Noncollinear optical parametric amplification of a supercontinuum

Henrik Åkesson

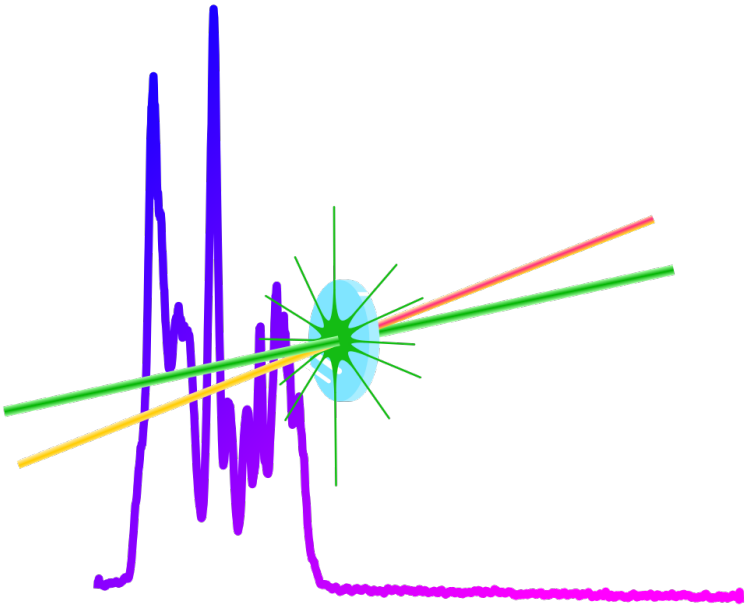

Master thesis

Supervisors: Fabian Langer and Ivan Sytcevich

Department of Engineering LTH
Lund University
March 11, 2019

Abstract

During this thesis, work has been done towards realizing a short-wave infrared (SWIR) laser source based on optical parametric amplification. It is planned that this setup should be able to produce few-cycle laser pulses at 2 µm with a stable carrier-envelope phase (CEP). This will be done by using various nonlinear processes to convert the output from a 1030-nm, 200 kHz laser source, based on Yb-doped rod-fiber amplifiers.

During my work, the first part of the envisioned SWIR source has been implemented: A supercontinuum has been generated, to provide a broadband seed for a non-collinear optical parametric amplifier (NOPA). The NOPA also requires a pump beam, which was produced using second-harmonic generation to obtain light at 515 nm. Finally, the NOPA was implemented using the supercontinuum seed and the pump beam.

The supercontinuum was generated through spectral broadening in a YAG crystal. The focusing conditions and the length of the crystal were adjusted to obtain a flat and stable spectrum in the wavelength range of interest (620 - 750 nm). The NOPA utilized a BBO crystal as a nonlinear medium. Phase-matching simulations of the NOPA process was carried out to design an optimal geometry for the amplification of the white light in the range of 640 - 750 nm. The NOPA was subsequently implemented using the optimal parameters obtained from the simulations. The resulting NOPA produced an output of 440 mW, using an input of approximately 5 - 6 mW of supercontinuum power. The spectrum of the amplified supercontinuum stretched between 640 - 695 nm. The gain of the NOPA is satisfying, however, the bandwidth is narrower than desired. Further improvements can be done to the amplifier such as removing residual chirp from the supercontinuum to further increase the bandwidth.

In future work, a stage performing difference frequency generation will be implemented, which will provide CEP-stable SWIR pulses.

Acknowledgements

First of all, I would like to thank my supervisors Fabian Langer and Ivan Sytcevich for all the help and comments on my work.

I would also like to thank Anne L'Huillier and Cord Arnold for introducing me to this interesting subject.

Popular science summary

Optical amplification of white light as a first step towards ultrashort laser pulses

In this master thesis, an infrared, pulsed laser was used to produce colorful, so called "white light", of which a part of was amplified using an optical amplifier. This is the first part of a planned larger setup (shown below), which can be used to, for example, produce ultraviolet light and possibly X-rays. Laser pulses at these wavelengths can be extremely short, which can be used to study extremely fast events, like the motion of electrons. Ultrashort laser pulses can also be used for such different things as the study of dissociation of molecules and eye surgery.

Ultrashort laser pulses are the shortest event in time created by humans. Currently it is possible to generate laser pulses in the timescale of attoseconds, which also is the timescale of electron motion. An attosecond is 10^{-18} s, or 0.000000000000000001 seconds. To put this into perspective, a really fast blink of the eye takes 0.1 s. This means that there is literally 100 million billion attoseconds during the blink of an eye. I suggest you blink right now to really get the idea.

In order to generate such short laser pulses, the wavelength of the light must also be very short. For attosecond laser pulses the light must at least be in the extreme ultraviolet (XUV). Unfortunately, there are no lasers today that can produce light with such a short wavelength, so alternative methods are required. A popular method is to take the light from an existing laser (usually an infrared laser) and convert this into light with much shorter wavelength (XUV).

My master thesis is the very of the first step of this process. We have taken infrared light at a wavelength of 1030 nanometers (nm, 10^{-9} m) from an existing laser and used it to produce so called *white light*. The light is in fact not necessarily white, it rather has a green/yellow color, but just like white light it has a very broad spectrum of colors. The white light was produced by sending intense infrared light through a crystal. Part of the white light, with an orange/red color, was then amplified using an *optical parametric amplifier*. This kind of amplifier works by using strong light to amplify weaker light. This is done by sending both beams of light through a suitable crystal. In this case, we used very intense green light to amplify the white light. The goal was to obtain amplified light between 620 - 750 nm.

The result is that a working amplifier was implemented. The amplifier provided an output power of 440 mW, which is a very good number. Unfortunately, the spectrum of the amplified light only covered 640 - 695 nm. This should however be possible to improve with further work.

The journey towards very short wavelength light and attosecond pulses will be continued by converting the amplified light back to infrared, but this time with a wavelength of 2000 nm. So the purpose of the whole process of creating white light and then amplifying it with green light, is to eventually end up with light that has roughly twice the wavelength of what we started with. This light can then finally be used for new and exciting investigations of generation of XUV light in gases as well as solid materials. The reason to why we want a longer wavelength, is that the process that we use to produce XUV light, called *high-harmonic generation*, depends on the wavelength. Rather counterintuitively, it produces light with a **shorter** wavelength, the **longer** wavelength light you put into it. The generated light can both be used to obtain information of the properties of the material and to produce ultrashort, attosecond laser pulses.

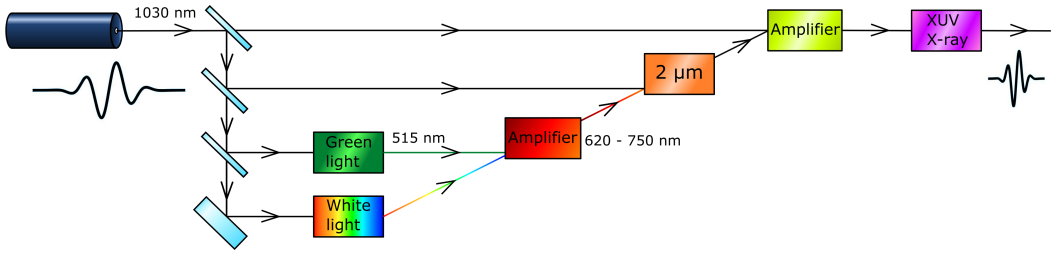

Schematic drawing of the process of how infrared light can be used to create ultrashort laser pulses. The laser itself produces pulsed light, but the pulses are much longer than what is desirable. The infrared light from the laser is first split up. One part is used to generate white light, which a part of is then amplified using the green light. The amplified light is then converted back to infrared at 2000 nm (2 µm) and amplified again. Finally the light is used to generate XUV light (and possibly even X-rays).

Table of contents

Physical constants

$c = 299792458$ m/s - speed of light in vacuum
$\epsilon_0 = 8.8542 \cdot 10^{-12}$ F/m - permittivity of free space
$e = 1.6022 \cdot 10^{-19}$ C - electron charge
$m_e = 9.1094 \cdot 10^{-31}$ kg - electron mass

Abbreviations

BBO - β-Barium Borate
CEP - carrier envelope phase
DFG - difference-frequency generation
FWHM - full width at half maximum
FWM - four-wave mixing
GVD - group velocity dispersion
HHG - high-harmonic generation
MIR - mid-infrared (3 - 8 µm)
MPI - multi-photon ionization
NA - numerical aperture
NIR - near-infrared (0.75 - 1.4 µm)
NOPA - non-collinear optical parametric amplifier
PEEM - photoelectron emission microscopy
SCG - supercontinuum generation
SF - self-focusing
SFG - sum-frequency generation
SHG - second-harmonic generation
SPM - self-phase modulation
SWIR - short-wavelength infrared (1.4 - 3 µm)
OA - optic axis
OPA - optical parametric amplifier
YAG - Yttrium Aluminium Garnet
XUV - extreme ultraviolet (10 - 124 nm)

1 Introduction

Ultrashort laser pulses are currently the shortest events in time made by humans. They are commonly used to study fast-evolving physical phenomena, such as electron motion in atoms and molecules [1] and electric field oscillations of other laser pulses [2]. At the time of writing, the shortest laser pulse ever created had a duration of 43 attoseconds (as, 10^{-18} s) [3]. In order to create such short pulses, the light must also have a short wavelength. This can be explained through the time-bandwidth product. As it turns out, the product of the time duration $\Delta\tau$ and the bandwidth $\Delta\nu$ of a laser pulse is limited by a constant C, that is, $\Delta\tau\Delta\nu \geq C$ [4]. The constant C depends on, for example, the pulse shape. In order to support a pulse with a short time duration, a large bandwidth is thus needed. Since the spectrum of the pulse is centered around the carrier frequency, a high carrier frequency is thus needed to support the wide bandwidth. This corresponds to a short carrier wavelength. For the case of few-cycle pulses with a duration on the timescale of attoseconds, it turns out that the carrier wave should be at least in the extreme ultraviolet (XUV) [4].

A method of creating coherent light with such short wavelengths is through the process of high harmonic generation (HHG). This is a non-linear process where intense laser light interacts with a medium, which results in the upconversion of the fundamental light into the extreme ultraviolet or even soft X-ray regime [5]. An atomic gas is usually used as the non-linear medium, although HHG has been reported in solids as well [6]. HHG in gases can be described with a three-step model [7], which is explained in a more simple way by reference [8]: First, atoms in the medium are tunnel-ionized by the driving field, leading to free electrons. Secondly, the free electrons are accelerated by the electric field of the laser light. Lastly, the electrons recombine with the atoms, and photons are emitted, whose energy is the sum of the ionization energy and the accumulated kinetic energy. The three-step process repeats for each half cycle of the fundamental field. Hence, the process is periodic in time. The periodicity translates via Fourier transformation into frequency space and modulates the spectrum. There will only be distinct harmonic peaks with a separation of twice the driving frequency, the "harmonics". The frequency spectrum of the resulting light has a distinct shape: Its intensity decreases exponentially for the first couple of harmonics, after which a plateau is formed. At this point the intensity of the spectrum stays constant for a large number of harmonics. Eventually a cutoff is reached and the amplitude drops rapidly [9]. In the single-atom picture, the maximum photon energy E_{max} corresponding to the cutoff is given by [7]

$$E_{max} = I_p + 3.17U_p = I_p + 3.17\frac{\mathrm{E}^2}{4\omega^2}, \tag{1}$$

where $U_p = \mathrm{E}^2/4\omega^2$ is the ponderomotive energy of the driving field, E is the electric field strength of the laser, ω is the angular frequency of the laser light and I_p is the atomic ionization potential.

As equation (1) shows, E_{max} increases for a decreasing ω. This means that for driving pulses with a longer wavelength, the photons created in the HHG process will be more energetic, which corresponds to a shorter wavelength of the resulting light. HHG is routinely performed in the near-infrared (NIR), so increasing the wavelength of the driving field towards the mid-infrared (MIR), will thus make it possible to obtain more energetic photons. There do exist lasers in the mid-infrared, but due to scalability difficulties with power, pulse duration and repetition rate [10] this is not a preferable solution for HHG. It is not possible to obtain short pulses with high power and stable CEP from such MIR lasers.

An increasingly popular approach is to use nonlinear processes of frequency conversion and amplification to acquire short, high-power pulses at the frequency of interest. This is also the approach used in this thesis. The laser light that will be used for this is taken from a laser system based on Yb-doped fiber rod amplifiers (a schematic drawing of this system is shown in figure 1). This system produces femtosecond pulses at 1030 nm at a repetition rate of 200 kHz, with a maximum power of 40 W.

The light from this source will be converted and amplified through a variety of nonlinear processes, and the plan is to obtain very short, few-cycle pulses centered at 2 µm. This is in the short-wave infrared (SWIR) wavelength range, which stretches between 1.4 - 3 µm. The resulting light will have twice the wavelength of the light from the 1030-nm source. High photon energies can thus be obtained through HHG, in accordance with equation 1. Furthermore, by generating few-cycle pulses, it will be possible to obtain only a few (ideally one) attosecond pulse after HHG.

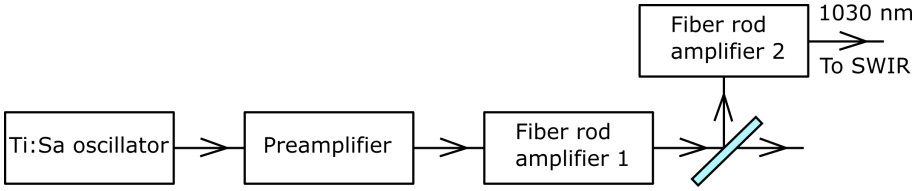

Figure 1: The light for the SWIR setup is taken from a Titanium-Sapphire (Ti:Sa) oscillator. Part of the spectrum from the oscillator around 1030 nm is picked and amplified. The amplification is done with a preamplifier and two Ytterbium-doped rod fiber amplifiers.

It would actually probably be possible to generate high harmonics from the 1030-nm source as well, however, due to the long pulses it produces (more than 100 cycles per pulse), the HHG would also result in many pulses, which is undesirable. The high repetition rate of 200 kHz will also be useful, since, although the maximum energy of the HHG increases for long wavelengths, the efficiency of the process drops as approximately $\lambda^{-6.5}$ [11]. A high repetition rate is therefore needed to obtain a suitable photon flux or to realize good statistics, for example in photoemission experiments. The high repetition rate will however require a very dense gas target [12], which will be challenging from an engineering point of view.

For few-cycle pulses the carrier-envelope phase (CEP) becomes important. The concept is illustrated in figure 2. The CEP of a laser pulse, denoted by ϕ_{CEP}, is the offset between the peak of the pulse envelope and the strongest half cycle of the carrier wave.

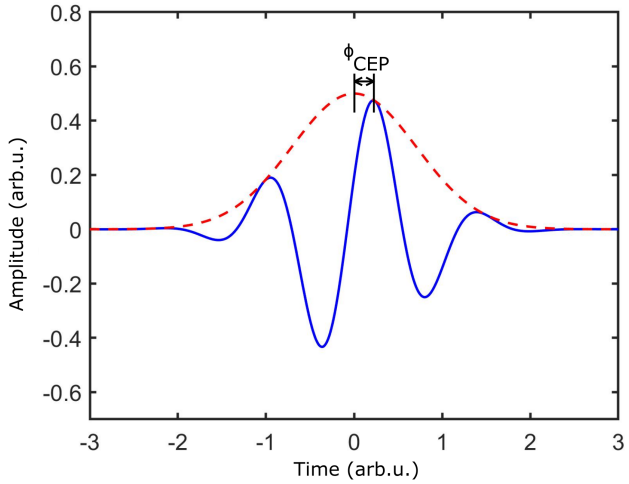

Figure 2: Definition of the carrier-envelope phase (CEP). The CEP (ϕ_{CEP}) is the offset between the peak of the pulse envelope and the strongest half cycle of the carrier wave.

The CEP has a large influence on the shape of few-cycle pulses. Figure 3 compares a few-cycle pulse with a multi-cycle pulse for two different CEPs. The change in shape is very clear for the few-cycle pulse, while for the multi-cycle pulse it is hard to distinguish. This means that the electric field strength in different half cycles of the pulses has a strong dependence on the CEP for few-cycle pulses.

HHG is strongly dependent on the electric field strength E through the ponderomotive energy. This will result in an HHG spectrum that is strongly dependent on the CEP [13, 14]. As can be seen in figure 3, the maximum field strength of pulse a) is larger than the maximum field strength of pulse b). Pulse a) should then be capable of producing more energetic photons. For the multi-cycle pulses in c) and d), however, there is far less difference in the maximum field strength, so the CEP is less important. It is also important to note the effect the CEP has on the symmetry of the amplitude of the pulses. In HHG, the electric field of the pulse accelerates the ionized electrons, causing a recollision event. Since the pulse in figure 3 b) has inversion symmetry, there are two half cycles that give similar recollision dynamics. However, the recollision also depends on the previous half cycle. The previous half cycle is what causes the tunnel-ionization (which is a highly nonlinear process). The pulse in figure 3 b) will therefore produce two pulses of different intensity.

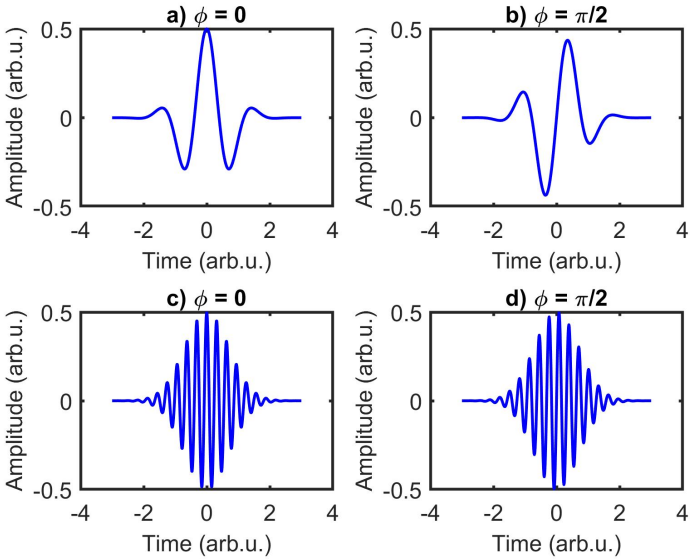

Figure 3: Comparison of the CEP effect on the pulse shape for few- and multi-cycle pulses. The difference is much greater for few-cycle pulses (a and b) than for multi-cycle pulses (c and d).

The pulse in figure 3 a) has on the other hand only one strong half cycle, so it is likely that this pulse will only produce one attosecond pulse. Because the CEP has such a great impact on the HHG process, control of the CEP is very important.

The CEP generally varies from pulse to pulse and must therefore be stabilized. Both active and passive CEP stabilization is possible [13]. In an active stabilization scheme the CEP is measured and a feedback loop is used to stabilize the CEP. A passive scheme, for example, employs difference frequency generation (DFG). DFG is a nonlinear process in which light at angular frequencies ω_1 and ω_3 combine to create light at angular frequency $\omega_2 = \omega_3 - \omega_1$, where $\omega_3 > \omega_1$ [15]. What is important is that the CEP of the wave at ω_2 will be the difference between the CEP of the waves at ω_1 and ω_3 [13], if the waves at ω_1 and ω_3 both are taken from the same source. Then, both waves will have the same phase fluctuations, and any variation in their phases will be cancelled in the DFG process and the wave at ω_2 will therefore have a constant CEP. It is the passive CEP-stabilization scheme that will be used for the laser presented here.

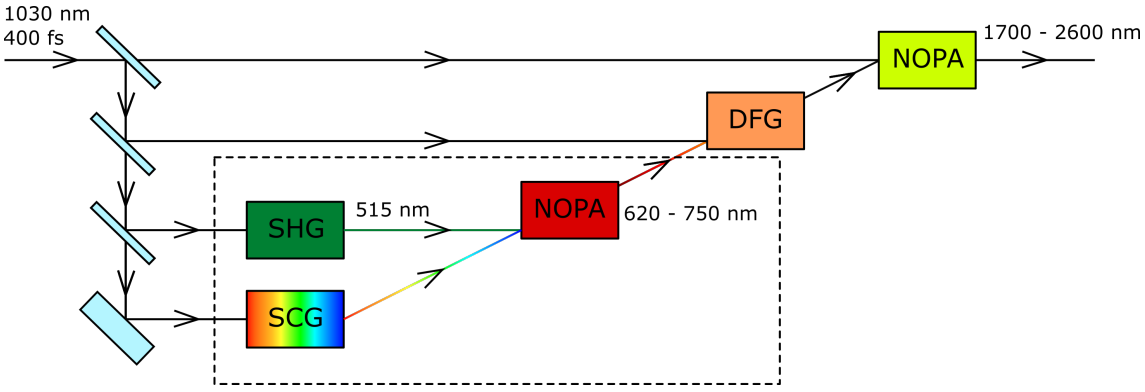

Figure 4: Schematic block diagram of the proposed final setup. SCG - supercontinuum generation, SHG - second-harmonic generation, NOPA - non-collinear optical parametric amplifier, DFG - difference-frequency generation. A supercontinuum is generated and part of it will be amplified in the NOPA. SHG is used to produce the pump for the NOPA. DFG is then performed between the amplified supercontinuum and the fundamental light at 1030 nm. Finally the output from the DFG will be amplified in a second NOPA. The black box indicates the parts that were implemented during the work of this thesis.

The setup that has been proposed to generate CEP-stable SWIR pulses is shown in figure

4. A compressor (not shown) is first used to compress the 1030-nm pulses to minimal duration (approximately 400 fs). The pulse is split several times and guided to the different stages of the SWIR source. The first stage is the supercontinuum generation (SCG), where the pulse is spectrally broadened in a YAG crystal. A previous master thesis [16], performed at the same research group as this thesis, investigated supercontinuum generation in a variety of materials. It was found that YAG was a particularly suitable medium, hence the choice of a YAG crystal for supercontinuum generation. The supercontinuum is then amplified using a noncollinear optical parametric amplifier (NOPA). In this process energy is taken from a pump beam and transferred to a signal beam (the supercontinuum). Here, second-harmonic generation (SHG) is used to create the pump beam. In the SHG process, the frequency of the fundamental light is doubled in a nonlinear crystal. This will result in light at a wavelength of 515 nm. The corresponding photon energy is sufficient to pump the NOPA, which amplifies the supercontinuum between 620 - 750 nm. The first NOPA stage provides a suitable pump beam for the DFG process with the 1030-nm radiation. The pulse is then finally amplified in a second NOPA, using the 1030-nm radiation as pump.

The proposed setup has been made by the team working in the lab where the setup will be used, and is based on similar, existing setups, such as the one described by reference [17]. This is a large, complex system, and during the work of this thesis, only the first part, as indicated by the black box in figure 4, was implemented (SHG, SCG and NOPA). I also followed the work during the setup of the compression and evaluated the measured data, so the compression will be covered as well. I have made all the calculations in this thesis. Building smaller set-ups for testing, for example for second-harmonic generation or supercontinuum generation, was done under supervision. The acquisition and analysis of the data was performed independently. Each of the parts of the setup will be presented in succession, since the results from the different parts will affect the implementation of the following parts. First the compression is discussed. Then the two inputs to the NOPA are covered, the SHG and the SCG. The results from these sections will then be used in the section about the NOPA. Finally, the future implementation of the rest of the setup will be discussed and also possible applications.

2 Ultrafast optics and pulse compression

The laser source that will be used for this setup (as shown in figure 1), employs a technique called chirped-pulse amplification, for which the Nobel prize in physics has been awarded in 2018. The idea is that dispersion is used to stretch the pulses in time, by rearranging the frequency components temporally (adding "chirp" to the pulse, in analogy to acoustics). The increased pulse duration leads to less intense pulses, which can then be amplified without risking non-linear effects or possibly even damage to the amplifier. This however means that the pulses must be compressed after the amplification in order to reach minimum time duration and maximum intensity. Although in this example dispersion is purposefully introduced to the pulses, dispersion is usually an unwanted, but omnipresent side effect in an optical system, resulting from propagation through optical components. For this reason, this first section will discuss the phenomena of dispersion, chirp and compression. The concept of chirp will also appear when discussing the supercontinuum. A method called interferometric autocorrelation that characterizes the pulse structure temporally and was used to minimize the pulse duration will also be covered. This section will, however, begin with discussing some basics of ultrafast optics, which will be useful throughout this thesis.

2.1 Basic ultrafast optics

Ultrafast pulses are composed of several frequencies, so that they have a broad spectrum. Furthermore, the temporal shape of the pulses depends on how the frequency components are phased with respect to each other. Different optical components have different effects on laser pulses as well. It is therefore necessary to discuss the basic principles of ultrafast optics. This will be done in the following sections, closely following reference [15].

Consider a light pulse $U(t)$ at central frequency ω_0 with the envelope $A(t)$, as described by [15]

$$U(t) = A(t) \exp\left(i(\omega_0 t + \phi(t))\right), \tag{2}$$

where $\phi(t)$ is a phase factor. The phase of the electromagnetic wave $U(t)$ is therefore $\omega_0 t + \phi(t)$. The intensity of the pulse is given by $I(t) = |A(t)|^2$ [15]. Usually, Gaussian pulses describe laser pulses very well. They have an intensity given by $I(t) \propto \exp\left(-2t^2/\tau^2\right)$ [15], where τ is a time constant describing the width of the function.

The spectrum of the pulse is described by its Fourier transform $V(\nu)$ [15]:

$$V(\nu) = |V(\nu)| \exp\left(i\psi(\nu)\right), \tag{3}$$

where $S(\nu) = |V(\nu)|^2$ is the spectral intensity and $\psi(\nu)$ is the spectral phase. The temporal and spectral width of the pulse are the width of the intensities $I(t)$ and $S(\nu)$. As criterion for the width, the full-width at half maximum (FWHM) is used, and the widths are denoted τ_{FWHM} and $\Delta\nu$, respectively. Since $V(\nu)$ is the Fourier transform of $U(t)$, the widths of $V(\nu)$ and $U(t)$ are inversely proportional [15]. For a Gaussian pulse, with a constant frequency carrier-wave (that is, a pulse without chirp), the relation is given by the time-bandwidth product [15]:

$$\tau_{\mathrm{FWHM}} \Delta\nu = 0.44. \tag{4}$$

Equation (4) can be used to estimate the pulse duration from the spectral width, and vice versa.

The frequency ν and the wavelength λ of an optical wave in vacuum are related by [15]

$$c = \lambda\nu, \tag{5}$$

where c is the speed of light in vacuum. This equation is useful for converting between wavelength and frequency, since both will be used throughout this thesis.

The width in wavelength $\Delta\lambda$ and the width in frequency $\Delta\nu$ can also be related to each other. However, these are differential variables and subsequently the expression is more complex. The relation is given by [15]

$$\Delta\lambda = \frac{\lambda_0^2}{c} \frac{\Delta\nu}{1 - (\Delta\nu/2\nu_0)^2}. \tag{6}$$

The instantaneous angular frequency ω_i is obtained by taking the derivative of the phase of $U(t)$, which gives [15]:

$$\omega_i = \omega_0 + \frac{\partial \phi}{\partial t}. \tag{7}$$

The angular frequency ω is related to the frequency ν by $\omega = 2\pi\nu$ [15]. Note that if $\frac{\partial \phi}{\partial t} = 0$, the instantaneous frequency will simply equal the central frequency. If instead $\frac{\partial \phi}{\partial t}$ has a time dependence, so that the second derivative of the phase $\phi'' \neq 0$, the instantaneous frequency will change in time [15]. This is called chirp. If the frequency is increasing at the pulse center, so that $\phi'' > 0$, the pulse is up-chirped [15]. If the frequency on the other hand is decreasing, the pulse is down-chirped. More specifically, if the phase is a quadratic function $\phi(t) = at^2/\tau^2$, the instantaneous frequency will change linearly over time and the pulse is therefore called linearly chirped. The constant a is called the chirp parameter and is given by [15]

$$a = \frac{1}{2}\phi''\tau^2, \tag{8}$$

which is obtained by differentiating the quadratic phase function twice.

Figure 5 shows one up-chirped and one down-chirped pulse. Note that the unit on the x-axis is time, so that the leading edge of the pulse is the leftmost part in the plot, since this part will arrive earlier in time.

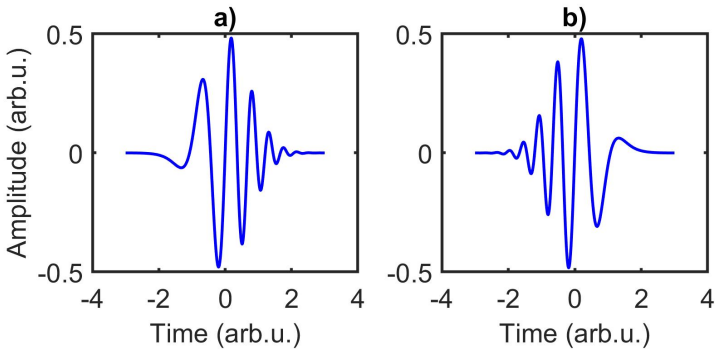

Figure 5: Chirped pulses. Pulse a) is up-chirped and pulse b) is down-chirped.

2.1.1 Gaussian pulse

If a pulse is transform-limited, the time-bandwidth product of the temporal and spectral widths is minimum [15]. This occurs when the Gaussian pulse has a constant phase factor ϕ and therefore no chirp. Equation (4) then gives the time-bandwidth product of a transform-limited Gaussian pulse. A transform-limited Gaussian pulse has the complex envelope and intensity as given by equations (9) and (10) [15].

$$A(t) = A_0 \exp\left(-t^2/\tau^2\right) \tag{9}$$

$$I(t) = I_0 \exp\left(-2t^2/\tau^2\right) \tag{10}$$

The time constant τ is related to the FWHM width of the intensity $I(t)$ by $\tau_{\mathrm{FWHM}} = \sqrt{2\ln 2}\tau$ [15]. An interesting property of the Gaussian pulse is that the Fourier transform of the Gaussian pulse is also a Gaussian pulse [15]. The spectral intensity of an unchirped Gaussian pulse is given by [15]

$$S(\nu) \propto \exp\left(-2\pi^2\tau^2(\nu - \nu_0)^2\right), \tag{11}$$

which indeed has a Gaussian shape.

As will be explained in the next section, chirp can be added to a pulse through dispersion; this will result in the rearrangement of the frequency components of the pulse. This will lead to a temporal broadening of the pulse, so that the intensity will be given by

$$I(t) = I_0 \exp\left(-2t^2/\tau^2(1+a^2)\right). \tag{12}$$

The amount of broadening thus depends on the amount of chirp through the chirp parameter a. However, adding chirp to a pulse will only redistribute the frequency components over time, not add any new frequencies. The spectral intensity, as given by equation (11), will therefore be unchanged for a chirped pulse.

Comparing equation 10 and equation 12 shows that the temporal width of the chirped pulse is increased by a factor $\sqrt{1+a^2}$. Equation 4 will therefore be modified for a chirped Gaussian pulse, so the time-bandwidth product will be given by

$$\tau_{\mathrm{FWHM}}\Delta\nu = 0.44\sqrt{1+a^2}, \tag{13}$$

according to reference [15].

2.1.2 Dispersion

As previously mentioned, dispersion can cause an optical pulse to become chirped. This section will introduce dispersion and show how this can result in a chirped pulse. Dispersion can however also be used to remove chirp, as will be explained in the following section about compression.

Dispersion is the wavelength dependence of the refractive index of the material, so that the **phase velocity** v of the wave in the material depends on the wavelength according to equation (14) [15]

$$v = \frac{c}{n(\lambda)}. \tag{14}$$

The phase velocity is the speed at which a point of constant phase on the wave travels. This point can for example be a peak of the electric field. This peak will then travel at a speed of the phase velocity.

Dispersion also affects the **group velocity**. The group velocity is the speed at which a change in amplitude of the wave travels, that is, for a pulsed wave it is the speed at which the envelope travels. The group velocity v_g is given by [15]

$$v_g = \frac{c}{n - \lambda\frac{dn}{d\lambda}}. \tag{15}$$

Equation (15) is of the same form as equation (14), except that the term $-\lambda\frac{dn}{d\lambda}$ is added to the refractive index. Most optical materials in the visible and infrared range have an increasing refractive index with decreasing wavelength [15], so that $\frac{dn}{d\lambda} < 0$. In this case, the denominator in equation (15) is larger than in equation (14), so that $v_g < v$. The effect of the difference between v and v_g is illustrated in figure 6, where a laser pulse is depicted at three moments in time.

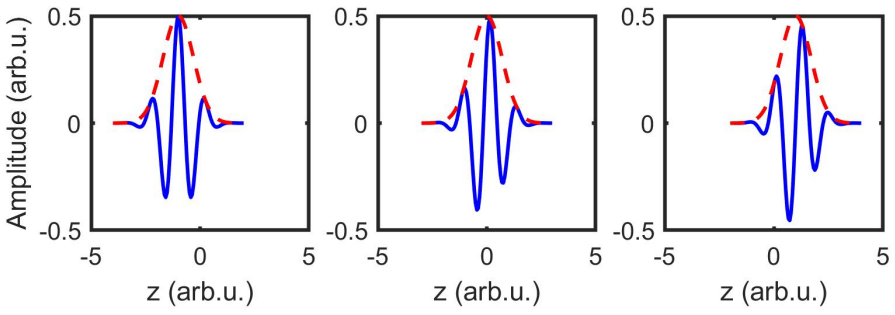

Figure 6: A laser pulse depicted at three moments in time, where $v_g < v$. The central half cycle of the electric field will arrive progressively earlier in time than the pulse envelope due to the higher velocity of the electric field. Note that the pulses are depicted in space, where z is the space coordinate.

Just like the phase velocity, dispersion also affects the group velocity, since the group velocity is dependent on the refractive index. For pulsed light, the wavelength of the carrier wave will therefore determine the speed at which the pulse travels. However, because the pulse actually comprises a

spectrum of wavelengths, the different spectral components of a pulse will travel at different speeds. This phenomenon is called group velocity dispersion (GVD), and results in a temporal broadening of the pulse. The amount of broadening caused by GVD will naturally depend on the derivative of the group velocity with respect to the wavelength. A large derivative means a large change in group velocity with wavelength, which will cause a large broadening of the pulse. In reference [15], the amount of broadening is quantified by the dispersion coefficient D_λ, as given by

$$D_\lambda = -\frac{\lambda_0}{c}\frac{d^2 n}{d\lambda_0^2}, \tag{16}$$

where λ_0 is the central wavelength. The broadening for a Gaussian pulse is given by

$$\sigma_\tau = |D_\lambda|\sigma_\lambda z, \tag{17}$$

where σ_τ is the temporal broadening, σ_λ is the spectral width of the pulse and z is the propagation distance. Note that equation (17) is an approximation; it only holds when the broadening is much larger than the initial pulse duration.

Group velocity dispersion is what causes the chirp of the pulse, due to the temporal redistribution of the frequency components of the pulse. The amount of chirp depends on the **magnitude** of the dispersion coefficient D_λ, as equation (17) shows. The **sign** of D_λ will on the other hand determine whether the pulse will be up- or down-chirped (that is, the sign of the chirp). In the case when the dispersion coefficient $D_\lambda < 0$, longer wavelengths will travel faster than shorter ones, which is called normal dispersion [15] (since this is the normal case in most materials in the visible and near-infrared). This will result in an up-chirped pulse. The opposite case, when $D_\lambda > 0$, is called anomalous dispersion and causes shorter wavelengths to travel faster than longer ones [15]. This will result in a down-chirped pulse. The process of how normal dispersion leads to an up-chirped pulse is illustrated in figure 7.

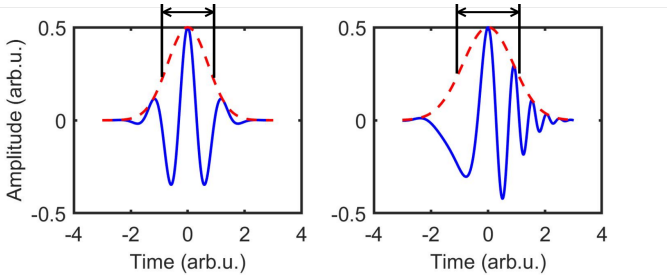

Figure 7: A laser pulse depicted before (left) and after (right) experiencing GVD. In this case the high frequencies are delayed more than the low frequencies (normal dispersion), which causes the chirp and subsequent temporal broadening.

2.1.3 Pulse compression with a chirp filter

As has just been shown, dispersion can be used to add chirp to a pulse. One or more dispersive optical elements can be combined into what is called a chirp filter [15]. A chirp filter can be used to both add or remove chirp. Removing chirp can be accomplished if the chirp introduced by the chirp filter has the opposite sign of the chirp of the pulse [15]. This means that a chirp filter can be used to compress a chirped pulse, since the unchirped pulse will have a shorter time duration than the chirped one (compare the time-bandwidth products of an unchirped and chirped Gaussian pulse in equations (4) and (13)).

Pulse compression is an essential first step of the envisioned SWIR setup, since the 1030-nm laser source is based on chirped-pulse amplification and therefore produces pulses with a significant chirp. Reversing the chirp of the pulses through compression will therefore provide much shorter, much more intense pulses. Compression may also be needed at other positions in the SWIR setup as well, since the pulses will gain some chirp by travelling through the various optical components of the setup.

As previously mentioned, most materials exhibit normal dispersion in the visible and near-infrared. The compressor must therefore introduce anomalous dispersion. This can be accomplished by using optical components exhibiting angular dispersion, for example prisms and grat-

ings. These can be arranged so that they introduce negative chirp, which can then compensate for the usually positive chirp caused by the normal dispersion of an optical system.

Figure 8 shows how two gratings can act as a chirp filter. This is what will be used in the SWIR setup. Due to the wavelength dependence of the deflection angle of the grating, the red light has to travel a longer distance than the blue light and will therefore be delayed more. That is, the path PACR of the red light in figure 8 is longer than the path PABQ of the blue light. This indicates that this setup would possibly be able to introduce the desired negative chirp. This is indeed the case, which is shown in great detail in reference [18]. The most important results of that paper will be summarized in the following, and the reader is referred to the paper for the complete derivation.

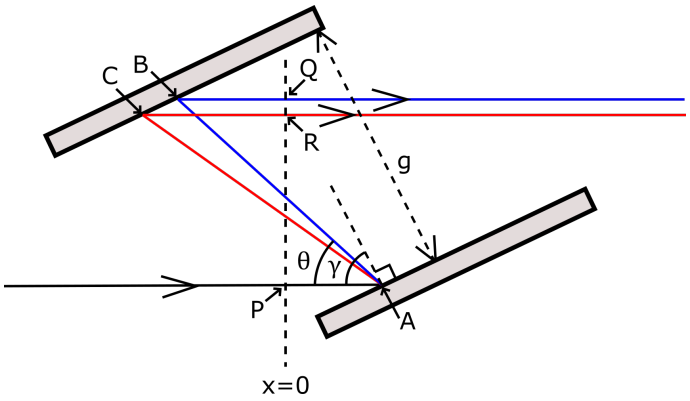

Figure 8: A grating compressor using the angular dispersion of the two gratings. Negative chirp is introduced since the path PABQ is shorter than PACR. Adapted from [18].

The phase shift of an optical wave that travels through the compressor is denoted by φ. The corresponding time delay τ is given by

$$\tau = \frac{\partial\varphi(\omega)}{\partial\omega} = \tau_0 - \frac{\omega - \omega_0}{\mu} + O(\omega - \omega_0)^2, \tag{18}$$

which is a linear expansion around the central frequency ω_0, so that τ_0 and μ^{-1} are the values τ and $-\partial\tau/\partial\omega$, evaluated at $\omega = \omega_0$.

The first term, τ_0, is the group delay at ω_0. The second term, $\mu^{-1}(\omega - \omega_0)$, is the change in group delay at the frequency ω compared to the group delay at the central frequency. This term accounts for the linear chirp introduced by the gratings, since μ depends on the second derivative of the phase shift φ. It may, however, be needed to include higher-order terms as well in order to treat broader bandwidths, which is indicated by the last term. The constants τ_0 and μ^{-1} are given by

$$\tau_0 = \frac{b}{c}(1 + \cos\theta) \tag{19}$$

and

$$\mu^{-1} = -\frac{\partial\tau}{\partial\omega} = \frac{4\pi^2 cb}{\omega^3 d^2(1 - ((2\pi c/\omega d) - \sin\gamma)^2)}, \tag{20}$$

where d is the grating constant, c is the speed of light in vacuum, and $b = \mathrm{AB} = \mathrm{g}\cdot\sec(\gamma - \theta)$ is the distance between A and B in figure 8.

Equation (18) can be used to determine the output $B(t)$ from the compressor. Assume that the input is a wave $A(t)\exp(i\psi(t))\exp[-i\omega_0 t]$. The output of the compressor can be found by taking the Fourier transform of the input wave, multiplying it with the phase shift $\exp(i\varphi(\omega))$ introduced by the compressor and then take the inverse transform. The phase shift φ is obtained through integration of equation (18). This results in the output

$$B(t' + \tau_0) = (\frac{\mu}{2\pi})^{1/2}\exp[i(\varphi_0 - \frac{\pi}{4} - \omega_0(t' + \tau_0))]\int A(t)\exp(i\psi(t))\exp[i\frac{\mu}{2}(t - t')^2]dt. \tag{21}$$

To obtain the output of a chirped pulse, equation (21) will first be rewritten slightly:

$$B(t'+\tau_0)\exp\left[i\omega_0(t'+\tau_0)\right] = (\frac{\mu}{2\pi})^{1/2}\exp\left[i(\varphi_0-\frac{\pi}{4})\right]\int A(t)\exp\left(i\psi(t)\right)\exp\left[i\frac{\mu}{2}(t-t')^2\right]dt. \quad (22)$$

A chirp $\psi(t) = -\frac{1}{2}\mu t^2$ is then introduced to the input pulse, resulting in a total input of $A(t)\exp\left[-i(\omega_0 t + \frac{1}{2}\mu t^2)\right]$. This results in a phase with a quadratic dependence, which is consistent with a linearly chirped pulse with a frequency that changes at a rate $-\mu$. Note that the assumed chirp parameter $-\mu$ of the input pulse is the same, but of opposite sign as the linear chirp introduced by the grating pair. Insertion of the chirped pulse into equation (22) will result in the output

$$B(t'+\tau_0)\exp\left[i\omega_0(t'+\tau_0)\right] = (\frac{\mu}{2\pi})^{1/2}\exp\left[i(\varphi_0-\frac{\pi}{4})\right]\exp\left[i(\mu/2)t'^2\right]\int A(t)\exp\left(i\mu t' t\right)dt. \quad (23)$$

Note the factor $\exp\left[i(\mu/2)t'^2\right]$ before the integral. This factor will add a chirp that is exactly the opposite of the input pulse, which shows that the grating pair indeed works as a compressor. The geometry of the gratings determines the value of μ (equation (20)), so the geometry can be adjusted to obtain the correct factor μ to reverse the chirp of the input pulse. However, this is only true for narrow bandwidths, due to the linear expansion of the group delay in equation (18). Furthermore, it is assumed that the input pulse is Gaussian.

2.1.4 Interferometric autocorrelation

The previous section discussed the need for pulse compression in the setup and how this can be achieved with a grating compressor. As was noted, the geometry of the compressor must be adjusted to obtain the greatest compression. A method to characterize the chirp after compression is thus needed. A straight-forward way to achieve this goal is to make use of an interferometric autocorrelator. An implementation of this is shown in figure 9.

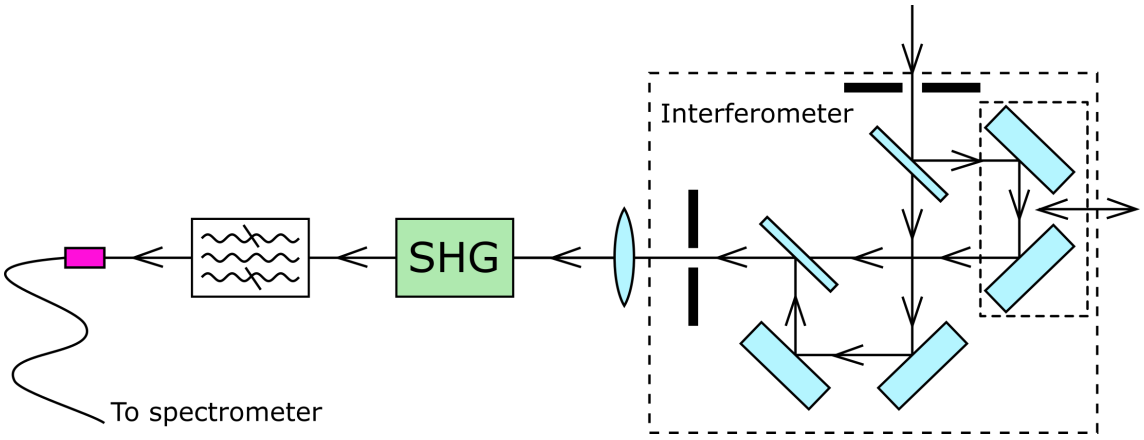

Figure 9: The autocorrelator consists of an interferometer and a nonlinear crystal. The incoming pulse is split into two identical pulses. One of the mirror pairs can be moved, in order to change the delay between the pulses. Both pulses are recombined and focused into a nonlinear crystal, creating light at the second-harmonic frequency (515 nm). Because of the nonlinearity, substantially more light will be created when the delay is adjusted so that the pulses overlap. A bandpass filter is used to remove the fundamental light at 1030 nm so that only the second harmonic reaches the spectrometer. SHG - second-harmonic generation.

The pulse is sent into an interferometer and then focused into a nonlinear crystal (more about nonlinear optics and second-harmonic generation in section 3 and appendix 1). In the interferometer the incident pulse is split equally into two pulse copies using a beamsplitter. The two pulse copies are guided by two mirrors each and then recombined. One of the mirror pairs can be moved in order to change the delay of one pulse copy with respect to the other. The pulses are then recombined and focused into the nonlinear crystal, which essentially performs a squaring operation, which results in light at 515 nm. A bandpass filter is used to filter out the fundamental

light, and the spectrum from the autocorrelator is measured with a fiber spectrometer. Normally, interferometric autocorrelation is performed with a photodiode, however, due to the availability of measurement equipment, a spectrometer was used. To obtain the total intensity of the second harmonic, the spectral intensity can simply be integrated around the wavelength of interest (515 nm). Furthermore, it is also possible to use the shape of the second-harmonic spectrum as an indicator for the compression as well.

The idea behind interferometric autocorrelation is to use the interference pattern that is produced to estimate the chirp and duration of a pulse (the pulse will in this case come from the compressor). When the delay of the interferometer is adjusted so that both arms have equal pathlength, the pulse copies will perfectly overlap in the nonlinear crystal and the interference will be constructive, resulting in the largest amount of second-harmonic light. Changing the delay just ever so slightly, will cause the interference to go from constructive to destructive and in principle no light will be obtained. However, the greater the delay between both pulse copies get, the less they will overlap. This will reduce the contrast of the interference pattern, until the point at which the pulses no longer overlap and thus no interference can be observed. This also shows that the width of the interference pattern is related to the width of the pulse.

The interference pattern is given by [15]

$$R_U^{(2)}(\kappa) = \int |(\mathrm{E}(t) + \mathrm{E}(t-\kappa))^2|^2 dt, \tag{24}$$

where κ is the time delay and E is the electric field of the pulse. Note the two squaring operations within the integral expression. The first one is due to the squaring operation of the nonlinear crystal. The second one is due to the fact that it is the intensity that is measured, which depends quadratically on the electric field [15]. This shows that if both pulse copies are perfectly overlapping in the nonlinear crystal, the electric field will be twice that of a single pulse, 2E. This will be squared twice, giving a measured intensity of $16\mathrm{E}^4$. In contrast, if the delay κ is adjusted so that the pulse copies are not overlapping in the crystal, each pulse will only result in the intensity E^4. After integration this gives $2\mathrm{E}^4$. The contrast will therefore be $16\mathrm{E}^4/2\mathrm{E}^4$, or 1:8 [4]. Note that, without a nonlinear crystal, the contrast would only be 1:2, due to the loss of one of the squaring operations in equation (24). The nonlinear crystal is also necessary to obtain information about the spectral phase [15], which means that it will be possible to estimate the chirp from the interference pattern, as will be shown in the following.

For a Gaussian pulse with time constant κ_0 and chirp parameter a, the integral in equation (24) computes to [15]

$$\begin{aligned} \frac{R_U^{(2)}(\kappa)}{R_U^{(2)}(\infty)} =& 1 + 2\exp(-\kappa^2/\kappa_0^2) + \\ & 4\exp(-(3+a^2)\kappa^2/4\kappa_0^2)\cos(a\kappa^2/2\kappa_0^2)\cos(\omega\kappa) + \\ & \exp(-(1+a^2)\kappa^2/\kappa_0^2)\cos(2\omega\kappa), \end{aligned} \tag{25}$$

when normalized with the asymptotic value $R_U^{(2)}(\infty)$. The resulting autocorrelation trace from equation 25 is plotted in figure 10, for a pulse with $\lambda = 1030$ nm, $\tau_{\mathrm{FWHM}} = 20$ fs and $a = 0, 2, 4$.

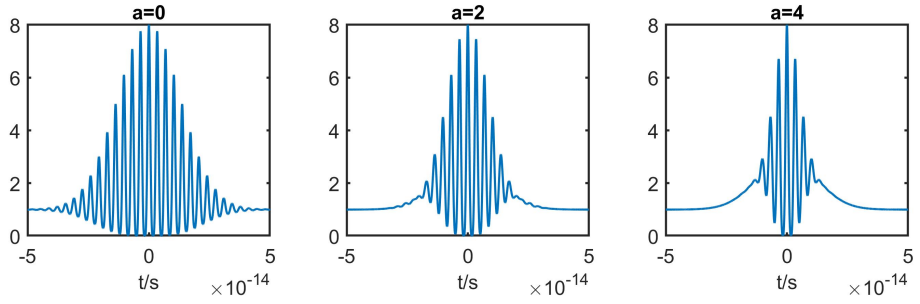

Figure 10: Interferometric autocorrelation trace for a 20 fs, 1030 nm pulse for chirp parameters $a = 0, 2, 4$.

As the figure shows, the ratio of the amplitudes of the autocorrelation trace between perfect pulse overlap and no overlap is indeed 1:8. However, the width of the trace is narrower the more the pulse is chirped, even though the pulses for which the traces in figure 10 are plotted for have the same length (in reality, when the autocorrelator is used in conjuction with pulse compression, the chirped pulses will in fact have a longer duration). Using the width of the trace is therefore deceptive when compressing a chirped pulse. However, the profile of the trace where the oscillation stops also depends on the chirp. The more the pulse is chirped, the more the trace is bent upwards at these points as can be seen from the figure. It is therefore better to use the profile of the trace to deduce the magnitude of the chirp. It is not possible to determine the sign of a from the profile, as indicated by equation (25), which is an even function of a. So for example, both $a = 2$ and $a = -2$ will result in the same trace.

2.2 Compression of narrowband amplified pulses at 1030 nm

2.2.1 Setup

The compression setup is shown in figure 11. The pulses from the laser source (as shown in figure 1) are guided to the grating compressor. The compressor consists of two transmission gratings. The compressor was previously discussed for reflection gratings, but the principle is the same for transmission gratings. The beam is dispersed by the first grating, after which it hits the second grating. The gratings are parallel to each other and the distance between them can be adjusted to maximize the compression. The beam is then reflected back using a retro reflector, which also lowers the beam so that it travels along the same path as the first beam but can be picked up by a mirror at a lower height after the compressor. As figure 8 shows, there will be a spatial separation of the different frequency components after the two gratings, which leads two a spatial chirp. The use of a retro reflector will let the beam travel back along the same path in the compressor, thus removing the spatial chirp. After the compressor the beam is guided to the autocorrelator and the spectrum of the second harmonic is measured with a fiber spectrometer.

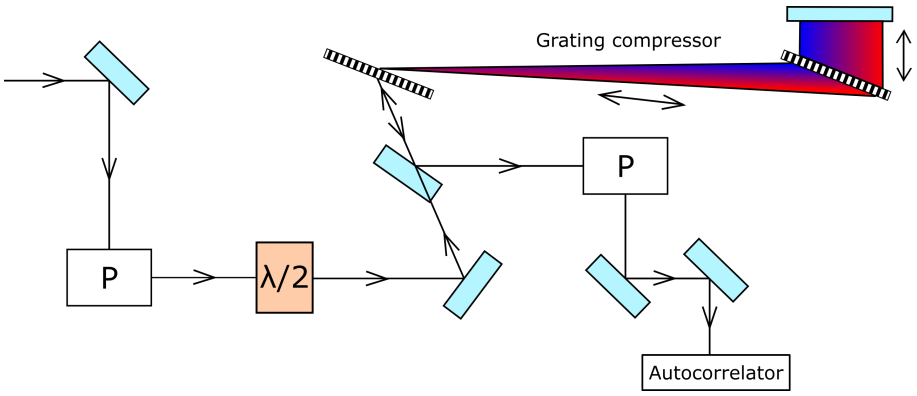

Figure 11: Setup for the compression. P - periscope.

2.2.2 Results and discussion

Figure 12 shows the autocorrelation trace for the compression that gives the shortest pulse duration. The width of the trace is 594 fs.

As can be seen in figure 12, the autocorrelation trace does not look like the ideal one (compare to figure 10). Most notably, the amplitude of the oscillation reaches a minimum (at around -500 fs and 500 fs, respectively) but increases again after this. This can be the result of noise and possibly a multi-pulse structure. The trace in figure 12 has been normalized so that the maximum amplitude is 8. The contrast between the maximum and the baseline (the amplitude of the trace at which the oscillation is ideally zero) is ideally 1:8. Although the oscillation is not zero, it can be seen that the right endpoint of the trace is well centered around 1, but the left endpoint is centered somewhat above 1. The reason for this may be that the autocorrelator is not perfectly aligned.

Studying the profile of the trace at the points where the oscillations are minimum shows that the trace is relatively flat, it does not "bend up" like it does for a chirped pulse. This would suggest that the pulse has relatively little chirp and therefore is well compressed. It is therefore reasonable

to approximate the width of the pulse from the autocorrelation trace. This, however, requires the knowledge of the pulse shape, which is not possible to deduce from the trace. The trace does have a shape that is reminiscent of a Gaussian pulse, but the shape of the trace and the pulse are two different things and does not necessarily have to be similar. For example, in a properly aligned autocorrelator the trace is always symmetric, even though the pulse may not be so [4]. Since it is not possible to determine the pulse shape from the trace, it is assumed that the pulse has a Gaussian profile, since this is a common and not unreasonable assumption. Since the chirp of the pulse is relatively small, the width of the trace can therefore be used to approximate the pulse duration. For a Gaussian unchirped pulse the width of the autocorrelation trace is $\sqrt{2}$ times wider than the actual pulse [15]. The width of the trace is 594 fs, so this gives a pulse duration of 420 fs. The pulse duration will be approximated as 400 fs throughout the rest of this thesis, and will be used to e.g. do various estimations of intensity.

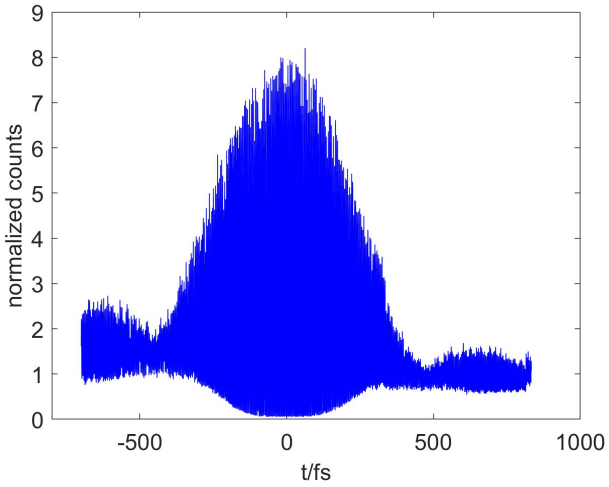

Figure 12: Autocorrelation trace of the compressed pulse.

3 Nonlinear optics and second harmonic generation

Part of the 1030 nm light will be frequency doubled and used as a pump for the NOPA. The reason for the frequency doubling is that the photons of the pump must have a higher energy than the photons of the light to be amplified. This section begins by discussing nonlinear optics in general, which will be useful throughout this thesis. Second-order nonlinear effects will be discussed in particular, which will be needed throughout this section, but for the parts about the NOPA and DFG as well. Phase-matching will be discussed very rapidly (the whole discussion can be found in appendix 1). Lastly, it will be shown how the SHG was implemented in the setup.

3.1 Nonlinear optics

An electric field $\mathbf{E}$ incident on a medium will introduce an electric flux density $\mathbf{D}$ as given by [15]

$$\mathbf{D} = \epsilon_0 \mathbf{E} + \mathbf{P}. \tag{26}$$

The polarization density $\mathbf{P}$ characterizes the polarization response of the medium to an external electric field. Generally, the polarization density depends on the electric field. Usually, the polarization density $\mathbf{P}$ is approximated to be linear to the electric field, in which case the relation is given by [15]

$$\mathbf{P} = \epsilon_0 \chi \mathbf{E}, \tag{27}$$

where χ is the electric susceptibilty of the material.

The polarization density $\mathbf{P}$ is a measure of the total displacement of all electrons due to the electric field. At low electric field strengths, the displacement is small and the binding potential of the electrons can be approximated with a quadratic, harmonic potential, which shows a linear response. When the external field becomes reasonably large, however, the electrons are displaced so far that they experience deviations from a harmonic potential and anharmonicities play into their motion. At this point, the linear response approximation is no longer valid and higher-order terms have to be included into the polarization density [19]. The nonlinear polarization density can be written as a series given by [19]

$$\mathbf{P} = \epsilon_0(\chi \mathbf{E} + \chi^{(2)}\mathbf{E}^2 + \chi^{(3)}\mathbf{E}^3 + \cdots) = \epsilon_0 \chi \mathbf{E} + \mathbf{P}_{\mathrm{NL}}, \tag{28}$$

where $\chi^{(2)}$ and $\chi^{(3)}$ are the strength of the second and third order term of the electric susceptibility. The coefficients $\chi^{(2)}$ and $\chi^{(3)}$ are usually very small, so it is often not necessary to include more terms in the expansion. The coefficients $\chi^{(2)}$ and $\chi^{(3)}$ are actually tensors, so they depend on the crystal orientation and/or polarization.

3.1.1 Second-order nonlinear effects

In this section, higher-order effects will be neglected and only second-order nonlinearities will be discussed. The nonlinear polarization can then be written as

$$\mathbf{P}^{(2)}_{\mathrm{NL}} = \epsilon_0 \chi^{(2)} \mathbf{E}^2. \tag{29}$$

It will here be of interest to see the effect of an electric field consisting of two harmonic components:

$$\mathbf{E}(t) = \frac{1}{2}[\mathrm{E}(\omega_1)\exp(i\omega_1 t) + \mathrm{E}(\omega_1)^*\exp(-i\omega_1 t)] + \frac{1}{2}[\mathrm{E}(\omega_2)\exp(i\omega_2 t) + \mathrm{E}(\omega_2)^*\exp(-i\omega_2 t)]. \tag{30}$$

By inserting equation (30) in equation (29), five different frequency components of $\mathbf{P}^{(2)}_{\mathrm{NL}}$ will be obtained at angular frequencies 0, $2\omega_1$, $2\omega_2$, $\omega_1 + \omega_2$ and $\omega_1 - \omega_2$. These components are given by:

$$P_{\mathrm{NL}}(0) = \chi^{(2)}(|\mathrm{E}(\omega_1)|^2 + |\mathrm{E}(\omega_2)|^2), \tag{31}$$

$$P_{\mathrm{NL}}(2\omega_1) = \chi^{(2)}\mathrm{E}(\omega_1)\mathrm{E}(\omega_1)\cos(2\omega_1 t), \tag{32}$$

$$P_{\mathrm{NL}}(2\omega_2) = \chi^{(2)}\mathrm{E}(\omega_2)\mathrm{E}(\omega_2)\cos(2\omega_2 t), \tag{33}$$

$$P_{\mathrm{NL}}(\omega_1+\omega_2) = 2\chi^{(2)}\mathrm{E}(\omega_1)\mathrm{E}(\omega_2)\cos((\omega_1+\omega_2)t), \tag{34}$$

$$P_{\mathrm{NL}}(\omega_1-\omega_2) = 2\chi^{(2)}\mathrm{E}(\omega_1)\mathrm{E}^*(\omega_2)\cos((\omega_1-\omega_2)t). \tag{35}$$

Equations (32) and (33) describe the case where one wave is doubled in frequency. This is called second-harmonic generation (SHG). The creation of a wave with angular frequency $\omega_3 = \omega_1+\omega_2$ (equation (34)) is called sum-frequency generation (SFG). Emission of a wave with angular frequency $\omega_3 = \omega_1-\omega_2$ (equation (35)) is called difference-frequency generation (DFG).

The nonlinear process takes place throughout the length of the crystal, which means that light with the new frequency is continuously created as the fundamental light propagates through the crystal. It is clear that the waves created at each point must have the same phase as the previously generated waves, so their interference is constructive. Otherwise the interference would be destructive and no light with the new frequency would be obtained. To maintain the right phase, a phase-matching condition needs to be satisfied. If waves with angular frequencies ω_1 and ω_2 efficiently generate a wave with angular frequency ω_3, then the angular frequencies are related by equation (36)

$$\omega_3 = \omega_1+\omega_2. \tag{36}$$

Equation (36) can be interpreted as an energy conservation condition, since the energy of a photon is given by $\hbar\omega$ [15]. The condition for energy conservation is then given by $\hbar\omega_3 = \hbar\omega_1+\hbar\omega_2$.

The phase-matching condition is given by [15]

$$\mathbf{k}_3 = \mathbf{k}_1+\mathbf{k}_2, \tag{37}$$

where $\mathbf{k}$ are the corresponding wavevectors. The length of $\mathbf{k}$ is given by $|\mathbf{k}| = \frac{2\pi n}{\lambda}$ (this is also denoted k and termed the wavenumber) and the direction of $\mathbf{k}$ is perpendicular to the wavefronts. The momentum of a photon is given by $\hbar\mathbf{k}$ [15]. Equation (37) then gives the momentum conservation relation $\hbar\mathbf{k}_3 = \hbar\mathbf{k}_1+\hbar\mathbf{k}_2$ (similar to the energy conservation condition). The phase-matching condition in equation (37) ensures that the polarization created by waves 1 and 2, which propagates with the wave vector $\mathbf{k}_1+\mathbf{k}_2$, remains in phase with the emitted wave 3 featuring the wave vector $\mathbf{k}_3$.

3.2 Calculation of phase matching for SHG in BBO

The phase-matching calculations for the second-harmonic generation can be found in appendix 1. In short, the phase-matching condition (equation (37)) will result in a condition on the refractive indexes of the fundamental wave and the second harmonic. This condition can only be satisfied using the birefringent properties of the BBO crystal that will be used for the second-harmonic generation. This will result in a phase-matching angle θ, which determines the propagation direction of the light with respect to the crystal's optic axis. Perfect phase-matching can however only be obtained for one single wavelength, which leads to the SHG process being less efficient for other wavelengths. Since phase matching is a propagation effect, this will put a limit to how thick crystal that can be used.

The result of this is that the phase-matching angle is $\theta = 23.39°$, and a suitable crystal thickness is 4 mm.

If the reader is unfamiliar with this kind of calculations, it is suggested to read appendix 1 before continuing any further. The concepts discussed in appendix 1 will also be needed for the discussion of the NOPA (section 5).

3.3 Setup for SHG

Figure 13 shows the setup for the second-harmonic generation. The incoming beam is focused with a 500 mm focal length lens into the BBO. The purpose of the focusing is to increase the intensity of the light, in order to maximize the second-harmonic generation. As previously mentioned the nonlinear effect is quite weak and becomes stronger with a stronger electric field (equation (29)). Since the intensity is proportional to the square of the electric field [15], increasing the intensity will give better conversion at the second-harmonic frequency. Naturally, there is a limit to how intense the light can be before the crystal is damaged. That is why a rather long focal length is used, to make sure that the intensity does not become to high.

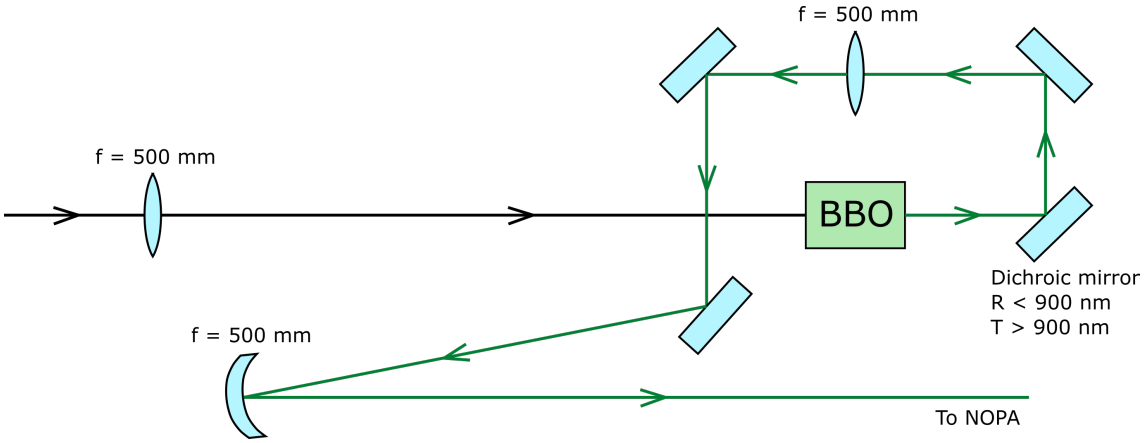

Figure 13: Setup for second-harmonic generation. The infrared light is focused into the nonlinear crystal. A dichroic mirror is used to filter out the remaining infrared light and guide the generated green light along. A second lens is used to collimate the green light, and a concave mirror is used to focus the light into the crystal for the NOPA.

The BBO crystal produces green light at 515 nm. The light is guided with two mirrors to another 500 mm focal length lens, which collimates the light. One of these mirrors is a dichroic mirror. A dichroic mirror has a wavelength dependent reflectance [4]. The dichroic mirror used here has a high reflectance below 900 nm, and a high transmittance above 900 nm. The infrared light will then pass straight through the mirror, while the green light will be reflected. After collimation the beam is guided to a 500 mm focal length concave mirror, which is used to focus the beam into the NOPA crystal.

The efficiency of the SHG was maximized by optimizing the orientation of the crystal and the position relative to the focus. The angle of incidence was adjusted so that the maximum amount of green light was obtained. Since the crystal is cut so that the optic axis already is at the phase-matching angle, the incidence should be normal, or at least very close to normal. The position of the focus was then optimized by moving the BBO crystal along the propagation axis of the beam. The optimal position of the focus has been investigated in reference [20]. It was found that the maximum amount of light at the second-harmonic frequency was obtained with the focus close to either the input or output face of the crystal, although not necessarily exactly at the face. Therefore, the crystal was simply placed at different positions close to the focus until the optimum position was found. At the optimum position the efficiency of the SHG was 53 %, using an input power of 5.5 W.

4 SCG - Supercontinuum generation

Part of the 1030-nm light is spectrally broadened through supercontinuum generation. A part of the supercontinuum will then be amplified in the NOPA. The wide spectrum is necessary to obtain the shortest possible pulses, and to choose the correct spectral content in order to obtain the desired SWIR wavelength via DFG. This section begins by discussing third-order nonlinear effects, which are the main cause of SCG. Then, the theory of SCG will be covered, and intensity calculations will be performed (to prevent damage to the crystal). After this, results of the investigations of SCG will be presented, and finally the setup for guiding the supercontinuum towards the NOPA.

4.1 Third-order nonlinear effects

As will be shown, SCG is mainly the result of third-order nonlinear effects. A medium without a second-order nonlinearity should therefore be used, so that the $\chi^{(3)}$-tensor will be the leading nonlinearity. The nonlinear polarization density $\mathbf{P}_{\mathrm{NL}}(t)$ of a third order nonlinear medium is given by

$$\mathbf{P}_{\mathrm{NL}}^{(3)} = \epsilon_0 \chi^{(3)} \mathbf{E}^3. \tag{38}$$

If a monochromatic wave $\mathbf{E}(t) = \frac{1}{2}[\mathrm{E}(\omega)\exp(i\omega t) + \mathrm{E}^*(\omega)\exp(-i\omega t)]$ travels through the material, two components of $\mathbf{P}_{\mathrm{NL}}(t)$ at frequencies ω and 3ω will be obtained, as given by equations (39) and (40) [15].

$$P_{\mathrm{NL}}(\omega) = 3\chi^{(3)}|\mathrm{E}(\omega)|^2\mathrm{E}(\omega) \tag{39}$$

$$P_{\mathrm{NL}}(3\omega) = \chi^{(3)}\mathrm{E}^3(\omega) \tag{40}$$

What is of interest here is the component at ω, $P_{\mathrm{NL}}(\omega)$. Equation (39) is of the same form as equation (27), $\mathbf{P} = \epsilon_0\chi\mathbf{E}$, which is a linear relation. The nonlinear response is therefore seemingly linear, with the coefficient $3\chi^{(3)}|\mathrm{E}(\omega)|^2$, where $|\mathrm{E}(\omega)|^2$ is proportional to the intensity. This can be interpreted as an intensity-dependent change in the susceptibility of the material, due to the third-order nonlinear effect. Since the refractive index is related to the susceptibility χ, this means that the nonlinear response will modify the refractive index. This can be shown by noting that equation (39) corresponds to a change in susceptibilty $\Delta\chi$, as given by [15]

$$\epsilon_0\Delta\chi = \frac{P_{\mathrm{NL}}(\omega)}{\mathrm{E}(\omega)} = 3\chi^{(3)}|\mathrm{E}(\omega)|^2 = 6\chi^{(3)}\eta I, \tag{41}$$

where η is the impedance of the medium.

The susceptibility is therefore dependent on the intensity $I = |\mathrm{E}(\omega)|^2/2\eta$ of the wave [15]. Since the refractive index n is related to the susceptibility as $n = \sqrt{1+\chi}$ [15], it results in an intensity-dependent refractive index, as given by [15]

$$\Delta n = \frac{3\eta}{\epsilon_0 n}\chi^{(3)} I = n_2 I, \tag{42}$$

where n_2 is the nonlinear refractive index. The intensity-dependent refractive index can then be expressed as [15]

$$n(I) = n + n_2 I, \tag{43}$$

which shows that the third-order nonlinear effect indeed modifies the refractive index, and this change is dependent on the intensity. This is called the optical Kerr effect [15].

Another third-order nonlinear effect is four-wave mixing (FWM). Similar to the second-order nonlinear case, consider an electric field that is the sum of three harmonic components:

$$\begin{aligned}\mathbf{E}(t) =& \frac{1}{2}[\mathrm{E}(\omega_1)\exp(j\omega_1 t) + \mathrm{E}(\omega_1)^*\exp(-j\omega_1 t)] + \\ & \frac{1}{2}[\mathrm{E}(\omega_2)\exp(j\omega_2 t) + \mathrm{E}(\omega_2)^*\exp(-j\omega_2 t)] + \\ & \frac{1}{2}[\mathrm{E}(\omega_3)\exp(j\omega_3 t)) + \mathrm{E}(\omega_3)^*\exp(-j\omega_3 t)].\end{aligned} \tag{44}$$

Inserting equation (44) into equation (38) gives the the nonlinear polarization density due to the three harmonic components. This will just as for the second-order nonlinear effect (equations (31) - (35)) give a sum of different frequency components. One of these components is [15]

$$P_{\mathrm{NL}}(\omega_1 + \omega_2 - \omega_3) = 6\chi^{(3)}\mathrm{E}(\omega_1)\mathrm{E}(\omega_2)\mathrm{E}^*(\omega_3)\cos((\omega_1 + \omega_2 - \omega_3)t). \tag{45}$$

A fourth wave is therefore created at the frequency ω_4, as given by equation 46. The corresponding phase-matching condition is given by equation 47 [15].

$$\omega_4 = \omega_1 + \omega_2 - \omega_3 \tag{46}$$

$$\mathbf{k}_1 + \mathbf{k}_2 = \mathbf{k}_3 + \mathbf{k}_4 \tag{47}$$

As will be explained later in section 6.1, a CEP-stable laser usually produces a CEP-stable supercontinuum. This will be shown using the four-wave mixing process.

4.2 Supercontinuum generation

A supercontinuum is used as the signal for the NOPA. A supercontinuum is created when an intense laser pulse passes through a crystal exhibiting the Kerr effect [21]. The Kerr effect causes several modifications to the beam propagation, which, all together, lead to a significant spectral broadening of the fundamental pulse. Initially, the pulse is spectrally broadened mainly through self-phase modulation (SPM). According to equation (43), the refractive index is intensity dependent in a material with a third-order nonlinearity. The change in phase $\Delta\phi$ when propagating a distance z through a medium is given by $\Delta\phi = k\Delta z$, assuming a linear medium. What is important here is that the change in phase depends on the refractive index through the wavenumber k. Since the refractive index of a Kerr medium depends on the intensity, this means that the change in phase will also depend on the intensity. The instantaneous frequency ω, which is the time derivative of the phase, will therefore depend on the derivative of the intensity according to [22]

$$\omega = -\frac{\partial\phi}{\partial t} = \omega_0 - n_2\frac{\omega_0}{c}L\frac{\partial I(t)}{\partial t}, \tag{48}$$

where ω_0 is the initial frequency and L is the propagation distance in the medium.

The instantaneous frequency will therefore be shifted, depending on the derivative of the intensity. The intensity increases for the leading part of the pulse, so the leading part will be shifted towards red frequencies, while the trailing part is shifted towards blue frequencies due to the decreasing intensity. The SPM will in this way create a chirped pulse with a broadened spectrum. This is shown in figure 14. The broadening will generally be greater for a shorter pulse, since the intensity changes more rapidly.

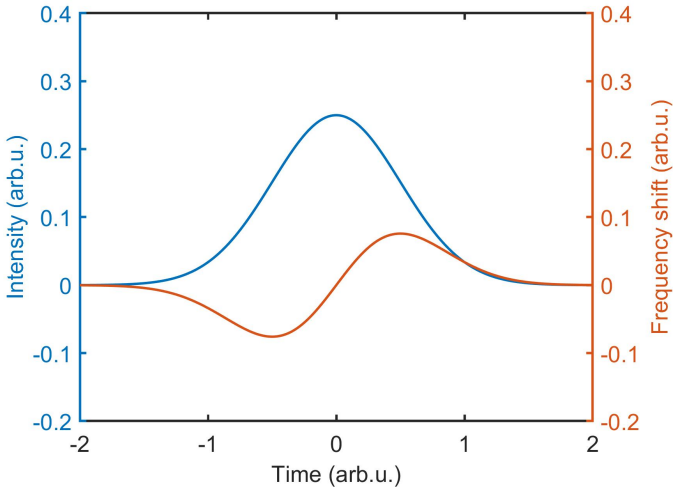

Figure 14: Illustrative figure of self-phase modulation (not to scale). The blue line is the intensity envelope of the pulse and the orange line is the resulting frequency shift.

Since there is also a spatial variation of intensity across the beam profile, the Kerr effect will result in a refractive index that varies spatially. Since the beam is most intense in the center, the refractive index will be larger at the center, and thus the index profile will be that of a positive lens. The material will therefore act as a lens under the influence of the strong beam, which causes the beam to experience self-focusing (SF) as it propagates through the material. There is a critical power P_{cr} for SF to occur, as given by [21]

$$P_{cr} = \frac{3.77\lambda_0^2}{8\pi n_0 n_2}, \tag{49}$$

for a Gaussian beam. If the power is less than P_{cr}, the focusing effect will not overcome the diffraction of the beam and the beam will diverge [21]. On the other hand, if the peak power is much greater than P_{cr} the pulse may break into several filaments [22]. Too high power may also cause the pulse to be ripped into two pulses due to dispersion [16].

The critical power describes the extreme case of an infinitely large medium and the collapse of the incoming beam at infinity [21]. In reality the power used is always higher than the critical power and the beam is also focused into the crystal (the focusing will be explained in the following), in order to have the theoretical collapse point at a realistic distance, on the scale of mm [21]. Also, P_{cr} is in practice larger than what is predicted by equation (49). This is a result of group velocity dispersion (equation (17), $\sigma_\tau = |D_\lambda|\sigma_\lambda z$). The pulse is stretched as it propagates through the medium, and this causes a reduction of the power of the pulse, since the energy is distributed over a longer time. The power therefore needs to be higher than P_{cr} to compensate for this. Shorter pulses have a wider bandwidth σ_λ according to equation (4), so the stretching becomes more severe and thus the power needs to be higher the shorter the pulse is [21]. However, for the 400 fs pulses and the few mm thick YAG crystal that will be used here, the pulse stretching due to dispersion is negligible.

The collapse point (where the beam theoretically collapses to a singularity) due to self focusing is given by [21]

$$z_f(P) = \frac{0.367ka_0^2}{((\sqrt{P/P_{crit}} - 0.852)^2 - 0.0219)^{1/2}}, \tag{50}$$

where a_0 is the beam waist at the 1/e-level at the input of the medium. The beam is assumed to be collimated, with the waist at the input, and the distance is the distance into the medium, starting from the input face.

As it turns out, this distance is rather long. Assuming a wavelength of 1030 nm, a beam waist of 200 µm, and $P/P_{crit} = 1.1$ gives a distance of $z_f(P) = 69$ cm. Such a long crystal would be highly impractical, introduce severe dispersion and be tremendously expensive. A thinner crystal can be used if the beam is focused beforehand with a lens. The collapse point will then be located at the point z_f' as given by [21]

$$z_f' = \frac{z_f f}{z_f + f}, \tag{51}$$

where f is the focal length of the lens. This means that $z_f' \leq z_f$ and $z_f' \approx f$ if $f \ll z_f$.

Because of self-focusing the intensity of the beam will increase. The intensity will eventually be high enough for multi-photon ionization (MPI) to occur, where several photons are simultaneously absorbed to ionize an atom or molecule, even if the bandgap is significantly larger than the photon energy. The creation of free electrons will cause the refractive index to decrease, as given in the Drude approximation by [21]

$$\Delta n_e = -\frac{2\pi e^2 N_e}{n_0 m_e(\omega_{laser}^2 + \nu^2)}, \tag{52}$$

where N_e is the electron density, ω_{laser} is the angular frequency of the laser and ν is the electron collision frequency (the frequency at which the free electrons collide). The decrease in refractive index due to free electron generation will counteract the effect of self-focusing and at some point multi-photon ionization and self-focusing will balance each other. At this point, the beam will be self-guiding, that is, the diameter of the beam will be constant. This process is visible as a very thin, colorful filament in the crystal. The beam will suffer a decrease in power during filamentation, due to the pulse being temporally stretched by dispersion, and also, to a lesser degree, light absorption

by the free electrons generated by MPI. Eventually the power will be lower than the critical power P_{cr}, at which point the beam will start to diverge due to diffraction. This will stop the filamentation process. The filament typically is a few millimeters long. The process of self-focusing, filamentation and finally diffraction is illustrated in figure 15. As previously mentioned, if the power is too high, the pulse will break up into several filaments. This is called multifilamentation.

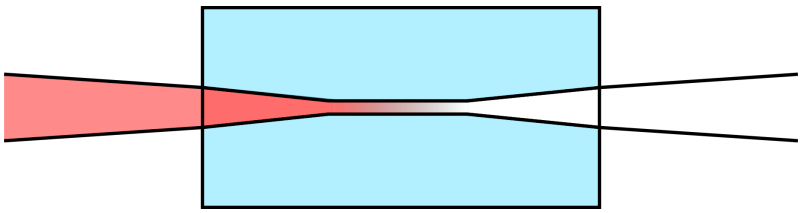

Figure 15: Illustrative figure of the supercontinuum generation process. The focused beam first experiences self-focusing until the intensity is high enough for filamentation to occur. During the filamentation, power is absorbed by free electrons caused by MPI, until the intensity is too low for self-focusing, which causes the beam to diverge.

Yet another result of the Kerr effect is self-steepening. Since the group velocity also depends on the refractive index (equation (15)), the most intense part (the central part) of the pulse will also travel the slowest. That means that the leading edge of the pulse will stretch out, whereas the trailing part of the pulse will run into the central part, resulting in self-steepening of the trailing (blue) edge of the pulse. This will contribute to the broadening of the pulse towards blue frequencies [16]. Self-steepening is illustrated in figure 16.

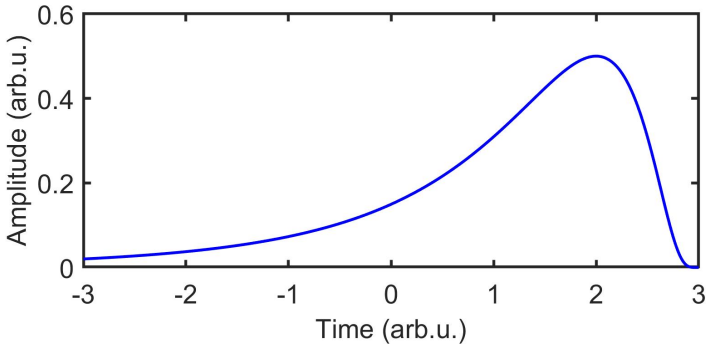

Figure 16: Illustrative figure of self steepening (not to scale). The peak of the pulse will experience a larger relative delay than the edges of the pulse, which causes a rapid change in amplitude towards the trailing edge of the pulse.

It has been shown [21] that most of the broadening occurs in the filament, and is the result of self-phase modulation in combination with multi-photon ionization. While self-phase modulation contribute to broadening towards both longer and shorter wavelengths (figure 14), multi-photon ionization will mostly give broadening towards shorter wavelengths. The broadening due to multi-photon ionization is a result of the reduction in refractive index it causes (equation (52)), which will affect the rate at which the phase changes, $\frac{\partial \phi}{\partial t}$. The broadening by multi-photon ionization and self-phase modulation is therefore both caused by the same mechanism, and depends on the phase. Note that, according to equation (48), self-phase modulation leads to an increase of the instantaneous frequency when the time derivative of the intensity of the pulse is negative. A decrease in intensity causes a decrease in refractive index as well (equation (43)), so the broadening by SPM towards higher frequencies is caused by a decreasing refractive index. Since multi-photon ionization also causes a rapid drop in refractive index, this shows that MPI will lead to broadening towards higher frequencies as well. The broadening by MPI is quite significant, since the generation rate of free electrons due to MPI is proportional to I^N, where N is the required number of photons to overcome the ionization potential [21]. This will cause a rapid increase in free electrons N_e around the peak of the pulse, which will, according to equation (52), cause a rapid drop in refractive index and thus significant broadening towards shorter wavelengths. Since multi-photon ionization, and self-steepening as well, mainly cause broadening towards higher frequencies, the broadening will be

asymmetrical. Indeed, typical supercontinua exhibit an intensity plateau at their high-frequency edge [23].

Supercontinuum generation requires high powers, which may cause damage to the crystal. Whether or not damage occurs depends on e.g. the intensity, the repetition rate and the medium that is used. The intensity is given by $I = P/A = E/\tau/A$, in the simplifying assumption that the energy E is constant during the pulse duration τ and over the beam area A. That means that even a pulse with a seemingly low pulse energy in the µJ range may have a huge intensity, if the duration is in the fs range and the area is in the μm^2 range (which is a common situation at the focus). This will result in the generation of a large amount of free electrons through multi-photon ionization. If a very large number of free electrons is generated, a large amount of energy will also be released as the electrons recombine, which can lead to rapid expansion, disruption, melting, etc. This is how damage may be caused by a single laser shot. Damage may also be the accumulative effect of several shots, which is especially a problem at high repetition rates. In this case it is often a thermal effect, since a high intensity, high repetition rate laser will also have a high average power. This will heat the crystal. As previously stated, there is a critical **power** P_{cr} at which self focusing occur, but it is the **intensity** that determines whether or not the crystal will be damaged. As long as the power is greater than P_{cr}, the supercontinuum will be generated, regardless of the intensity (to a certain extent). The damage is then determined by how tightly the beam is focused into the crystal.

To summarize: A supercontinuum is generated when a strong laser pulse enters a Kerr medium. SPM will start to broaden the pulse spectrally, while self-focusing will decrease the beam waist leading to an increase in intensity. The continuous increase in intensity will provide a gradually stronger SPM, but eventually also cause multi-photon ionization of the dielectric. Hence, the generated plasma decreases the refractive index and counteracts self-focusing. During supercontinuum generation, both effects balance each other and result in a self-guiding of the beam in a narrow plasma channel (the filament) for several millimeters. Self-steepening and the refractive index modulation due to MPI lead to an overall asymmetric broadening towards short wavelengths.

4.3 Damage threshold estimations

This paragraph presents considerations of the damage threshold of YAG and the peak intensity in the envisaged experiment, in order to avoid crystal damage. There are two parameters that must be determined, the average power P_{avg} and the focal length f of the focusing lens. The average power must be chosen so that the peak power of the pulse is higher than the critical power but not so high that multifilamentation occurs. From this the peak power will be used to find a suitable focal length of the focusing lens. The focal length should be chosen to give a short distance inside the crystal before filamentation occurs, but an intensity that is not high enough to cause damage.

As touched upon in the introduction, reference [16] found that YAG is a suitable material for supercontinuum generation. Of the different materials that were tested, it had a relatively low critical power of 2.0 - 3.2 MW. At powers above $3.2P_{cr}$, fringes appeared in the spectrum, most likely due to the pulse being split into two due to dispersion. For the other materials that were investigated, fringes appeared for powers much closer to P_{cr}. Furthermore, the spectrum of the supercontinuum generated in YAG had a plateau at around 600 - 900 nm, which is suitable for the 620 - 750 nm range that is desired. YAG also has a high damage threshold. In reference [16] it was found that the damage threshold of YAG was $> 10P_{cr}$. All these properties makes YAG a suitable choice.

The power used in the experiment should be higher than the critical power, in order to reduce the distance before filamentation. For this reason, a peak power of $P_{peak} = 7.5$ MW is chosen. The 1030-nm light source that is used has a pulse duration of $\tau_{\mathrm{FWHM}} \approx 400$ fs and a repetition rate of $F_{rep} = 200$ kHz. The desired average power P_{avg} can be calculated as $P_{avg} = P_{peak} F_{rep} \tau_{\mathrm{FWHM}}$. This gives $P_{avg} = 600$ mW.

The next step is to find a suitable focal length. The shorter the focal length, the more tightly the beam will be focused. This will make the beam waist narrower at the focus, which will increase the intensity. For a collimated beam, the beam waist w_0' at the focus is given by [15]

$$w_0' \approx \frac{\lambda}{\pi w_0} f, \tag{53}$$

where w_0 is the waist of the incident beam. The collimated incident beam has a diameter of approximately $2w_0 = 3$ mm. Using equation (53) with focal lengths 40 mm and 80 mm gives

the waists $w_0' = 8.8\,\mu\text{m}$ and $17.5\,\mu\text{m}$ at the focus, respectively. The focal lengths are chosen since they are in the range that is commonly used for supercontinuum generation. This can be used to calculate the effective area A_{eff} of the beam, which is given by [4]

$$A_{eff} = \frac{\pi w^2}{2}, \tag{54}$$

where the factor of 2 is due to the assumed Gaussian profile. The intensity at the focus can then finally be calculated as

$$I = \frac{P_{peak}}{A_{eff}}, \tag{55}$$

according to [4]. For this $P_{peak} = 7.5$ MW (corresponding to 600 mW of average power) was used. For $f = 40$ mm the result is $I = 4.75 \cdot 10^{12}$ W/cm^2 and for $f = 80$ mm the result is $I = 1.27 \cdot 10^{12}$ W/cm^2.

The surface damage threshold of YAG was investigated in [24], where a wavelength of 800 nm was used. At a pulse duration of 297 fs, the damage threshold is 4.31 J/cm^2 at a single shot. That corresponds to an intensity of $1.45 \cdot 10^{13}$ W/cm^2. That is about 10 times higher than the intensity obtained with an 80-mm focal length lens, and about 3 times higher than with the 40-mm focal length lens. This threshold was however obtained at a shorter wavelength than what will be used here, so it may not be entirely accurate. It is probable that the damage threshold for longer wavelengths is even higher (since their photon energy is further away from the band gap). This shows that both an 80-mm or a 40-mm focal length lens would probably be safe to use. The 40-mm focal length lens would be the better choice, since it will provide a tighter focusing and therefore the filamentation will start earlier in the crystal.

The bulk damage is much harder to calculate. Because of the nonlinear effects in the crystal, the pulse is significantly focused and deformed. These changes can not be estimated very well by hand calculations, and the entire process must be simulated which is rather complicated. However, supercontinuum generation in a YAG crystal has been reported repeatedly [17, 23, 25]. If a careful approach is used, where the power is slowly increased, starting below P_{th}, it should be possible to avoid any damage.

4.4 Experimental investigations of supercontinuum generation

The power levels and focal lengths that were found in the previous section can now be used to experimentally investigate supercontinuum generation. For this part I worked together with my supervisors. I aligned optics, tested various lenses and crystals and made measurements. The setup for investigating supercontinuum generation is shown in figure 17. The light was guided from the compressor using two mirrors (not shown). An iris was then used to reduce the power and a lens focused the light into the YAG crystal. An $f = 50$ mm lens collimated the resulting supercontinuum. Two dichroic mirrors (with a cut-off wavelength at 900 nm) were used to filter out the much more intense infrared light. The spectrum was studied with a fiber-coupled compact spectrometer.

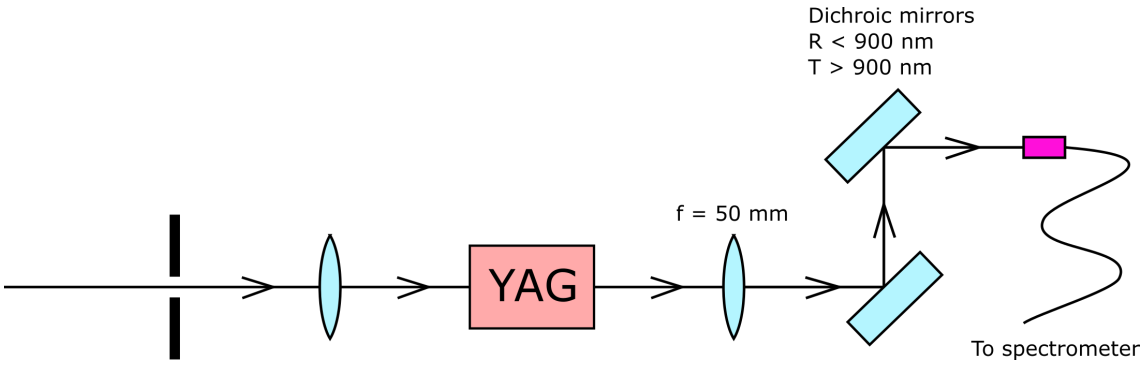

Figure 17: Setup for generation of supercontinuum. An iris is used for power attenuation and a lens focuses the beam into the YAG crystal. The supercontinuum is collimated and the fundamental light at 1030 nm is filtered out with two dichroic mirrors.

In reference [25], it is noted that for a wavelength of 1030 nm and 200 - 400 fs pulses, a 4 - 6-mm thick YAG crystal is a suitable choice for supercontinuum generation. It is stated that this will provide a stable spectrum without damaging the crystal. Therefore, to find the optimum focal length of the focusing lens, a 4-mm-thick YAG crystal was used. Three different focal lengths were tested: 50 mm, 75 mm and 100 mm. To try a different material a piece of 5-mm-thick BK-7 glass was also tested with the 75 mm focal length lens. The BK-7 glass was anti-reflection coated, whereas the YAG crystal was uncoated. The input power and the position of the focus was adjusted to obtain the optimum (flattest) spectrum. The result is shown in figure 18.

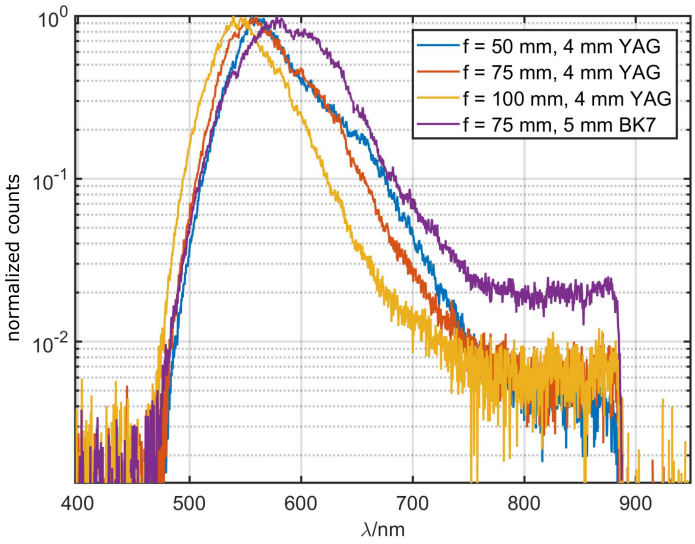

Figure 18: Spectra of the supercontinuum from a 4-mm-thick YAG crystal and 5-mm-thick BK-7 glass. The power and focusing was adjusted to optimize the spectrum.

Supercontinuum spectra are generally presented on a logarithmic scale, since the supercontinuum is much weaker than the fundamental light. However, in this case the fundamental is filtered out. Nevertheless, the logarithmic scale will still be used, since it simplifies comparison with spectra from other sources. The supercontinuum also varies considerably in magnitude over the spectrum, so the logarithmic scale will also show the weaker parts of the spectrum. As can be seen from figure 18, the spectrum shifts slightly towards longer wavelengths when the focal length decreases. A shorter focal length also seems to widen the spectrum slightly. BK7 shows more broadening towards longer wavelengths and produces a spectrum that is wider than that for YAG. This may however be down to the fact that the BK-7 glass is 1 mm thicker than the YAG crystal and therefore can support a longer filament. A short focal length lens seems to be the best choice for this application, since the 50-mm focal length lens gives the longest central wavelength and the widest spectrum. None of these spectra are satisfactory however. The desired wavelength range of the supercontinuum is around 620 - 750 nm. As will be shown later, this will result in a spectrum in the SWIR range after the DFG. The spectra shown here are centered at 550 - 600 nm, which is too short. Also, the spectra are not as flat as desired.

The average input power (the power after the iris) and the average power of the supercontinuum was measured with a powermeter. The result is listed in table 1. It is clear from the table that the 50-mm focal length lens requires the least amount of power and also has almost as good conversion efficiency P_{SC}/P_{in} as the $f = 75$ mm case. However, in all of the cases the conversion efficiency is very low. Note also that the optimal input power is higher than the expected 600 mW. The 50-mm focal length lens requires the least amount power, but it is still at 900 mW and that is too much in contrast to the expected power requirement.

It is possible that a thicker crystal would provide a more ideal spectrum, since such a crystal can support a longer filament. The spectrum of the 5-mm-thick BK7 glass in figure 18 would suggest this. Therefore, the spectra from 4- and 8-mm-thick YAG crystals were compared under the same conditions. The result is shown in figure 19. For both YAG crystals a 75-mm focal length lens along with 1.27 W of input power was used. The 8-mm-thick crystal generates a much flatter spectrum than the 4-mm-thick crystal in the region of interest (620 - 750 nm). Furthermore, the

f	P_{in}	P_{SC}	P_{SC}/P_{in}
50 mm	0.9 W	0.66 mW	0.073 %
75 mm	1.09 W	0.84 mW	0.077 %
100 mm	1.4 W	0.66 mW	0.047 %

Table 1: Measured average powers and conversion efficiency.

peak of this part of the spectrum is located at a longer wavelength than the peak of the same part of the spectrum from the 4-mm-thick crystal. The spectrum was also stable. The power of the supercontinuum was 2.5 mW for the 8-mm-thick crystal and 1.2 mW for the 4-mm-thick crystal (which is higher than for the previous measurement, but the input power is also higher). Therefore, an 8-mm-thick YAG crystal seems like a good choice for the supercontinuum generation.

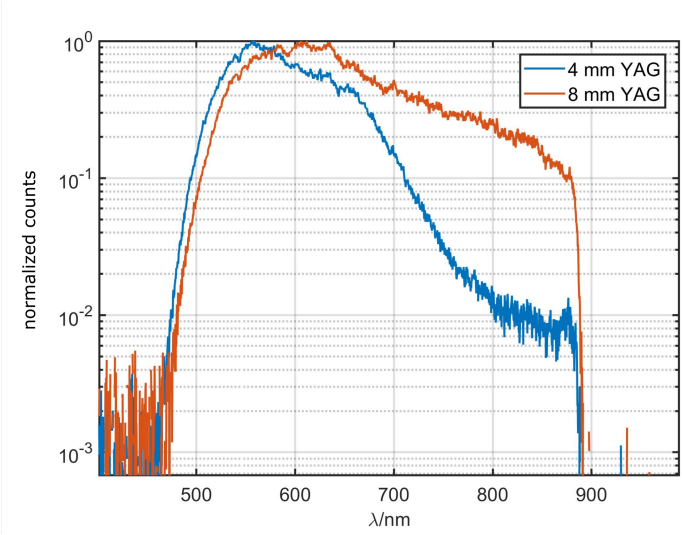

Figure 19: Spectra of the supercontinuum from 4- and 8-mm-thick YAG crystals, using 1.27 W of power and a 75 mm focal length lens.

The 8-mm-thick YAG crystal was also tested with focusing lenses with focal lengths 50 mm, 75 mm and 100 mm. One of the dichroic mirrors in the setup shown in figure 17 was removed, since it was not necessary to attenuate the fundamental light that much. The result is shown in figure 20.

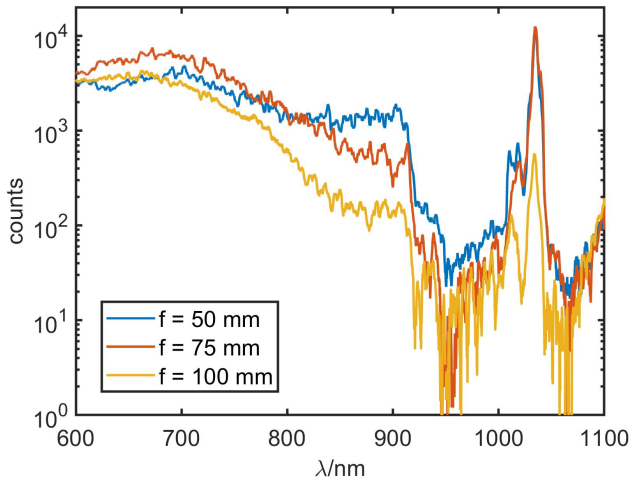

Figure 20: Spectra of the supercontinuum from an 8-mm-thick YAG crystal for different focal length lenses. The power was adjusted to optimize the spectrum.

For $f = 50$ mm the flattest spectrum is obtained, with a peak at around 700 nm. If this is compared to the spectrum from the 4-mm-thick YAG crystal (figure 18), the spectrum is now far wider and also centered at the desired wavelength. The flattest spectrum is obtained when the crystal is placed roughly with the input face at the focus of the lens. When the crystal is moved towards the lens so that the geometrical focus is located inside the crystal, a peak is created in the spectrum (resulting in a less flat spectrum). As the focus is moved further inside the crystal the peak is shifted towards shorter wavelengths. When the spectrum has a peak it is also the most stable and the supercontinuum will have a green or yellow color. On the other hand, when the supercontinuum is red, it flickers and becomes unstable. Since red light has a longer wavelength, this indicates less self-phase modulation than when the supercontinuum is green or yellow. This would correspond to a shorter, less stable, filament that is aborted by the end facets before it can reach a stable configuration. This is not optimal, since the red supercontinuum has the most desirable spectrum. For the reliable operation of a NOPA, it is, however, more important to generate a stable seed source. The input power to obtain the optimal spectrum was 1 W. The conclusion would be that for this application, an $f = 50$ mm lens, 8-mm-thick YAG crystal and 1 W of power is the optimal choice to obtain the best spectrum.

However, 1 W of input power is more than what is expected from theoretical considerations. The preferable choice is 600 mW. As it turns out, when studying the beam profile of the pump beam, the beam quality was less than optimal. The degradation of the spatial properties of the pump pulses resulted from a misalignment of the compressor configuration. The mode was spatially chirped, which had a negative effect on the generation of a supercontinuum. Any residual chirp was removed from the pump pulses by re-aligning the compressor gratings. The improved beam quality allows for stable continuum generation at the expected average power of approximately 0.6 W. Note that the spectra in figures 18 - 20 were measured before the correction of the grating compressor was made. The spectra that will be presented in the following were however obtained after the correction.

Since the YAG crystal was uncoated, the continuum generation might suffer from reflection losses. It is therefore of interest to minimize these losses. This can be done by placing the crystal at the Brewster angle, which is an angle of incidence at which p-polarized (electric field parallel to the plane of incidence) light is completely transmitted [15].

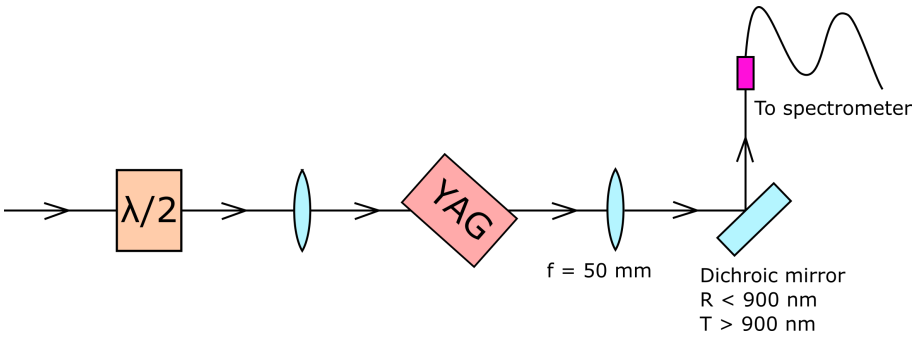

Figure 21: Setup for supercontinuum generation at Brewster angle. The $\lambda/2$-plate is used to rotate the polarization, so the YAG can be placed at the Brewster angle in a safe way.

To investigate the effect of placing the crystal at the Brewster angle, the setup in figure 21 was used. It is the same as for the investigations of the 8-mm-thick YAG crystal, but the iris is replaced with a half-wave plate ($\lambda/2$), in order to rotate the polarization by 90°. The rotated polarization will then eliminate reflections when the crystal is placed at the Brewster angle, since the light from the laser is supposedly linearly polarized (a polarizer can be used to check the polarization of the light, which will also be done later). If the polarization had not been rotated the crystal would have to be angled upwards, which is dangerous since any reflection would not be contained to the plane of the table. The iris would not be needed to attenuate the light, since the laser source was set directly to the desired power of 600 mW for these investigations. Higher input power than 600 mW was used for the previous experiments without any damage, so 600 mW of input power should be safe to use. The crystal was also placed at normal incidence for comparison.

Because of the relatively large Brewster angle of 61.5° [26] the mounting of the YAG crystal had to be placed in such a way that it was not possible to fit the 50-mm focal length lens. Figure 22 shows the spectra at Brewster angle. It shows as before that a shorter focal length lens gives a

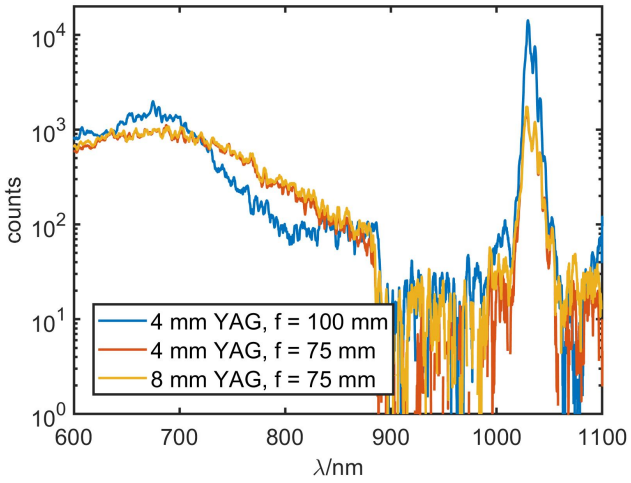

Figure 22: Spectra at Brewster angle using 600 mW of power.

flatter, wider spectrum. However, with a lower power of 600 mW and an improved beam quality, there is very little difference between the spectrum of the 4- and the 8-mm-thick YAG crystals. It was also noted that when the crystal was rotated from normal incidence to the Brewster angle, a ring-like pattern emerged in the beam profile. The beam profile was therefore worse at the Brewster angle than at normal incidence. The power of the white light at Brewster angle with 600 mW of input power and a 75-mm focal length lens was 2.2 mW, for both 4-mm and 8-mm-thick YAG crystals. For the same conditions, but at normal incidence, the power of the white light was 2.3 mW for a 4-mm-thick crystal and 2.4 mW for an 8-mm-thick crystal. Compared to the previous case (when the beam had a spatial chirp), the average pump power is reduced by a factor of two and the output power is increased by a factor of 3-4. The conversion efficiency is now much higher, and there is much less difference in supercontinuum power between the different thicknesses. However, the power was higher at normal incidence, even though there would be more reflections. Part of the reason for this may be that the beam was not perfectly linearly polarized. When the half-wave plate was adjusted by minimizing the power of the beam through a polarizer, it was not possible to achieve zero power. Some power was therefore still reflected at Brewster angle. Another possibility could be that the refraction due to the angled surface with respect to the focus deteriorates the mode profile in the focus slightly, or influences self focusing (one side of the beam enters the crystal "earlier" at lower intensity than the other side). This may be the reason for the ring-like pattern in the beam profile that was previously noted. The power reflectance at normal incidence was also not more than 0.084 [26], so the gain in power would be quite small anyway.

Because of the higher power and better beam profile, it was decided to put the YAG crystal at normal incidence. Figure 23 shows the spectra for 4- and 8-mm-thick crystals using a 50-mm focal length lens. In complete contrast to before the spatial chirp was removed (figure 19), the spectra now look very similar. Both thicknesses produce very similar spectra at the same power. Subsequently, it is chosen to work with the thinner 4-mm-thick crystal, since it will introduce less dispersion and hence minimizes the chirp. The reason for the now very similar spectra is most likely due to the removed spatial chirp. Before the improvement, the spectrum from the 4-mm-thick crystal was much narrower than the spectrum from the 8-mm-thick crystal. This would suggest a shorter filament in the 4-mm-thick crystal which is interrupted at the end facet of the crystal, resulting in less broadening. After the improvement, however, the spectra were much more alike. The filament in both crystals would therefore be equal in length. This means that the filamentation process starts earlier in the crystal with the improved beam quality, and that the filament is short enough to fully fit in the 4-mm-thick crystal as well as in the 8-mm-thick crystal.

An important aspect of the supercontinuum is the stability. Throughout all measurements it could be noted that the spectrum fluctuated the most when the beam had a red color. Changing the focusing conditions so that the spectrum became yellow or green, made it look more stable. There were no visible fluctuations. A stability measurement was also made. This was done by measuring the supercontinuum spectrum consecutively 5000 times, using an 8-mm-thick YAG crystal and a 50-mm focal length lens. The result is shown in figure 24. The blue line shows the average

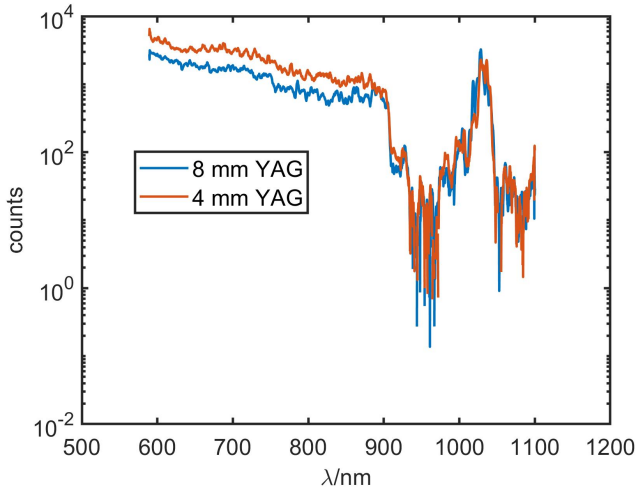

Figure 23: Spectra for 4-mm and 8-mm-thick YAG crystals at normal incidence using 600 mW of power and a 50-mm focal length lens.

number of counts at each frequency, and the orange line the average deviation from the average number of counts. The average deviation was calculated by determining the average number of counts at each wavelength, and then finding the magnitude of the deviation of the instantaneous number of counts, relative to the average number, at each wavelength, for each of the 5000 time points. The average of the deviations over time for each wavelength were then taken. As the figure shows, the average deviation is at least 1 order of magnitude lower than the average number of counts. It was however noted when studying the spectrum of the laser that the laser itself was fluctuating somewhat. Therefore, it is difficult to tell how much of the fluctuations are the result of an instability of the supercontinuum. Nevertheless, the fluctuations in figure 24 are not too severe. One of the reasons to why the spectrum of the laser was fluctuating, is that the laser source was operated at a lower power. The laser source is designed to provide up to 40 W of power, and running at these powers will give a more stable output. However, 40 W is a significant amount of power, so due to safety reasons the power was reduced when investigating the supercontinuum generation.

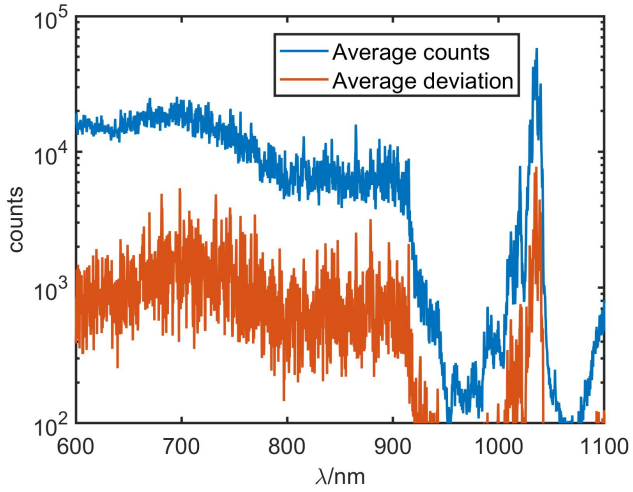

Figure 24: Stability of supercontinuum over 5000 measurements, using an 8-mm-thick YAG crystal and a 50-mm focal length lens. The blue line is the average counts and the orange line the average deviation from the average counts.

The conclusion of this section is that the best choice for this application is to use a 4-mm-thick YAG crystal at normal incidence, along with a 50-mm focal length lens. It is also very important

for the efficiency of the supercontinuum generation process to have a good beam quality.

4.5 Collimation and guiding of the supercontinuum

It has been noted that when a supercontinuum is generated, the divergence of the beam drastically increases [23]. The supercontinuum is therefore quite divergent, and must subsequently be collimated. Collimation of the supercontinuum is done by placing a lens at a distance equal to the focal length away from the YAG crystal. A shorter focal length lens will thus result in a narrower collimated beam, since the beam will have less distance to diverge. The beam should then be further reduced in size with a telescope, to roughly match the mode diameter of the SHG pump beam in the NOPA crystal. Finally, the beam is guided towards and focused into the crystal for the NOPA. Figure 25 shows the setup for this. An achromatic 30-mm focal length lens was used for collimation. The telescope consisted of an $f_1 = 200$ mm focal length concave mirror and one $f_2 =$ -37.5 mm focal length convex mirror. The mirror separation in the telescope should be the sum of the focal lengths: $200 - 37.5 = 162.5$ mm. The magnification of the telescope is then $f_2/f_1 = -37.5/200 = -0.1875$ [27]. The beam is guided from the telescope to a delay stage. This consists of two mirrors at 90° angle, mounted on a translational stage. The mirror pair can be moved forward and backward, which makes it possible to adjust the path length of the supercontinuum. This is necessary since the pathlength of the signal and the pump must be the same in order for them to overlap in the NOPA. After the delay stage a dichroic mirror is used to remove much of the infrared light. The light is then guided by a mirror and a focusing mirror with $f =$ 250 mm to the NOPA crystal.

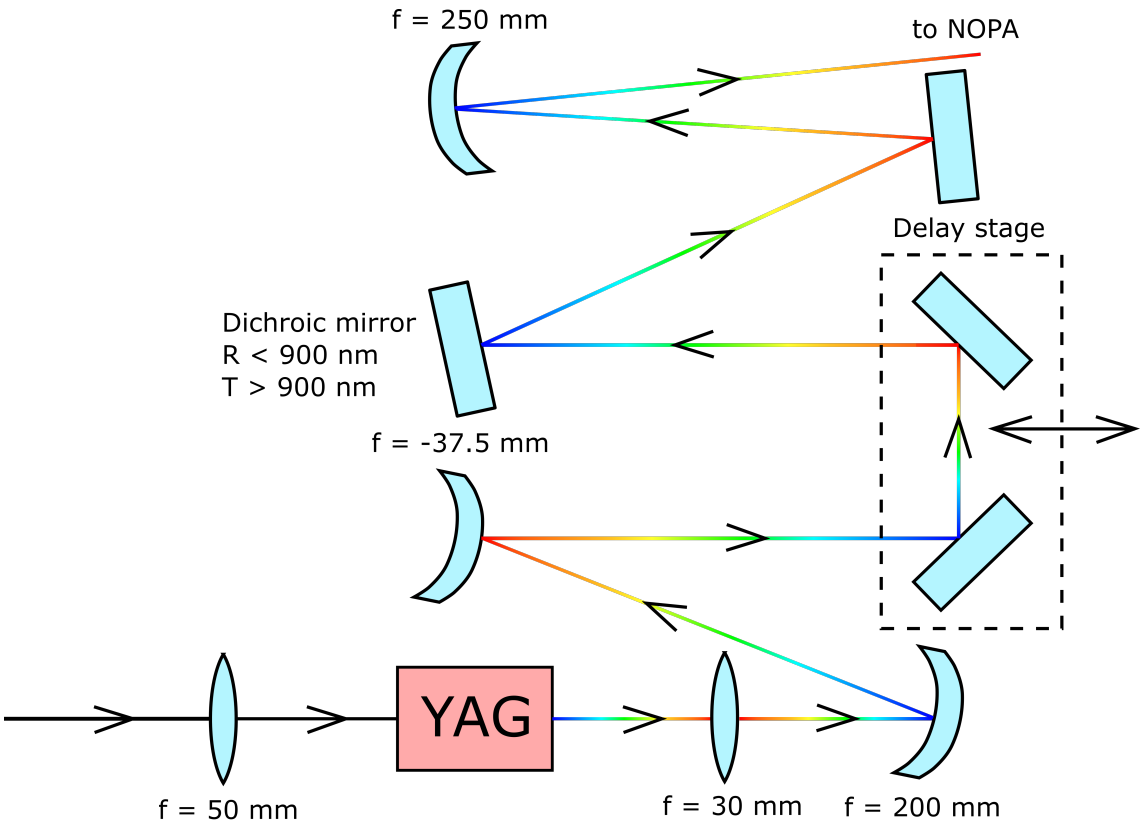

Figure 25: Final setup of WLG to NOPA. The infrared light is focused into the YAG crystal and the supercontinuum is collimated with the 30-mm focal length lens. A telescope is used to further reduce the beam size. The delay stage features a mirror pair, mounted on a translational stage, that can be used to adjust the pathlength of the supercontinuum to the NOPA. A dichroic mirror is used to remove the remaining infrared light. Finally, a 250-mm focal length concave mirror is used to focus the supercontinuum into the NOPA crystal.

5 NOPA - non-collinear optical parametric amplifier

Both the signal and the pump for the NOPA have now been generated. The NOPA will be implemented by focusing both beams into a nonlinear crystal, where an energy transfer occurs, which results in the supercontinuum being amplified. This section begins by presenting the theory of the NOPA, followed by simulations of the amplifier gain. Then the experimental results of the implemented NOPA are presented. To finish the section, an overview of the entire setup is shown.

5.1 Optical parametric amplification

Optical parametric amplification (OPA) is a second-order nonlinear effect, where an intense beam with angular frequency ω_3 (the pump) distributes some of its energy to a weaker beam with angular frequency ω_1 (the signal), as both beams travel through a second-order nonlinear medium [15]. To satisfy frequency and phase-matching conditions, a third beam (the idler) is also generated at angular frequency ω_2. The angular frequencies of the waves are related by equation (36), $\omega_3 = \omega_1 + \omega_2$. The idler is therefore generated through difference-frequency generation between the pump and the signal. Just as for the SHG, the phases will also need to be matched according to the phase-matching condition $\mathbf{k}_3 = \mathbf{k}_1 + \mathbf{k}_2$ (equation (37)).

The process can be thought of as a pump photon of angular frequency ω_3 being split into two photons with angular frequencies ω_1 and ω_2. The energy of the pump must be higher than that of the signal and idler for this to be possible, which means that the wavelength of the pump must be shorter than that of the signal. This is the reason why the pump beam in the NOPA setup is frequency doubled: It is not possible to amplify the white light with the 1030-nm light, since the white light has a shorter wavelength.

In a collinear geometry, all the wavevectors of the beams are parallel. This is what was used for the SHG. If instead the wavevectors are not parallel, the geometry is noncollinear and the process is hence called non-collinear OPA (NOPA). This means that the signal and the pump beam cross inside the crystal under a certain angle α, usually denoted as the non-collinear angle. As will be shown later, the NOPA geometry can provide a wider phase matching bandwidth, and therefore, it is the NOPA geometry that will be used here.

Just as for the SHG, the birefringent properties of the nonlinear medium can be used to satisfy the phase-matching condition. If appropriate polarizations of the signal and pump beams are chosen, the refractive index of the extraordinary beam $n_e(\theta)$ can be tuned according to [15]

$$\frac{1}{n_e(\theta)^2} = \frac{\cos^2\theta}{n_o^2} + \frac{\sin^2\theta}{n_e^2}, \tag{56}$$

by choosing a suitable phase-matching angle θ (n_o and n_e are the ordinary and extraordinary refractive indexes, respectively). As will be shown subsequently, θ depends on the chosen α, so the non-collinear geometry adds an extra degree of freedom. The NOPA will be designed for *Type I ooe* phase matching, where *Type I* means that the signal and the idler have the same polarization, and *ooe* indicates the polarization of the signal, idler and pump, respectively.

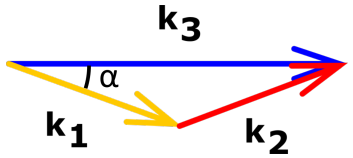

Figure 26: Non-collinear phase matching configuration. $\mathbf{k}_1$ - signal wavevector, $\mathbf{k}_2$ - idler wavevector, $\mathbf{k}_3$ - pump wavevector, α - non-collinear angle

In order to phase match a NOPA, the condition $\mathbf{k}_3 = \mathbf{k}_1 + \mathbf{k}_2$ must be fulfilled. Because of the non-collinear geometry, this is less straightforward than for the SHG. The geometry is shown in figure 26. The angle between $\mathbf{k}_1$ and $\mathbf{k}_3$ is the non-collinear angle α. This angle will remain fixed. Since the signal and idler are ordinary, the refractive index does not change with θ and consequently the length of the vectors $\mathbf{k}_1$ and $\mathbf{k}_2$ is therefore fixed. The length of $\mathbf{k}_2$ is obtained from the wavelength of the signal and the pump through equation (36). When θ is changed, the refractive index of the pump changes and therefore also the length of $\mathbf{k}_3$. This means that the phase-matching problem can be understood intuitively by looking at figure 26: When the phase

matching angle θ is adjusted, the length of $\mathbf{k}_3$ changes, while $\mathbf{k}_1$ remains stationary. The goal is then to find the length of $\mathbf{k}_3$ so that the distance between the tips of $\mathbf{k}_3$ and $\mathbf{k}_1$ equals the length of $\mathbf{k}_2$. The direction of $\mathbf{k}_2$ will then be set by the phase matching. Note that the direction of $\mathbf{k}_2$ will change depending on the wavelength of the signal, so for a broadband signal the idler will be angularly dispersed.

Mathematically, the condition on the wavevectors is $\mathbf{k}_2 = \mathbf{k}_3 - \mathbf{k}_1$. The components of $\mathbf{k}_2$ must therefore fulfill

$$\begin{cases} k_{2x} = k_{3x} - k_{1x} = |\mathbf{k}_3| - |\mathbf{k}_1| \cos\alpha \\ k_{2y} = k_{3y} - k_{1y} = 0 - |\mathbf{k}_1| \sin\alpha \end{cases} \tag{57}$$

From these two equations the length of $\mathbf{k}_2$ is

$$|\mathbf{k}_2|^2 = k_{2x}^2 + k_{2y}^2 = (|\mathbf{k}_3| - |\mathbf{k}_1| \cos\alpha)^2 + (|\mathbf{k}_1| \sin\alpha)^2 \tag{58}$$

Finally, this can be rewritten to find the desired length of $\mathbf{k}_3$:

$$|\mathbf{k}_3| = \sqrt{|\mathbf{k}_2|^2 - (|\mathbf{k}_1| \sin\alpha)^2} + |\mathbf{k}_1| \cos\alpha \tag{59}$$

When $|\mathbf{k}_3|$ has been determined, the relation $|\mathbf{k}_3| = 2\pi n_e(\theta)/\lambda_3$ can be used to find the desired refractive index $n_e(\theta)$. The angle θ can then be determined from equation (56), just as for the SHG. It is still difficult to find an explicit expression for θ from this equation, so it has to be solved numerically. From this, phase-matching curves for different non-collinear angles α can be calculated. A number of these curves for BBO with the pump wavelength $\lambda_3 = 515$ nm are shown in figure 27.

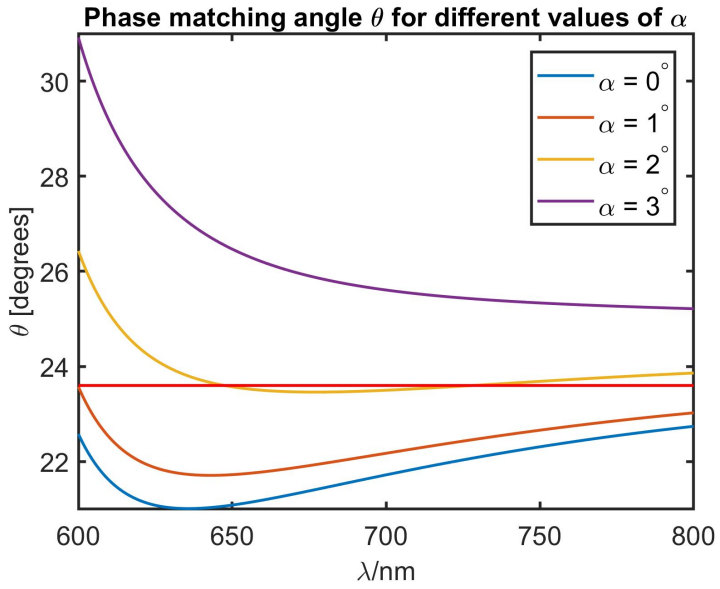

Figure 27: Phase-matching curves in BBO for 515 nm pump for different noncollinear angles α. The red line indicates the phase-matching angle.

These curves serve as an introduction to the concept of the phase-matching bandwidth. Since an ultrashort pulse has a wide bandwidth, it is important to also have a broadband amplifier. But as figure 27 shows, the required phase-matching angle θ at a certain non-collinear angle α changes with the wavelength λ. It is therefore not possible to have perfect phase-matching over the entire signal wavelength range. The idea is then to choose a curve that is as flat as possible in the desired wavelength range so that the wave vector mismatch $\Delta\mathbf{k} = \mathbf{k}_3 - \mathbf{k}_1 - \mathbf{k}_2$ is minimized. This gives a good initial estimate of the required θ and α. Figure 27 also shows why the non-collinear configuration is used: The curve at $\alpha = 2°$ is much flatter than the curve at $\alpha = 0°$ (collinear case), so the non-collinear configuration can provide a wider bandwidth. Note that the desired bandwidth is 620 - 750 nm. The phase-matching curve for $\alpha = 3°$ may be flatter than the one for $\alpha = 2°$, but it is flatter in the wrong range, so the phase-matching curve at $\alpha = 2°$ would be better

suited for this application (the exact value of α will be calculated later). The red line indicates a good phase-matching angle for $\alpha = 2°$. Perfect phase matching is obtained at two wavelengths.

The gain G of the NOPA depends on more parameters than just $\Delta\mathbf{k}$. It is therefore better to calculate the gain in order to estimate the resulting bandwidth of the amplified pulses. In reference [25], the gain for a medium of length L is given by

$$G = \frac{I_{1out}}{I_{1in}} = 1 + (\frac{\Gamma}{g}\sinh(gL))^2, \tag{60}$$

where

$$g = \sqrt{\Gamma^2 - \frac{|\Delta\mathbf{k}|^2}{4}} \tag{61}$$

and

$$\Gamma^2 = \frac{2\mathbf{d}_{\text{eff}}^2\omega_1\omega_2 I_3}{c^3\epsilon_0 n_1 n_2 n_3}. \tag{62}$$

Note that the gain predicted by equation (60) assumes that the pump is not depleted during the interaction. Other effects, such as light absorption in the crystal, are also ignored. The effective nonlinear coefficient is given by $\mathbf{d}_{\text{eff}} = d_{31}\sin\theta - d_{22}\cos\theta\sin 3\phi$ in BBO [25], where $d_{31} = 0.04$ pm/V and $d_{22} = 2.2$ pm/V [15]. The angle ϕ depends on how the beam is rotated with respect to the surface normal of the crystal. This angle should simply be chosen so that $\mathbf{d}_{\text{eff}}$ is maximized. For the *Type I* interaction used here, the optimum angle is 90° [25]. The effective nonlinear coefficient $\mathbf{d}_{\text{eff}}$ corresponds to $\chi^{(2)}/2$ in $\mathbf{P}_{\text{NL}} = \epsilon_0\chi^{(2)}\mathbf{E}^2$ (equation (29)), where $\chi^{(2)}$ indicates the strength of the second order interaction. However, as previously mentioned, in an anisotropic medium $\chi^{(2)}$ is a tensor, since each component of the polarization vector $\mathbf{P}$ depends on the components of the electric field vector $\mathbf{E}$. An effective value $\mathbf{d}_{\text{eff}}$ of $\chi^{(2)}/2$ can then be found which depends on the direction of the electric fields [15].

Apart from the angles θ and α the length L of the crystal must also be decided. There are two important measures: Coherence length and pulse splitting length. The coherence length L_c is the length at which the phase difference between two interacting waves has become π. It is given by [15]

$$L_c = \frac{2\pi}{|\Delta\mathbf{k}|}. \tag{63}$$

L_c is a measure of how far into the crystal the nonlinear process is efficient [15]. If the crystal is longer than L_c the generated waves will start to interfere destructively and the gain will actually be reduced. Furthermore, sum-frequency generation may also occur between the signal and the idler, resulting at radiation at the pump frequency. This will also reduce the gain.

The pulse splitting length [25] is a result of the difference in group velocities of the signal, idler and pump. In order for the nonlinear process to take place, the signal and the idler must overlap with the pump not only spatially, but also temporally. Because they have different group velocities they will, however, separate after a certain distance, and the amplification will cease. The pulse splitting length is given by [25]

$$l_{j3} = |\tau/(1/v_{gj} - 1/v_{g3})|, \tag{64}$$

where τ is the FWHM length of the pump and j=1,2. Note that it is very important for the amplification process that the idler does not separate from the pump. The reason for this is that the idler, with an angular frequency of ω_2, will also be amplified. That is, the beam with a frequency of ω_2 will now act as the signal. Amplification of this beam will, just as before, result in an idler, but this time at ω_1. This is in fact the same frequency as the initial signal, which shows that the amplification of the idler at ω_2 will provide positive feedback and add to the signal [25].

Because a birefringent crystal is used as a nonlinear medium, the extraordinary wave will be refracted even at normal incidence. In this case (*ooe*), the pump beam will be refracted, as shown in figure 28. Before the pump enters the crystal, the Poynting vector $\mathbf{S}$ and the wavevector $\mathbf{k}$ are parallel. Upon entering the birefringent crystal the Poynting vector $\mathbf{S}$ will change direction, but the wavevector $\mathbf{k}$ will be unaffected. According to reference [25], the walkoff angle is given by

$$\rho(\theta) = \arctan((n_o/n_e)^2 \tan(\theta)) - \theta, \tag{65}$$

when $n_o > n_e$, as is the case for example in BBO.

Since the phase-matching angle is the angle between the optic axis and the wavevector, not the Poynting vector, the walkoff angle does not affect the phase matching angle. The walkoff is still an issue, however, since the pump and signal beam must overlap spatially to be able to exchange energy. To minimize the effect of angular walkoff, the crystal should be rotated so that the signal beam and the pump beam both are refracted to the same side of the normal (so if the beam in figure 28 is the pump beam, the signal beam should be refracted to the right and therefore enter the crystal from the left). This will minimize the angle between the pump and the signal beam.

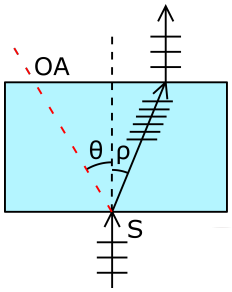

Figure 28: Refraction of the extraordinary beam in a birefringent material. The beam is refracted but the wavefronts will still have the same direction. OA - optic axis, S - Poynting vector

5.2 Simulation of NOPA

Suitable values of θ and α can be found from figure 27. The desired wavelength range is 620 - 750 nm. As the phase matching curves show, it is not possible to find a curve that is flat enough over that range. The range 640 - 750 nm, however, looks promising. To determine the optimal curve, the wave vector mismatch Δk was numerically integrated over the desired wavelength range. This was done by summing Δk for 500 wavelength points between 640 - 750 nm, for different choices of α and θ. The result is denoted $\Sigma|\Delta k|$. The combination of α and θ that gives the smallest $\Sigma|\Delta k|$ over the desired wavelength range should therefore give a good starting point for finding the optimal phase-matching and non-collinear angle. The result is shown in figure 29.

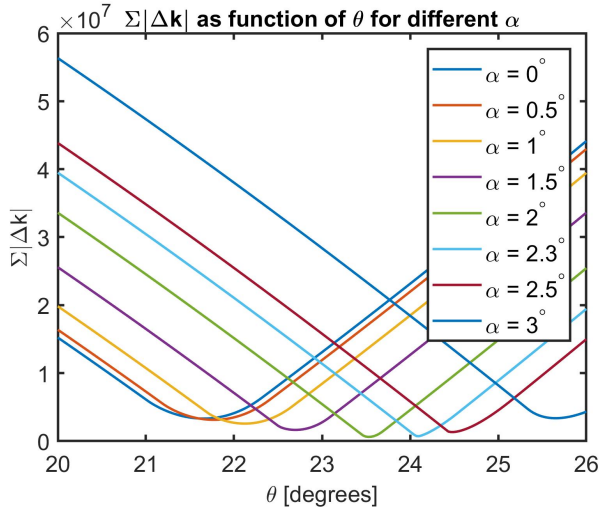

Figure 29: The result of integrating the wave vector mismatch for 500 wavelength points between 640 - 750 nm. The combination of θ and α that minimizes this should give a good starting point for finding the optimal values.

The figure shows that $\Sigma|\Delta k|$ is minimized for $\alpha = 2°$ and $\theta = 23.53°$. This was rounded to $\theta = 23.6°$. Note that the value of α is the internal angle. Because the signal will be refracted as it

enters the crystal, the external angle needs to be larger than α.

The intensity of the pump I_3 and the length of the crystal L is also needed to calculate the gain. The power of the pump light was measured to be approximately $P_{avg} = 2.7$ W. Following the same procedure as for the intensity calculation for the white light gives a peak power of $P_{peak} = 34$ MW, once again assuming a 400 fs pulse duration. The beam diameter of the green light at the focus, at which the BBO crystal was to be placed, was measured with a beam profiler, and found to be approximately 200 µm. This gives according to equation (54) an area of $1.57 \cdot 10^{-8}$ m^2, and using equation (55), this results in the intensity 210 GW/cm^2. In reference [25], it is mentioned that typical intensities for the pump are 100 - 150 GW/cm^2 in BBO. The intensity may therefore be too high. However, the pulse length is only roughly approximated from the autocorrelation trace (figure 12) and also the pulse structure is not known. This means that the calculated peak intensity possibly is slightly inaccurate and the actual intensity at the focus will be lower.

The thickness of the crystal was determined by plotting the coherence length and the pulse splitting length. The coherence length is shown in figure 30 a).

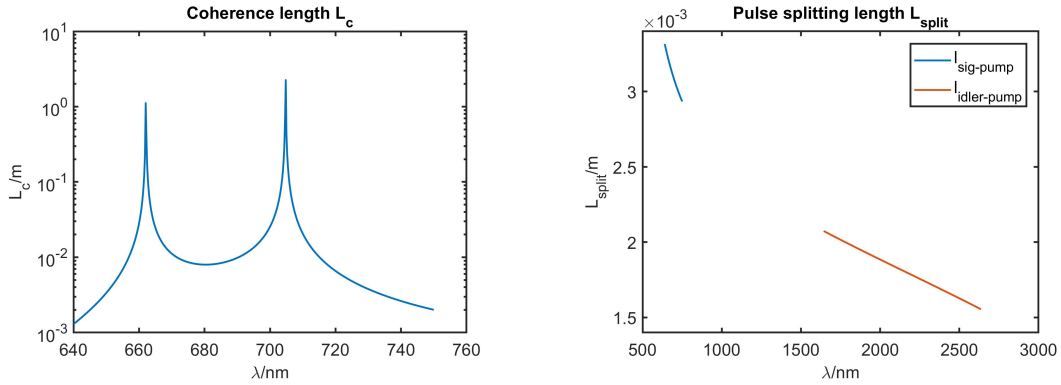

(a) Coherence length

(b) Pulse splitting length

Figure 30: Coherence and pulse splitting length in BBO for $\theta = 23.6°$.

The two peaks in the figure show that perfect phase matching is achieved for two wavelengths (664 and 705 nm). The coherence length then drops very rapidly when moving away from these wavelengths. The coherence length, however, is greater than 1.5 mm over the entire range, which means that a 1.5-mm-thick crystal is within the limits of acceptable length.

The pulse splitting length is shown in figure 30 b) for both the signal and the idler. Both of these are greater than 1.5 mm as well, but it is interesting to note that the length is actually limited by the idler. If the length is longer than the pulse splitting length of the idler, there would still be amplification (if the coherence length is long enough), but it would be much lower since the positive feedback from the idler is lost. The conclusion is that the maximum length of the crystal is 1.5 mm. However, from figure 30 a) it is noted that this is very close to the coherence length around 640 nm. For this reason, a 1-mm-thick crystal will be chosen for the simulations.

Now, the gain can be calculated. The length is $L = 1$ mm and the pump intensity is assumed to be 150 GW/cm^2 (since 210 GW/cm^2 as previously calculated is too much). Three different θ are investigated: $\theta = 23.6°$, $\theta = 23°$ and $\theta = 24°$. The first angle gives the smallest $\Sigma|\Delta k|$, and the two other ones are chosen to investigate the effect of choosing slightly smaller and larger angles. For each θ, four different gain curves, corresponding to 4 different non-collinear angles α, are plotted. The result is shown in figures 31 - 33.

All these curves are very similar in the wavelength region of interest. It can be noted that for larger angles θ, the bandwidth increases, but the spectrum shifts towards longer wavelengths. Judging from these graphs, $\theta = 23°$ would be the optimal choice, since it has sufficient bandwidth but covers shorter wavelengths better. What is striking, however, is the gain. For all gain curves the simulated gain is around 10^4. This is a very high and more than what can be expected from the implementation. Therefore, a lower intensity is chosen in order to obtain a more realistic simulation. Figure 34 - 36 shows the gain using a reduced intensity of 50 GW/cm^2

The gain curves now have a significantly different shape, and furthermore, the gain is reduced by two orders of magnitude. This is quite remarkable, since the intensity was only reduced by a factor of three. Just as for the higher intensity, it can be seen that choosing a larger θ will give

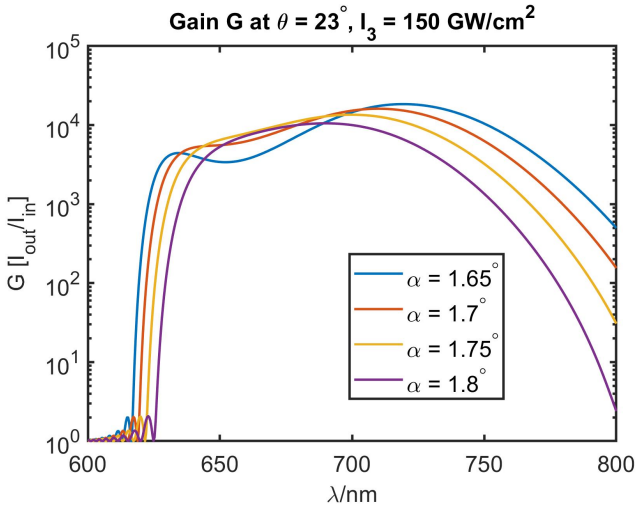

Figure 31: Gain curves for $\theta = 23°$, $L = 1$ mm and pump power 150 GW/cm^2.

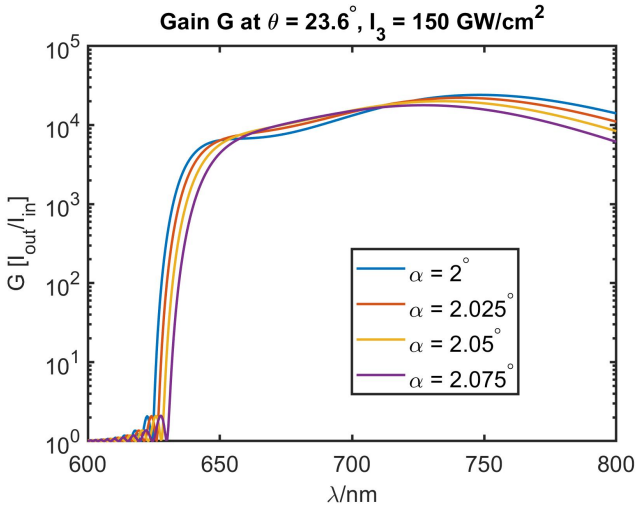

Figure 32: Gain curves for $\theta = 23.6°$, $L = 1$ mm and pump power 150 GW/cm^2.

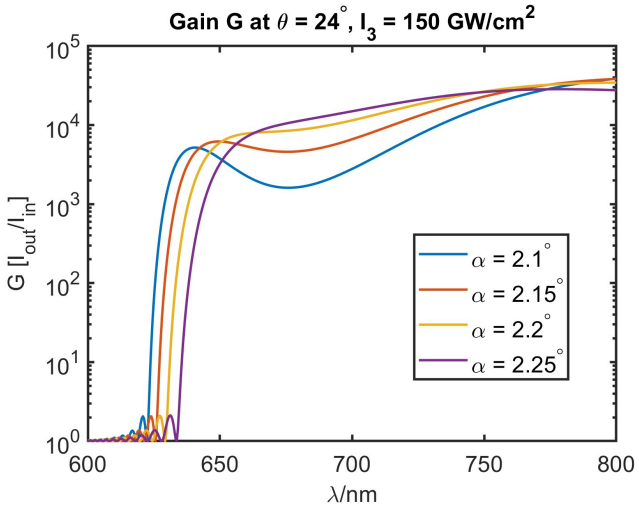

Figure 33: Gain curves for $\theta = 24°$, $L = 1$ mm and pump power 150 GW/cm^2.

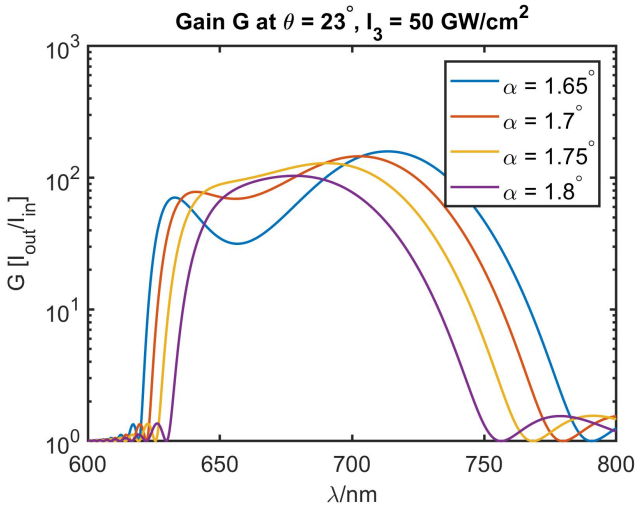

Figure 34: Gain curves for $\theta = 23°$, $L = 1$ mm and pump power 50 GW/cm^2.

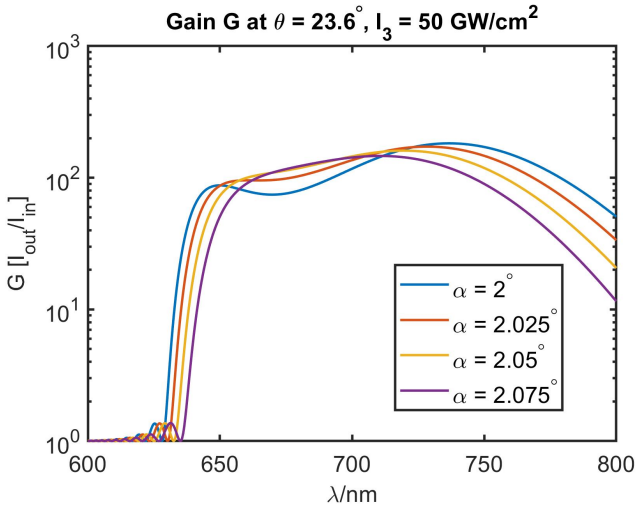

Figure 35: Gain curves for $\theta = 23.6°$, $L = 1$ mm and pump power 50 GW/cm^2.

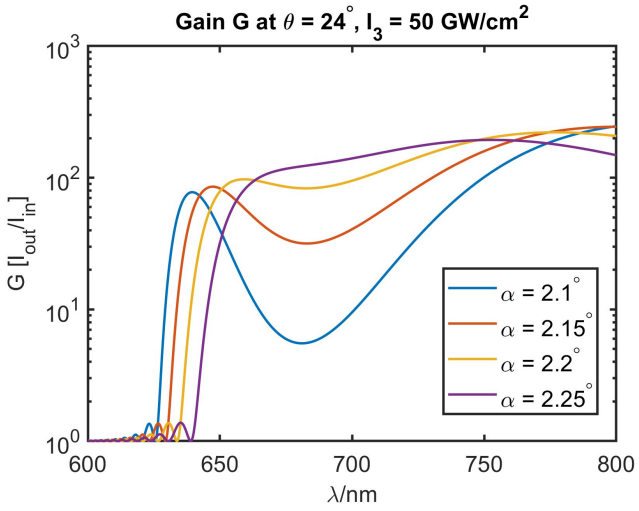

Figure 36: Gain curves for $\theta = 24°$, $L = 1$ mm and pump power 50 GW/cm^2.

more gain towards longer wavelengths and a wider bandwidth as well. This is consistent with figure 27. The phase-matching curves that corresponds to a smaller θ are flatter towards shorter wavelengths, but the overall bandwidth is reduced. Increasing θ gives a longer flat range, but it is located towards longer wavelengths. The simulated gain is now closer to what can be expected, it is somewhere around 100 - 200 over most of the desired range. But do note that, as previously mentioned, pump depletion and other effects are ignored when plotting these curves. The actual gain may therefore be substantially smaller and subsequently, a pump intensity of 150 GW/cm^2 would not be unreasonable to use.

For the simulations at 50 GW/cm^2, the curves at $\theta = 23.6°$ are indeed the best for this application, as predicted. At $\theta = 23°$ the gain does not cover the longer wavelengths as well as at $\theta = 23.6°$, and at $\theta = 24°$ the shorter wavelengths are not covered as well or the gain profile has a dip in the middle. However, there is not much difference between the curves at $\theta = 23.6°$ and $\theta = 24°$ in the wavelength region of interest, so both choices would likely work for this application. The optimal α at $\theta = 23.6°$ can be found from figure 35 to be $\alpha = 2.05°$. For this angle, the simulation shows that the gain is fairly flat over most of the desired range and the bandwidth is reasonably wide. As figure 35 shows, improving the bandwidth gives a less flat gain curve and vice versa. The optimal trade-off is therefore at $\alpha = 2.05°$. This is the internal angle. The external angle α_{ext} can be calculated with Snell's law, $n_1 \sin \alpha_{ext} = n_2 \sin \alpha$ [15]. The crystal is in air so n_1 can be approximated as 1, while $n_2 \approx 1.67$ over the desired wavelength range (see figure 47 in appendix 1). This gives the external angle $\alpha_{ext} = \arcsin(1.67 \sin 2.05°) = 3.42°$

The implementation of a NOPA has been shown in previous publications, for example by reference [17], on which the envisioned SWIR source described in this thesis is based upon. In that case, a 4-mm-thick BBO crystal was used with a phase-matching angle of $\theta = 23.3°$ and non-collinear angle of $\alpha = 1.8°$. This is quite close to the findings from the simulations in this section.

Figure 37 shows the walkoff angle ρ due to the extraordinary refraction, as function of the phase matching angle θ. The walkoff angle is quite small (around 3.27° at $\theta = 23.6°$) and quite close to the noncollinear angle, so it is possible to compensate for some off the walkoff by proper alignment of the nonlinear crystal.

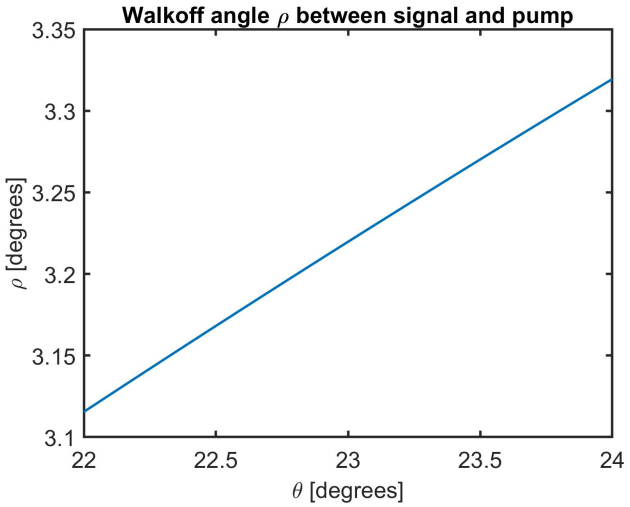

Figure 37: Walkoff angle as function of the phase matching angle θ.

It can be shown [15] that the efficiency of the NOPA process is given by

$$I \propto \text{sinc}^2(\frac{\Delta \mathbf{k}}{2\pi}), \tag{66}$$

where $\text{sinc}(x) = \frac{\sin(\pi x)}{\pi x}$. Equation (66) is plotted in figure 38 with the optimal parameters $\theta = 23.6°$ and $\alpha = 2.05°$, for a 1 mm thick crystal. This shows the efficiency of the NOPA as a function of wavelength. Perfect phase-matching is achieved at two wavelengths, neither of which is the central wavelength. To obtain a large bandwidth, the phase-matching angle θ should therefore be chosen somewhere in the middle of the range of angles for the desired bandwidth. Figure 38

shows that the efficiency decreases particularly rapidly at shorter wavelengths (at 640 nm it is < 0.1).

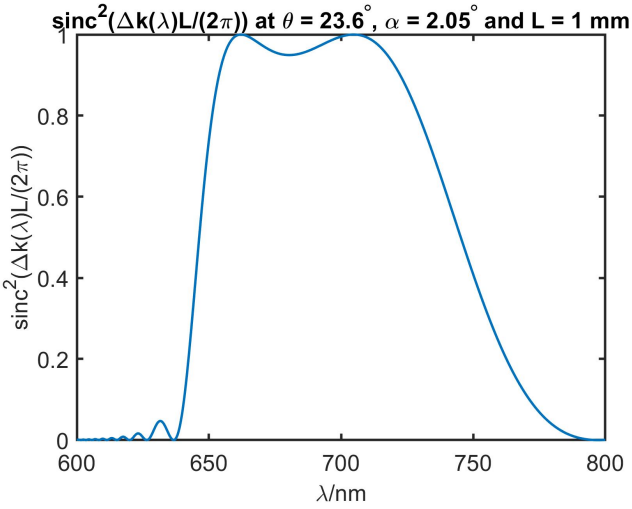

Figure 38: Efficiency of the NOPA with a 1 mm long BBO crystal.

5.3 NOPA results

The NOPA was first tested with a 1-mm-thick BBO crystal with $\theta = 23.6°$, which should be the optimal choice according to the simulations. A phenomenon called parametric fluorescence can be used to set up the NOPA. Parametric fluorescence is caused by fluctuations in the electric field (noise) that enters the crystal. These fluctuations are amplified and appear in the directions where phase matching is obtained [4]. The fluorescence takes the form of a circular structure in the far field. This is useful when aligning the NOPA. When the fluorescence is observed, it means that the crystal is oriented in a correct way to be phase matched for the nonlinear interaction. There will also be a spot in the ring in the far field which shows where to aim the seed pulse, i.e. it shows the approximate noncollinear angle. However, the fluorescence could not be observed with the 1-mm-thick crystal. This is probably a sign of low intensity. Note that when the intensity of the pump beam was estimated previously, a value of 210 GW/cm^2 was obtained, assuming 400 fs pulse duration. The actual intensity of the pump beam is therefore probably lower than this, which means that either the approximated pulse duration is inaccurate, or that the pulse indeed consists of several pulses, as was suggested before.

The 1 mm thick crystal was replaced with a thicker, 3-mm-thick BBO crystal with $\theta = 23.4°$. This phase matching angle is not optimal, but it should only be a small difference. With this thicker crystal, the parametric fluorescence could be observed. This was used to align the crystal, and amplification of the supercontinuum could be achieved.

The spectrum of the amplified light was measured using 2.5 and 3 W of pump power. The result is shown in figure 39. The spectrum using 2.5 W of pump power is quite wide, but also spikey and has a low power. This structure will translate into the time domain as well. The spectrum using 3 W of pump power is on the other hand narrower, but has a decent power and is overall more well-behaved. The difference between the two spectra in figure 39 may be caused by a change in temporal overlap when the pump power is changed. The bandwidth of the spectrum obtained with 3 W of pump power is around 640 - 695 nm (FWHM), which is narrower than what is desired (including the shoulders as well gives a bandwidth between 630 - 720 nm). The main reason for this is that the supercontinuum has a significant chirp, due to dispersion in the YAG crystal, as well as the various nonlinear processes that generate the supercontinuum, such as self-phase modulation. The output spectrum of the NOPA will then depend on which part of the supercontinuum-pulse overlaps with the pump pulse in the NOPA crystal, since the frequency components of the supercontinuum will be temporally distributed over the pulse. Indeed, varying the temporal overlap (using the delay stage) made it possible to alter the spectrum, depending on which frequencies of the supercontinuum that the pump pulse overlapped with. In order to improve the bandwidth, the supercontinuum pulses must therefore be compressed. This will lead to shorter

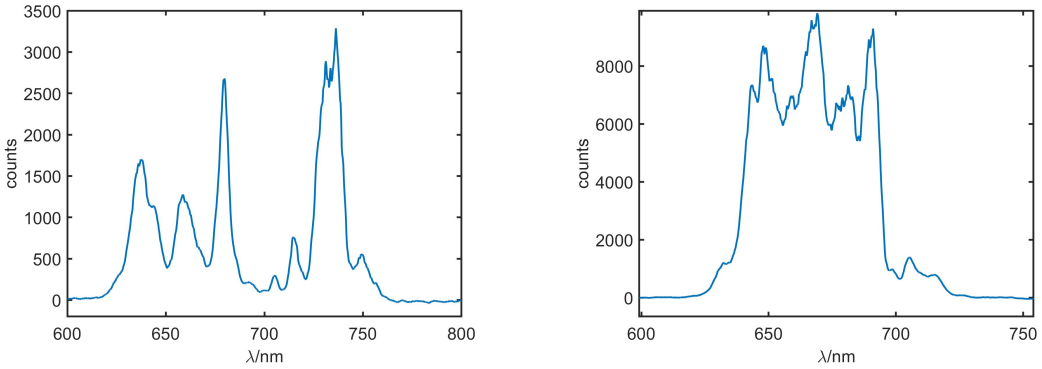

(a) 2.5 W (b) 3 W

Figure 39: Amplified supercontinuum using 2.5 W and 3 W of pump power.

pulses, which will result in better overlap with the pump pulses and therefore amplification of a larger part of the supercontinuum spectrum.

To a lesser degree, the thicker crystal also makes the spectrum narrower. Equation (72) shows that the efficiency drops faster with $\Delta\mathbf{k}$ when L is larger, leading to a narrower efficiency curve in figure 38. The use of a thinner crystal may therefore also increase the bandwidth slightly.

The power of the supercontinuum was approximately 5-6 mW before amplification, and after amplification 440 mW, using 3 W of pump power. At 2.5 W pump power, the power of the amplified supercontinuum was 130 mW, which is much less than what was achieved with the higher pump power. This is consistent with what the gain curves in figures 31 - 36 predicts, where a smaller reduction in pump power gave a much larger reduction in gain.

If the gain of the NOPA is defined as G_{tot} = (total output power)/(total input power), the gain using 3 W of pump power will be G_{tot} = 440 mW / 5.5 mW = 80. However, only a small part of the total supercontinuum power is amplified. Therefore, the gain G, as was simulated before, will be larger than 80. It is however not possible to estimate how much spectral power that is contained between 640 - 695 nm from the supercontinuum spectrum in figure 23, so the gain G can not be calculated.

It was previously touched upon that the simulated gain does not take into account pump depletion. A simple estimation of the depletion can be made by noting that with 3 W of pump power, 440 mW of output power was obtained. Since only a small part of the 5 - 6 mW of supercontinuum was amplified, one can assume that about 440 mW of pump power has been used to amplify the signal (assuming that, for example, absorption can be neglected). However, for each generated signal photon, one pump photon is required. Since the pump photons are more energetic than the signal photons, the total pump power used will be higher than the power of the amplified signal (the remaining energy is lost to the idler). The energy of a photon is given by $E = \hbar\omega$ [15], and therefore depends on the frequency. The frequency of the idler is $5.82 \cdot 10^{14}$ Hz, while the frequency of the signal (between 640-695 nm) is $4.32 \cdot 10^{14} - 4.69 \cdot 10^{14}$ Hz. The pump photons therefore have about 1.3 times the energy of the signal photons, which means that the total pump power that has been used for the amplification process is 440 mW $\cdot$ 1.3 = 570 mW. The pump power would therefore have dropped to 3 - 0.57 W = 2.43 W. This is approximately a 19 % drop in power. Although this will reduce the gain, the pump is most certainly not depleted. In this simple approximation, any temporal stretching of the pump is neglected. Temporal effects will lead to a further drop in power, however, this is more difficult to approximate.

5.4 Overview of the complete setup

The amplification of the generated supercontinuum was achieved using a NOPA geometry. It was possible to generate a sufficiently flat and stable supercontinuum between 620 - 750 nm, as desired. The NOPA had a satisfying gain, however the resulting bandwidth between 640 - 695 nm is narrower than what is expected. However, the bandwidth can be further improved by adding compression to the supercontinuum.

The entire setup is shown in figure 40. The wide black/grey beam coming out of the NOPA is the idler, which is angularly dispersed and not used.

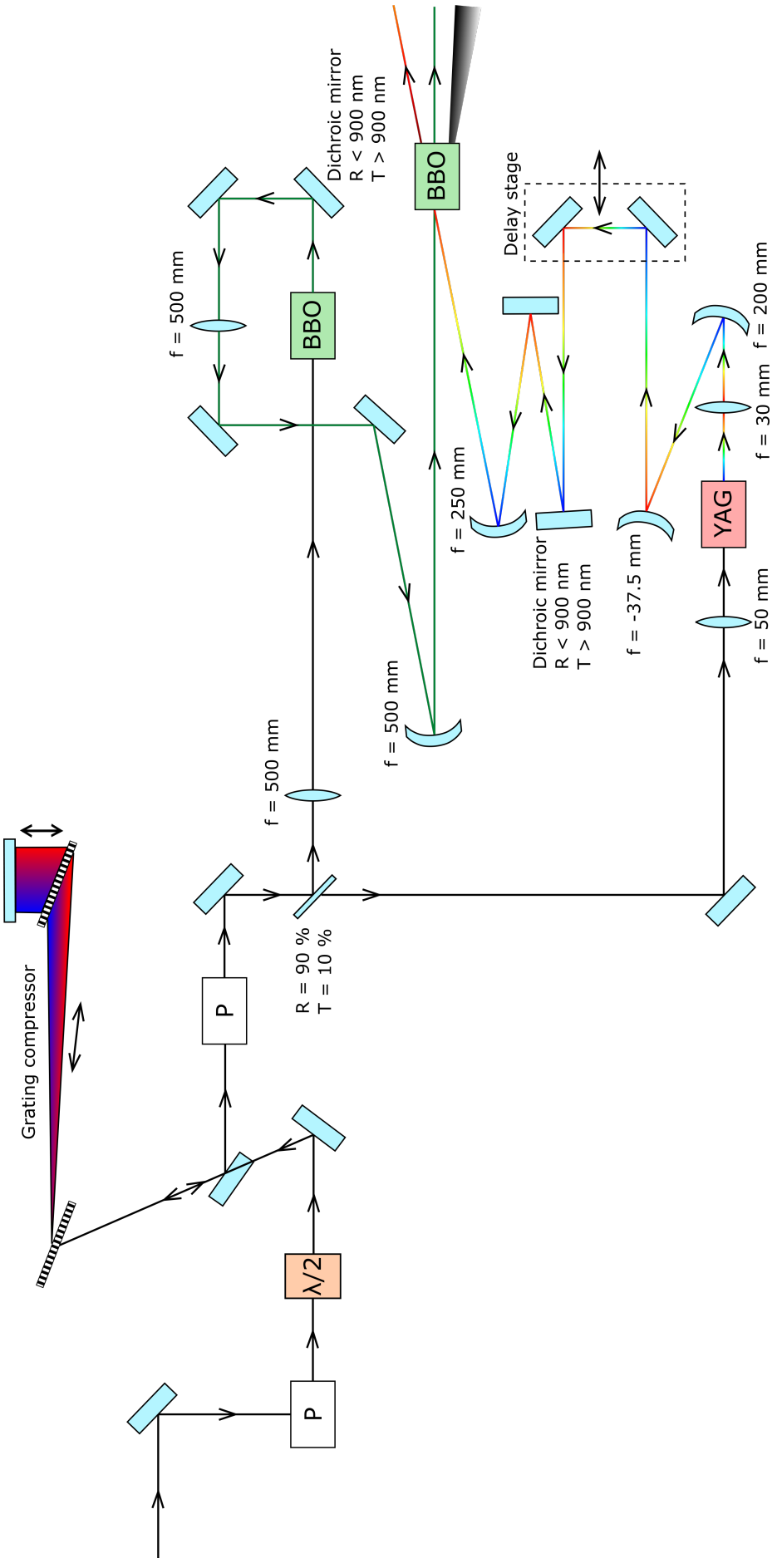

Figure 40: The complete setup

6 Reflection and outlook

This section will begin with a short reflection on the work that was done during this thesis. After this, it will be shown how the output from the NOPA can be used in a setup that produces CEP-stable SWIR pulses. For this, CEP-stabilization is first covered, and then how this can be implemented in the final setup, along with some simulations of the gain and bandwidth of the final setup. Lastly, some possible applications are presented.

6.1 Reflection on my work

During my time working on this thesis, I have performed both theoretical and practical work. First of all, I have learned a huge amount about ultrafast and nonlinear optics: How dispersion affects an optical system and how this can be compensated for with pulse compression, how nonlinear processes can be used to both generate light at a new frequency, as well as amplify already existing light, etc. I have followed the alignment procedure of a grating compressor, as well as taken measurements. The autocorrelation traces obtained during the alignment procedure were evaluated and I estimated the pulse duration from this. I have learned about the theory of second-harmonic generation, supercontinuum generation and the NOPA. I have used this to perform various simulations to determine e.g. suitable phase-matching angles and thicknesses, and also damage estimations. This was applied in the lab, where I, under supervision of my supervisors, built smaller test-setups to evaluate my theoretical findings. This also allowed me to get hands-on experience with a high-power laser system. I have learnt how to plan a setup as well as practical aspects, such as mounting and aligning optics. Measurements have been made in the lab, which were then evaluated and compared to the findings from the simulations. I have also made simulations of the remaining parts that are required to finalize the SWIR setup, in order to estimate the final performance of the system (which will be presented later in this section). Finally, I have also studied some possible applications of the envisioned SWIR source, such as solitons, high-harmonic generation and pump-probe spectroscopy (which will be covered in the last part of this section).

6.2 Stabilization of CEP

The carrier envelope phase was already briefly discussed in the introduction. It will be discussed in more detail here.

The SWIR source is intended to be a high-intensity, few-cycle source that can be used for strong-field light-matter interaction experiments like high-harmonic generation. For such interactions, which utilize the electric field of a light pulse, the carrier-envelope phase plays a fundamental role influencing the outcome of experiments. Consequently, a phase-stabilization scheme has to be implemented. This is done intrinsically by the DFG process itself. As it turns out, not only the frequencies of the participating waves in a nonlinear optical process are tied to one another, but also their phases [13].

For DFG, where $\omega_3 = \omega_1 - \omega_2$, the CEP of the resulting pulse is given by [13]

$$\phi_{\mathrm{CEP3}} = \phi_{\mathrm{CEP1}} - \phi_{\mathrm{CEP2}} - \pi/2. \tag{67}$$

Equation (67) is the basis for the passive CEP stabilization. Consider two pulses at ω_1 and ω_2 that are phase-locked, i.e. two pulses that originates from the same source. The CEP of the pulse at ω_1 is denoted ϕ and the CEP of the pulse at ω_2 is denoted $\phi + \phi_0$, where ϕ_0 is a constant. Due to propagation the CEP of the pulses will also change by constants c_1 and c_2, respectively. In total, the CEP of the pulses is $\phi_{\mathrm{CEP1}} = \phi + c_1$ and $\phi_{\mathrm{CEP2}} = \phi + \phi_0 + c_2$. Equation (67) will then give $\phi_{\mathrm{CEP3}} = \phi + c_1 - \phi - \phi_0 - c_2 - \pi/2 = c_1 - \phi_0 - c_2 - \pi/2$, which is constant. This means that a CEP-stable output can be obtained from the DFG process, even if ϕ drifts from shot to shot, as long as both input pulses have the same drift [13]. Even though this creates a passively stabilized source, the constants c_1 and c_2 might vary from shot to shot if the environment is not controlled sufficiently well (fluctuations in the setup, long distances etc.). On the other hand, c_1 and c_2 also provide means to control the CEP of the SWIR source. This can be done by simply changing one path length slightly, since this will change the value of c_1 or c_2 and therefore also the CEP. This is not really easily done with active stabilization (where dispersive elements like insertion of a wedge pair are usually used).

For four-wave mixing, where $\omega_4 = \omega_1 - \omega_2 + \omega_3$, the CEP is given by [13]

$$\phi_{\mathrm{CEP4}} = \phi_{\mathrm{CEP1}} - \phi_{\mathrm{CEP2}} + \phi_{\mathrm{CEP3}} - \pi/2. \tag{68}$$

Equation (68) is of particular interest for the supercontinuum generation. The main reason for the spectral broadening is SPM, which can actually be thought of as an four-wave mixing process between three frequencies ω_1, ω_2 and ω_3, all belonging to the spectrum of the pulse. These frequencies will create a new frequency, which can even lie outside the fundamental spectrum. The newly created frequency will in turn create even more new frequencies and so on, subsequently broadening the spectrum. Since all the initial frequencies belong to the same pulse, they will also have the same CEP ϕ. According to equation (68) the resulting CEP will therefore be $\phi_{\mathrm{CEP4}} = \phi - \phi + \phi - \pi/2 = \phi - \pi/2$. This shows the very important property of the supercontinuum, that the supercontinuum will be phase-locked to the input pulse [13].

The CEP stability of the DFG process and the preserved CEP in the supercontinuum can then be utilized to obtain a CEP-controlled output of the SWIR source.

6.3 The planned setup

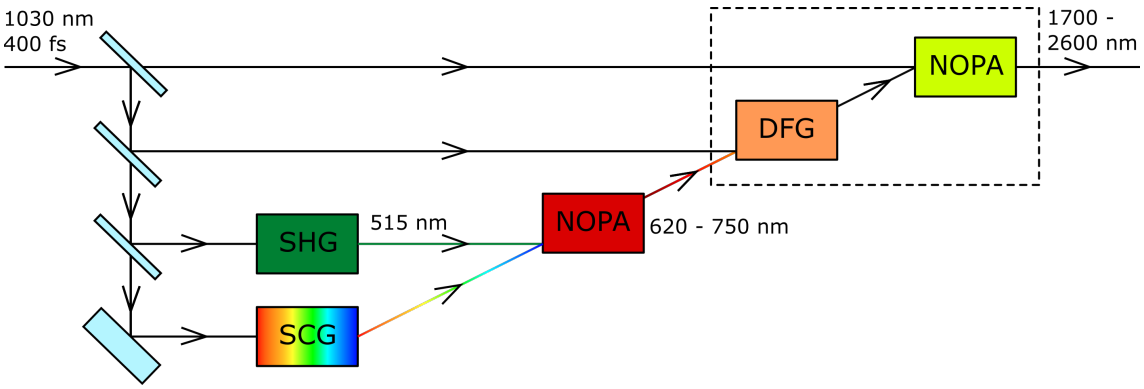

Figure 41: Block diagram of the final setup. The remaining stages are highlighted by the dotted box

The final setup of the SWIR source is shown in figure 41, highlighting the remaining parts by the dotted box. What remains is to do the DFG between the amplified supercontinuum and the 1030-nm light and then to amplify the resulting light. It is planned to use BBO for both the DFG and the amplification. The DFG between the desired 620 - 750 nm supercontinuum light and the 1030-nm light will result in a maximum spectrum between 1558 - 2628 nm, assuming the entire spectrum can be converted. The phase matching curves for the DFG are shown in figure 42 (a). Just as for the NOPA, a non-collinear setup gives flatter phase matching curves and therefore a wider bandwidth. However, a non-collinear geometry will also introduce an angular chirp. To avoid this, a collinear geometry ($\alpha = 0°$) is chosen. To obtain the widest bandwidth, the phase matching angle θ should be chosen between the largest and smallest for the desired range. For the desired range (620 - 750 nm), this gives $\theta = 20.3°$ and for the range obtained from the NOPA (640 - 695 nm) $\theta = 20.2°$. Figure 42 (b) shows the coherence length for the DFG when $\theta = 20.3°$. As can be seen, the coherence length is at least 1 mm over the entire range between 620 - 750 nm. This is a reasonable value, which means that fairly efficient conversion can be obtained over the entire desired range. This also means that the spectrum from the NOPA can be optimized and extended towards longer wavelengths without being restricted by the DFG.

After creating the difference frequency, the radiation needs to be amplified to reach sufficient peak intensities to drive strong-field processes. This will be done in a second NOPA, using the light generated in the DFG as the signal and the 1030-nm light as the pump. In this case, the pump beam does not need to be frequency doubled since the 1030-nm light already has a shorter wavelength than the entire output from the DFG process. Figure 43 (a) shows the phase matching curves for the second NOPA.

In contrast to the first NOPA (figure 27), the phase matching curves are actually flatter for noncollinear geometries with small noncollinear angles. For small noncollinear angles the phase matching curves are also better centered at 2 µm. Therefore, the best choice here seems to be a very

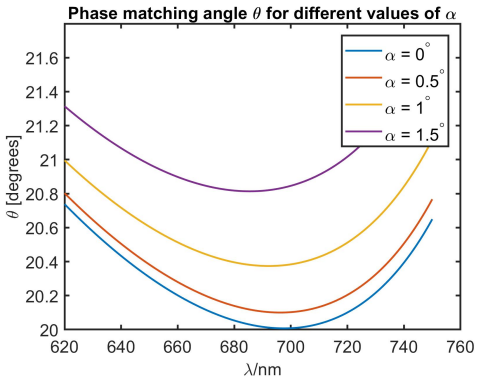

(a) Phase matching curves for the DFG in a BBO crystal

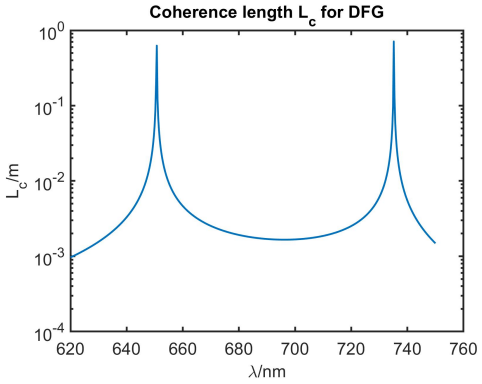

(b) Coherence length for the DFG for $\theta = 20.3°$.

Figure 42: Phasematching curves and coherence length for DFG in a BBO crystal between the amplified supercontinuum and the 1030-nm fundamental beam.

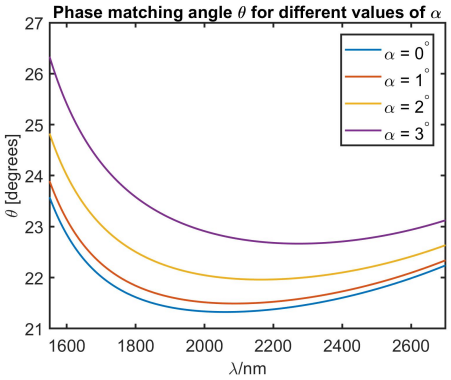

(a) Phase matching curves

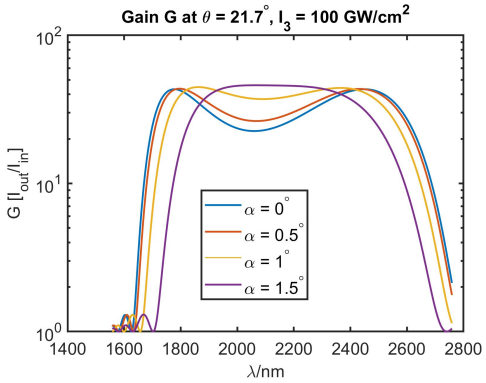

(b) Gain curves for $\theta = 21.7°$, $L = 1$ mm and pump power 100 GW/cm^2.

Figure 43: Phase matching and gain curves for the second NOPA with 1030-nm pump in a BBO crystal.

small noncollinear angle. A collinear configuration should be avoided in order to be able to separate the idler from the signal (the idler will be degenerate with the signal for some frequencies). Based on the curves, a choice of $\theta = 21.7°$ seems reasonable. Gain curves for this choice are shown in figure 43 (b), where the length of the crystal is 1 mm and the intensity of the pump beam is 100 GW/cm^2. A higher intensity is needed here compared to the first NOPA to obtain a similar amount of gain. As mentioned in the previous section, this is a usual intensity for nonlinear processes, so the BBO should be able to handle it. Also, remember that the actual gain of the implemented NOPA may be lower than what is predicted by figure 43 (b), due to the simplifying assumptions made (no pump depletion, no absorption, etc.). In this case the yellow curve, corresponding to $\alpha = 1°$, has the best profile. The gain curve stretches from 1700 - 2600 nm, which gives a bandwidth of 900 nm centered at 2150 nm. This is narrower than the maximum ideal bandwidth of the DFG (1558 - 2628 nm), which shows that the final bandwidth of the system is more likely to be limited by the second NOPA than the DFG.

The final pulse length can be estimated from the bandwidth of the output from the second NOPA (clearly some compression after the NOPA is needed to obtain the shortest pulse length). Currently the output from the first NOPA is between 640 - 695 nm, which gives 1690 - 2127 nm after the DFG. This gives a bandwidth of $\Delta\nu = 36.5$ THz. Using equation (4), this gives a pulse length of $\tau_{\mathrm{FWHM}} = 12.1$ fs. Note that the bandwidth in this case is not limited by the second NOPA. On the other hand, if the entire desired spectrum from the first NOPA can be obtained (620 - 750 nm), the bandwidth is limited by the second NOPA. This would give a bandwidth of 1700 - 2600 nm, which gives a pulse length of 7.20 fs. Light with a wavelength of 2 µm has a period time of 6.67 fs, so in either case the transform limited pulse duration is less than two optical cycles.

The output will also be CEP-stable because of the DFG. Both the supercontinuum and the 1030 nm light in the DFG process are taken from the same source and will therefore have the same CEP, except for a constant due to propagation. As previously shown, the DFG will produce a CEP-stable output, and the final NOPA will just like the first NOPA not affect the CEP.

6.4 Applications

6.4.1 Anomalous dispersion and optical solitons

In the visible region, most optical materials exhibit normal dispersion. In this case, longer wavelengths travels faster than shorter ones through the material. The group velocity dispersion is characterized by the dispersion coefficient D_λ, as given by equation (16). In the case of normal dispersion, the dispersion coefficient is negative. However, for longer wavelengths, such as what will be produced by the SWIR source, the dispersion is often anomalous. Figure 44 shows the refractive index of BK-7 glass. The dispersion coefficient D_λ depends on the second derivative of the refractive index, and is negative (normal dispersion) when the refractive index curve is convex. Figure 44 shows that BK-7 glass exhibits normal dispersion at short wavelengths. At 1322 nm, however, the curve has an inflexion point, where the dispersion coefficient changes sign. The dispersion is subsequently anomalous for long wavelengths. More specifically, it is anomalous at the wavelength of the SWIR-source.

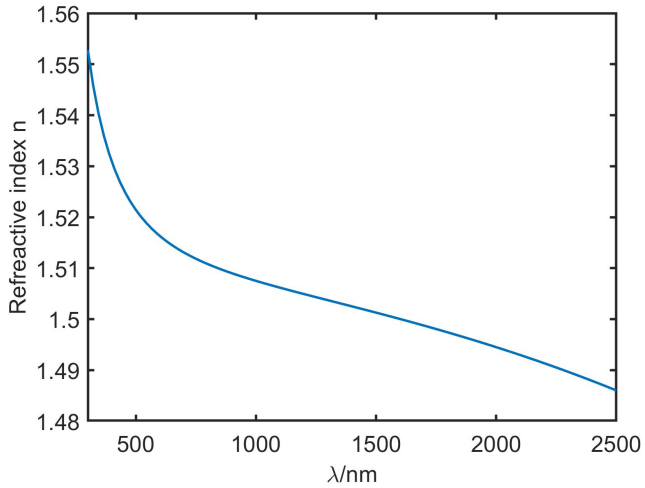

Figure 44: Refractive index of BK-7 glass (data from [26]). Below 1322 nm the dispersion is normal and above it is anomalous. At 1322 nm there is in fact no dispersion.

The anomalous dispersion can be utilized to create an optical soliton. An optical soliton is a laser pulse that travels throughout a material with an unchanged shape [15]. Normally a pulse is subject to group velocity dispersion, which will cause the pulse to be stretched out and chirped. In order to create a soliton, the dispersion is counteracted using SPM. As previously explained, the Kerr effect leads to an intensity dependent refractive index, $n(I) = n + n_2 I$. If n_2 is positive, which it usually is, equation (48) shows that SPM will result in a chirped pulse whose leading edge is red-shifted and trailing edge is blue-shifted. This will reduce the effect of the anomalous dispersion, since shorter wavelengths (which travels faster with anomalous dispersion) will now be at the trailing edge of the pulse. The dispersion will therefore move the trailing edge closer to the center of the pulse. The leading edge will on the other hand travel slower, so it is also moved closer to the center of the pulse. If the strength of the dispersion and the SPM is balanced properly, the pulse can travel through the material with an unaltered shape. A soliton is thus achieved. In order to obtain a soliton, the pulse shape must be correct. The simplest shape a soliton can have is an unchirped sech^2 [4]. The pulse energy must also be chosen correctly, since this will determine the strength of the SPM.

Naturally, if the dispersion and the SPM does not cancel each other, the duration of the pulse will change as it propagates through the material. This means that the pulse can either be stretched or compressed, depending on how the shape and energy of the pulse is chosen. This means that

with properly chosen parameters, the pulse can be made to self-compress.

6.4.2 High-harmonic generation

As already mentioned in the introduction, the SWIR source can be used for high-harmonic generation. This will create ultrashort, attosecond pulses, which, for example, can be used to study events with an extremly short time duration.

Due to the long wavelength of the SWIR source, the cutoff of the HHG spectrum can be extended into the XUV and possibly the soft X-rays as well. A particularly interesting wavelength region in biology and medicine is the water window. The water window is in the X-ray regime, and stretches between 284 - 543 eV (4.37 - 2.33 nm). In this region, carbon is highly absorptive, while water has a very high transmittance. This means that the water window is very useful for imaging biological samples (due to their carbon content) [28, 29]. Both synchrotrons and free-electron lasers can produce coherent radiation in the water window, but these are large and expensive facilities [28]. It would therefore be very useful, if a table-top setup using HHG can be utilized instead. Emission of soft X-ray radiation using HHG has in fact been demonstrated several times, such as in reference [28]. Here, a wavelength of 2.1 µm was used to obtain an HHG spectrum from neon, with a cutoff of almost 450 eV. This is very promising for our envisioned SWIR source, which could possibly lead to novel imaging possibilities in the water window.

Although HHG was first demonstrated in gases, it has recently been demonstrated in solids as well [6]. HHG in gases has the disadvantage of requiring large setups with high power lasers and vacuum chambers, and also the gas needs to be confined to the interaction volume. HHG in solids has the distinct advantage of the medium being a solid and will therefore stay where it is. Concerning the performance, the cutoff does not necessarily depend quadratically on the electric field like equation (1) predicts. It has been shown for HHG in ZnO that the cutoff in fact depends linearly on E [30].

One difficulty with HHG in solids is the low cutoff energy, due to absorption in the solid. For comparison, reference [31] used a 1053-nm laser to study HHG in noble gases. In neon the cutoff was at least at the 135th harmonic (160 eV). Also, as previously mentioned, a cutoff at 450 eV in neon with a 2.1 µm laser was achieved by reference [28]. Compared to this, HHG in fused silica gave a cutoff at only 25 eV using a 1700-nm laser [32].

HHG in solids could still be useful for studying material properties, such as charge densities. It may also be possible to image single atoms in the solid, which could be used to find vacancies and impurities in semiconductors. Furthermore, HHG depends on the structure of the material, which means that it could be possible to manufacture nanostructures that can control the properties of the generated light [6]. The SWIR source described in this thesis is well suited for studying HHG in solids, and could therefore open up for new, interesting possibilities to study this phenomena.

It is possible to use more than one optical field for HHG. In this case, several waves with different frequency can be added to the fundamental field. By varying some properties of these waves it is possible to control the properties of the light generated by HHG. For example, the fundamental field can be sent through a second-order nonlinear crystal, which will add a second-order harmonic component to the fundamental [33]. Normally, HHG produces light at each half cycle of the driving pulse. However, when the pulse is a superposition of different frequency components, the symmetry of the pulse is broken. This will result in emission of a pulse at only every other half cycle, that is, one photon for each cycle of the fundamental light. This was shown in for example [33]. There it was also shown that changing the relative phase between the fundamental and the second harmonic makes it possible to tune the shape of the spectrum as well as the maximum photon energy. Since it was previously shown that it is possible for the future SWIR-source to produce less-than-two-cycle pulses, a two-colour approach can be used to enhance the dominant field maximum even more, resulting in the emission of single pulses from the HHG.

6.4.3 Pump-probe spectroscopy and PEEM

Pump-probe spectroscopy utilizes the ultrashort pulses created by HHG to study phenomena with a very short time duration, such as atomic motions, which occur on the time scale of ps, and electronic processes in the order of as. In pump-probe spectroscopy two laser pulses are used to study a material. First a pump pulse initializes some dynamic, due to e.g. an excitation. A probe pulse is then utilized to study this dynamic, by taking a snapshot of the dynamic without altering it. If this procedure is repeated for different time delays between the probe and the pump, the

property of interest can be studied over time. However, it is important that the process under investigation is reversible and the initial conditions are the same from shot to shot.

Clearly, this is a very general description and there are many different ways the scheme can be realized, with respect to e.g. wavelength of the pulses. There are a multitude of dynamics that can be studied this way. Some examples are presented in the following:

Vibrational and orientational dynamics of water have been studied, using a mid-IR pump-probe scheme. For this, 250 fs laser pulses between 2.8 - 3.2 µm were used. An intense pump pulse excited the water molecules and a probe pulse was used to study the transmittance as a function of time [34].

A two-colour pump-probe scheme was used in reference [35], where ultrafast wavepacket dynamics in the dissociation of H_2 was studied. An XUV pump pulse was used to start the wavepacket dynamics and an IR probe pulse then made the H_2-molecules dissociate.

Reference [1] used a similar scheme, so the pump was in the XUV and the probe in the near-IR. Here, the time difference in photoemission of electrons in different states in tungsten was studied. The pump ionized the atoms directly and the probe then affected the momentum of the free electrons, leading to a streaked momentum distribution.

Naturally, it is necessary to have single pump and probe pulses. If one or both of these pulses are generated through HHG, the two-colour approach is very useful. This will ensure that a only a single pulse is created by HHG for each pulse of the driving field. Furthermore, the delay between the pulses must be controlled. This can be done with an interferometer setup, like the one shown in figure 9. One IR-pulse is split into two as it enters the interferometer. The HHG is performed in one of the arms, so that one of the pulses are at XUV. Both pulses are then overlapped at the output. This can be done e.g. with a mirror with a hole in the middle (due to the lack of beam splitters at XUV).

The pump-probe scheme can also be used for photoelectron emission microscopy (PEEM), as proposed in reference [36]. PEEM uses electrons emitted from the surface of a sample in order to study so-called plasmons. Plasmons are resonant field-driven oscillations of the elctron density. When an oscillating electric field is incident on a metal surface, plasmons can be created [8]. The proposed scheme first uses a pump-probe scheme to excite and probe the plasmons. PEEM is then used to study the plasmons. The pump pulse is in the near-IR and excites the surface plasmons. An attosecond XUV probe pulse is then used to photo-emit electrons. An ultrashort probe pulse is required to resolve the rapid dynamics of the plasmons. An attosecond pulse is short enough to make the emitted electrons escape from the material at a fraction of the driving field (which is in the near-IR). The energy of the electrons will therefore be a snapshot of the electric potential at the surface when they escape. The emitted electrons are subsequently imaged with a PEEM, which employs electron-guiding optics and an electron detector to image the electrons escaping the surface of the sample. The idea behind this scheme is that it can provide both a high spatial and temporal resolution. The use of an attosecond probe pulse provides a temporal resolution in the attosecond range. The imaging, on the other hand, is performed with electrons, which have a very short wavelength and can therefore provide a very high spatial resolution of 10 nm [37]. Attempts have been made to implement this scheme, [8, 38] for example, but it is challenging and the scheme proposed in [36], although being very attractive, is yet to be properly implemented. The SWIR source is however an attractive candidate for this. Due to its high repetition rate, space charge effects from too many electrons per laser shot can be avoided, boosting the resolution and reducing exposure time per picture.

References

[1] A. L. Cavalieri et. al. Attosecond Spectroscopy in Condensed Matter. *Nature*, 449:1029–1032, 2007.

[2] E. Goulielmakis et. al. Direct Measurement of Light Waves. *Science*, 305(5688):1267–1269, 2004.

[3] T. Gaumnitz et. al. Streaking of 43-attosecond Soft-X-ray Pulses Generated by a Passively CEP-Stable Mid-Infrared Driver. *Optics Express*, 25(22):27506–27518, 2017.

[4] R. Paschotta. *Encyclopedia of Laser Physics and Technology.* Wiley-VCH, 2008.

[5] D. Popmintchev et. al. Near- and Extended-Edge X-Ray-Absorption Fine-Structure Spectroscopy Using Ultrafast Coherent High-Order Harmonic Supercontinua. *Physical Review Letters*, 120(9):093002, 2018.

[6] S. Ghimire and D. A. Reis. High-Harmonic Generation from Solids. *Nature Physics*, 15:10–16, 2018.

[7] P. B. Corkum. Plasma Perspective on Strong-Field Multiphoton Ionization. *Physical Review Letters*, 71(13):1994–1997, 1993.

[8] C. Guo. *A High Repetition Rate Attosecond Light Source Based on Optical Parametric Amplification.* PhD thesis, Lund University, 2018.

[9] M. Lewenstein, Ph. Balcou, M. Yu. Ivanov, A. L'Huillier, and P. B. Corkum. Theory of High-Harmonic Generation by Low-Frequency Laser Fields. *Physical Review A*, 49(3):2117–2132, 1994.

[10] G. M. Archipovaite, S. Petit, J-C Delagnes, and E. Cormier. 100 kHz Yb-Fiber Laser Pumped 3 μm Optical Parametric Amplifier for Probing Solid-State Systems in the Strong Field Regime. *Optics Letters*, 42(5):891–894, 2017.

[11] A.D. Shiner et. al. Wavelength Scaling of High Harmonic Generation Ef[U+FB01]ciency. *Physical Review Letters*, 103(7), 2009.

[12] C. M. Heyl et. al. Scale-Invariant Nonlinear Optics in Gases. *Optica*, 3(1):75–81, 2016.

[13] G. Cerullo, A. Baltuška, O. D. Mücke, and C. Vozzi. Few-Optical-Cycle Light Pulses with Passive Carrier-Envelope Phase Stabilization. *Laser and Photonics Reviews*, 5(3):323–351, 2011.

[14] P. Rudawski et. al. Carrier-Envelope Phase Dependent High-Order Harmonic Generation with a High-Repetition Rate OPCPA-System. *The European Physical Journal D*, 69(70), 2015.

[15] B. E. A. Saleh and M. C. Teich. *Fundamentals of Photonics, 2nd edition.* Wiley, 2007.

[16] C. Lu. *Evaluation of White-Light Generation as Possible Seed for a Mid-Infrared Optical Parametric Chirped Pulse Amplifier.* Master thesis, 2016.

[17] M. Neuhaus et. al. 10 W CEP-Stable Few-Cycle Source at 2 µm with 100 kHz Repetition Rate. *Optics Express*, 26(13):16074–16085, 2018.

[18] E. B. Treacy. Optical Pulse Compression with Diffraction Gratings. *IEEE Journal of Quantum Electronics*, QE-5(9):454–458, 1969.

[19] R. Boyd. *Nonlinear Optics.* Academic Press, 3rd edition, 2008.

[20] D. A. Kleinman and R. C. Miller. Dependence of Second-Harmonic Generation on the Position of the Focus. *Phys. Rev.*, 148(1):302–312, 1966.

[21] A. Brodeur and S. L. Chin. Ultrafast White-Light Continuum Generation and Self-Focusing in Transparent Condensed Media. *Journal of the Optical Society of America B*, 16(4):637–650, 1999.

[22] S. Uhlig. *Self-Organized Surface Structures with Ultrafast White-Light*. Master thesis, 2015.

[23] M. Bradler and P. Baum and E. Riedle. Femtosecond Continuum Generation in Bulk Laser Host Materials with sub-µJ pulses. *Applied Physics B*, 97:561–574, 2009.

[24] S. Xu et. al. Femtosecond Laser Ablation of Crystals SiO_2 and YAG. *Optics Communications*, 274(1):163–166, 2007.

[25] C. Manzoni and G. Cerullo. Design Criteria for Ultrafast Optical Parametric Amplifiers. *Journal of Optics*, 18(10), 2016.

[26] Refractiveindex.info https://refractiveindex.info/?shelf=mainbook=y3al5o12page=zelmon, November 2018.

[27] E. Ingelstam, R. Rönngren, and S. Sjöberg. *TEFYMA*. Studentlitteratur, 3rd edition, 2014.

[28] G. J. Stein et. al. Water-Window Soft X-ray High-Harmonic Generation up to the Nitrogen K-edge Driven by a kHz, 2.1 µm OPCPA Source. *Journal of Physics B: Atomic, Molecular and Optical Physics*, 49(15), 2016.

[29] Ch. Spielmann et. al. Generation of Coherent X-rays in the Water Window Using 5-Femtosecond Laser Pulses. *Science*, 278(5338):661–664, 1997.

[30] S. Ghimire et. al. Observation of High-Order Harmonic Generation in a Bulk Crystal. *Nature Physics*, 7:138–141, 2011.

[31] A. L'Huillier and Ph. Balcou. High-Order Harmonic Generation in Rare Gases with a 1-ps 1053-nm Laser. *Physical Review Letters*, 70(6):774–777, 1993.

[32] Y. S. You et. al. High-Harmonic Generation in Amorphous Solids. *Nature Communications*, 8(724), 2017.

[33] E. Mansten et. al. Spectral Shaping of Attosecond Pulses Using Two-Colour Laser Fields. *New Journal of Physics*, 10, 2008.

[34] S. Woutersen, U. Emmerichs, and H. J. Bakker. Femtosecond Mid-IR Pump-Probe Spectroscopy of Liquid Water: Evidence for a Two-Component Structure. *Science*, 278(5338):658–660, 1997.

[35] F. Kelkensberg et. al. Molecular Dissociative Ionization and Wave-Packet Dynamics Studied Using Two-Color XUV and IR Pump-Probe Spectroscopy. *Physical Review Letters*, 103(12):658–660, 2009.

[36] M. I. Stockman, M. F. Kling, U. Kleineberg, and F. Krausz. Attosecond Nanoplasmonic-Field Microscope. *Nature Photonics*, 1:539–544, 2007.

[37] S. H. Chew et. al. Imaging Localized Surface Plasmons by Femtosecond to Attosecond Time-Resolved Photoelectron Emission Microscopy - "ATTO-PEEM". In *Attosecond Nanophysics: From Basic Science to Applications*. Wiley-VCH Verlag GmbH Co. KGaA., 2015.

[38] E. Mårsell. *Photoemission Electron Microscopy with an Attosecond Light Source*. Licenciate thesis, 2014.

Appendix 1

Calculation of phase-matching for SHG in BBO

For second-harmonic generation, equations (36) and (37) reduces to $\omega_3 = 2\omega_1$ and $\mathbf{k}_3 = 2\mathbf{k}_1$, respectively. In the experiments of this thesis, the wavelength corresponding to ω_1 is $\lambda_1 = 1030$ nm, which gives $\lambda_3 = 515$ nm according to the condition on the frequencies and equation (5). Since $\mathbf{k}_1$ and $\mathbf{k}_3$ must be parallel, the phase matching condition can be further reduced to $n(\lambda_3)/\lambda_3 = 2n(\lambda_1)/\lambda_1$. Here $\lambda_3 = \lambda_1/2$, which finally leads to the condition $n(\lambda_3) = n(\lambda_1)$. Because of dispersion it is not straightforward to satisfy this condition, however it is possible. The solution is to use an anisotropic material. In an anisotropic material, the refractive index depends on the direction of the electric field of the beam [15]. Here BBO (β-Barium borate) will be used, which is a common nonlinear crystal. It also exhibits uniaxial birefringence. Birefrigence is a special case of anisotropy, which is illustrated in figure 45.

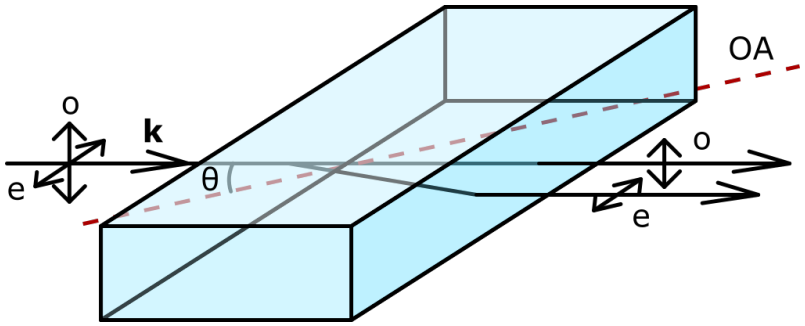

Figure 45: Birefringence in a crystal, OA - optic axis, o - ordinary polarized wave, e - extraordinary polarized wave, $\mathbf{k}$ - wavevector, θ - phase-matching angle. The ordinary polarized wave will experience refractive index n_o regardless of direction of $\mathbf{k}$. The refractive index for the extraordinary polarized wave will on the other hand depend on the angle θ between the wavevector and the optic axis, and take a value between n_o and n_e.

A birefrigent material has an optic axis and the orientation and polarization of the beam relative to this axis determines the refractive index [15]. If the polarization of the beam is perpendicular to the plane of the optic axis and the wavevector $\mathbf{k}$, the beam is called ordinary and the refractive index n_o (ordinary refractive index) is not dependent on the direction of the beam. This is the polarization marked as "o" in figure 45. The case when the polarization is in the same plane as the optic axis and the wavevector $\mathbf{k}$ is more interesting. The beam is now called extraordinary and has the polarization marked as "e" in figure 45. The refractive index of the extraordinary beam depends on the angle θ between the wavevector $\mathbf{k}$ and the optic axis. If $\mathbf{k}$ is parallel to the optic axis the refractive index will still be n_o, but if $\mathbf{k}$ is perpendicular to the optic axis it will instead experience the refractive index n_e (extraordinary refractive index). For any other angle the refractive index $n_e(\theta)$ will be somewhere in between n_o and n_e, as expressed by [15]

$$\frac{1}{n_e(\theta)^2} = \frac{\cos^2\theta}{n_o^2} + \frac{\sin^2\theta}{n_e^2}. \tag{69}$$

A peculiarity of birefringent materials is that the extraordinary beam will be refracted even at normal incidence [15]. This is shown in figure 45, where the extraordinary beam is refracted, whereas the ordinary beam is not. However, it is only the Poynting vector $\mathbf{S}$, which represents the power flow, that changes direction. The wavevector $\mathbf{k}$ of the extraordinary beam will not change direction and will in fact point in the same direction as it does for the ordinary beam [15]. The angle θ is the angle between $\mathbf{k}$ and the optic axis, so the extraordinary refraction can be ignored when doing the phase matching. That is, the extraordinary beam should be treated as if it is still at normal incidence when inside the crystal (since the wavevector still is at normal incidence). However, since the extraordinary beam will walk off relative to the ordinary beam, the interaction between the beams will be smaller as the extraordinary beam walks off.

Equation (69) represents the refractive index as an ellipsoid. The refractive index is the distance to the point at which $\mathbf{k}$ intersects this ellipse. This is shown in figure 46.

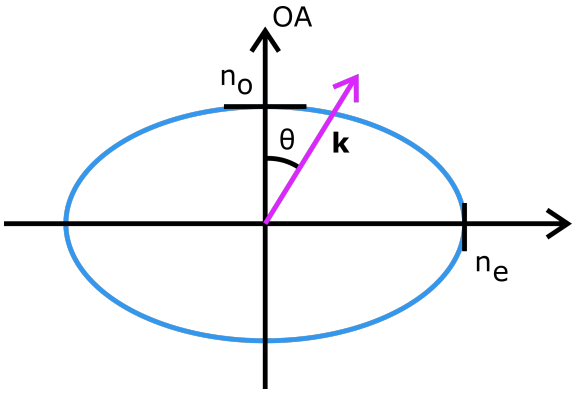

Figure 46: The elliptical curve (blue) satisfies equation (69). The refractive index for an extraordinarily polarized beam can be found by the intersection of its k-vector with the curve.

The refractive indexes n_o and n_e can be calculated using the Sellmeier equation, which approximate the wavelength dependent refractive index with a sum. For BBO, n_o and n_e are given by equations (70) and (71) [15]:

$$n_o^2 = 2.7359 + \frac{0.01878}{\lambda^2 - 0.01822} - 0.01354\lambda^2, \tag{70}$$

$$n_e^2 = 2.3753 + \frac{0.01224}{\lambda^2 - 0.01667} - 0.01516\lambda^2, \tag{71}$$

where λ is the wavelength in µm. The equations are valid from 0.22 - 1.06 µm. The refractive indexes are plotted in figure 47.

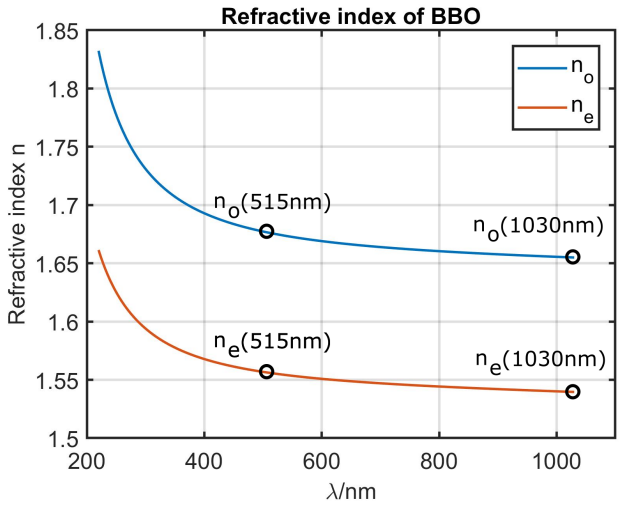

Figure 47: Refractive index of BBO at 220 - 1060 nm.

Figure 47 shows something very important: The beam at 1030 nm must be ordinary and the second harmonic beam at 515 nm must be extraordinary. As can be seen in the figure, n_o(1030 nm) is in between n_e(515 nm) and n_o(515 nm). The refractive index of the beam at 515 nm can then be tuned to equal n_o(1030 nm), thus fulfilling the phase matching condition. On the other hand, n_o(515 nm) is greater than both n_e(1030 nm) and n_o(1030 nm). It is therefore impossible to tune the refractive index of the 1030-nm beam to be equal to that of the 515-nm beam, if the 1030-nm beam is extraordinary.

The phase matching angle θ can be calculated using equation (69). The solution to this equation for a range of wavelengths is called the phase-matching curve and is shown in figure 48. The phase matching curve shows that the phase matching angle for SHG at 1030 nm is $\theta = 23.39°$. In practice, the BBO is cut at the phase matching angle for the desired nonlinear effect. This will let the input beam be at normal incidence.

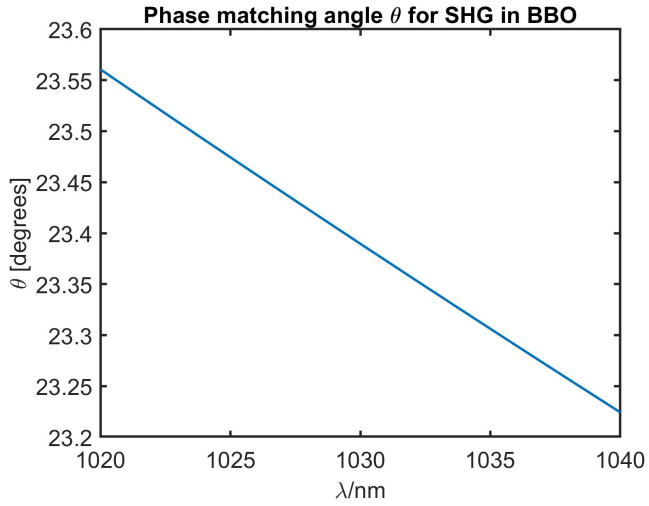

Figure 48: Phase matching curve for SHG in BBO.

As figure 48 shows, the phase matching angle θ depends on the wavelength. This means that it is not possible to achieve perfect phase matching over the entire bandwidth of the laser. This will lead to reduced efficiency of the SHG process further from the wavelength at which phase matching is achieved, and therefore a reduced intensity of the second harmonic.

It can be shown [15] that the intensity I of the second harmonic is given by

$$I \propto L^2 \text{sinc}^2(\frac{\Delta k L}{2\pi}), \tag{72}$$

where $\text{sinc}(x) = \frac{\sin(\pi x)}{\pi x}$, L is the length of the crystal and $\Delta k = k_3 - 2k_1$ is the phase mismatch. Equation (72) shows that a longer crystal will provide higher conversion but a narrower bandwidth. For SHG the phase mismatch can be calculated as $\Delta k = \frac{4\pi}{\lambda_1}(n(\lambda_3) - n(\lambda_1))$ [15]. This shows that the phase mismatch depends on the wavelength λ_1 of the fundamental.

Equation (72) will be used to find a suitable thickness of the crystal. The crystal should be as thick as possible to provide the highest conversion, but thin enough to accommodate the desired bandwidth. Assuming a Gaussian pulse, equation (4) gives a bandwidth of 1.1 THz for a 400 fs pulse. The bandwidth in frequency can be converted to wavelength by equation (6), which results in a bandwidth of 3.9 nm. This means that the second-harmonic will have a bandwidth of 1.95 nm (assuming a Gaussian profile). To determine Δk, equations (69) - (71) are first used to find the refractive indexes over the desired wavelength range. This gives Δk as a function of wavelength. The obtained Δk is then inserted in equation (72), to obtain the efficiency of the SHG process as a function of wavelength. Equation (72) is normalized and plotted in figure 49 for a 4 mm thick crystal. This graph shows the efficiency of the SHG process as a function of the wavelength. The efficiency is at least 0.5 over the desired bandwidth, which shows that 4 mm is a suitable thickness.

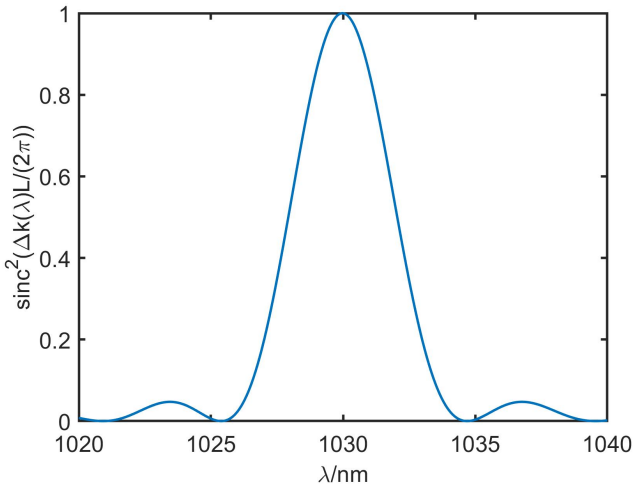

Figure 49: Efficiency of SHG for a 4-mm-thick BBO-crystal.

Appendix 2

MATLAB code

Script for producing the autocorrelation traces of figure 10:

```
%Autocorrelation of chirped Gaussian pulse with chirp parameter a
    and time constant tau0.

c = 299792458; %speed of light
lambda = 1030e-9; %INPUT wavelength
omega0 = 2*pi*c/lambda; %angular frequency
tauFWHM = 20e-15; %INPUT FWHM width of pulse
tau0 = tauFWHM/1.18; %time constant (Gaussian pulse)
tau = linspace(-50e-15,50e-15,5000); %time delay

%Calculate trace for three different chirp parameters a
a = 0; %INPUT first chirp parameter
%calculate autocorrelation trace
R1 = 1+2*exp(-tau.^2./tau0^2)+4*exp(-(3+a^2).*tau.^2/(4*tau0^2)).*
    cos(a.*tau.^2/(2*tau0^2)).*cos(omega0.*tau)+exp(-(1+a^2).*tau
    .^2/tau0^2).*cos(2*omega0*tau);
subplot(1,3,1)
plot(tau,R1)
title('a=0')
xlabel('t/s')

a = 2; %INPUT second chirp parameter
%calculate autocorrelation trace
R2 = 1+2*exp(-tau.^2./tau0^2)+4*exp(-(3+a^2).*tau.^2/(4*tau0^2)).*
    cos(a.*tau.^2/(2*tau0^2)).*cos(omega0.*tau)+exp(-(1+a^2).*tau
    .^2/tau0^2).*cos(2*omega0*tau);
subplot(1,3,2)
plot(tau,R2)
title('a=2')
xlabel('t/s')

a = 4; %INPUT third chirp parameter
%calculate autocorrelation trace
R3 = 1+2*exp(-tau.^2./tau0^2)+4*exp(-(3+a^2).*tau.^2/(4*tau0^2)).*
    cos(a.*tau.^2/(2*tau0^2)).*cos(omega0.*tau)+exp(-(1+a^2).*tau
    .^2/tau0^2).*cos(2*omega0*tau);
subplot(1,3,3)
plot(tau,R3)
title('a=4')
xlabel('t/s')
```

Script for simulating NOPA. Produces plots of phase-matching curves, $|\Delta k|$, coherence length, pulse-splitting length, gain curves and efficiency. Requires the functions nOrd(lambda), nExt(lambda), vgOrd(lambda) and vgExt(lambda), which follows after the main script.

```
%NOPA in BBO, type 1, signal and idler ordinary, pump extraordinary
%All distances are in meters, all times in seconds
%Some parts of the script requires the user to evaluate the result
    of a calculation and then to manually input the optimal value
    afterwards (these parts are indicated in the script with the
    word MANUALLY). The script therefore must be run several times.

%clear all
c = 299792458; %speed of light in vacuum

```

```
%1. lambda1 = signal, lambda2 = idler, lambda3 = pump
lambda3 = 515e-9; %INPUT pump
lambda1 = linspace(600e-9,800e-9,500); %INPUT siganl range
lambda2 = 1./(1./lambda3-1./lambda1); %idler (set by signal and
    pump)

%2. Phase match.
alpha = [0 1 2 3]/360*(2*pi); %INPUT non-coll. angles here
k1 = 2.*pi.*nOrd(lambda1)./lambda1; %All k are magnitudes of
    wavevectors
k2 = 2.*pi.*nOrd(lambda2)./lambda2;
k30 = 2*pi/lambda3; %k3 in vacuum
figure(1)
hold on
box on
for i = 1:length(alpha)
    %Find the desired k3 for phase-match
    k3 = sqrt(k2.^2-(k1.*sin(alpha(i))).^2)+k1.*cos(alpha(i));
    n3 = k3/k30; %Use this to find desired refractive index
    %Use equation for refractive index in birefringent material to
        find the desired theta using n3
    theta = zeros(1,length(n3));
    for j = 1:length(n3)
        thetaFun = @(theta) cos(theta).^2./nOrd(lambda3).^2 + sin(
            theta).^2./nExt(lambda3).^2 - 1./n3(j).^2;
        theta(j) = fzero(thetaFun,20/360*2*pi); %Find theta,
            initial guess 20 degrees
    end
    plot(lambda1*1e9,theta/(2*pi)*360)
end
legend('\alpha = 0^\circ','\alpha = 1^\circ','\alpha = 2^\circ','\
    alpha = 3^\circ')
xlabel('\lambda/nm')
ylabel('\theta [degrees]')
title('Phase matching angle \theta for different values of \alpha')

%3. Find how alpha and theta affects sum(abs(Deltak)). Minimizing
    this sum will give the alpha and theta that minimizes the
    integrated wavevector mismatch over the desired wavelength range
    . This alpha and theta should then give a good starting point at
     which to calculate the gaincurves.
birRef = @(theta,lambda) sqrt(1./(cos(theta).^2./nOrd(lambda).^2 +
    sin(theta).^2./nExt(lambda).^2));
alpha = [0 0.5 1 1.5 2 2.3 2.5 3]/360*2*pi; %INPUT non-coll. angels
theta = linspace(20,26,200)/360*2*pi; %INPUT Range of phase-
    matching angles
DeltakSum = zeros(length(alpha),length(theta));
%sum Deltak for each combination of theta and alpha for all
%wavelength points
for j = 1:length(alpha)
    for i = 1:length(theta)
        %Calculate Deltak as difference between length of k2 and
            the distance between the tips of k1 and k3
        k3 = 2.*pi.*birRef(theta(i),lambda3)./lambda3;
        k3k1diff = sqrt((k3-k1.*cos(alpha(j))).^2+(k1.*sin(alpha(j)
            )).^2);
        Deltak = k3k1diff - k2;
        %Sum for all lambda to get total Deltak
```

```
        DeltakSum(j,i) = sum(abs(Deltak));
    end
end
figure(2)
plot(theta/2/pi*360,DeltakSum)
legend('\alpha = 0^\circ','\alpha = 0.5^\circ','\alpha = 1^\circ','\alpha = 1.5^\circ','\alpha = 2^\circ','\alpha = 2.3^\circ','\alpha = 2.5^\circ','\alpha = 3^\circ')
title('\Sigma\mid\Deltak\mid as function of \theta for different \alpha')
xlabel('\theta [degrees]')
ylabel('\Sigma\mid\Deltak\mid')
%MANUALLY insert here the combination of alpha and theta that gave the smallest sum(Deltak). Calculate Deltak for these values.
alpha = 2.05/360*2*pi;
theta = 23.6/360*2*pi;
k3 = 2.*pi.*birRef(theta,lambda3)./lambda3;
k3k1diff = sqrt((k3-k1.*cos(alpha)).^2+(k1.*sin(alpha)).^2);
Deltak = k3k1diff - k2;

%4. Determine lengths
%4 a) Coherence length Lc = 2pi/abs(Deltak). Depends on Deltak, so may need
%to be adjusted after calculating the gain curves. However, these curves will determine the thickness of the crystal, so they must be plotted before calculating the gain.
Lc = 2.*pi./abs(Deltak);
figure(3)
semilogy(lambda1*1e9,Lc)
title('Coherence length L_c')
xlabel('\lambda/nm')
ylabel('L_c/m')
%4 b) Pulse splitting length. Assume pulse length tau = 400 fs
tau = 400e-15; %INPUT pulse length here
%Calculate the group velocities
vg1 = vgOrd(lambda1);
vg2 = vgOrd(lambda2);
dndlambda = (birRef(theta,lambda3+0.1e-9)-birRef(theta,lambda3-0.1e-9))/0.2e-9;
vg3 = c/(birRef(theta,lambda3)-lambda3*dndlambda);
l13 = abs(tau./(1./vg1-1/vg3)); %Split between signal and pump
l23 = abs(tau./(1./vg2-1/vg3)); %Split between idler and pump
figure(4)
plot(lambda1*1e9,l13)
hold on
plot(lambda2*1e9,l23)
title('Pulse splitting length L_{split}')
xlabel('\lambda/nm')
ylabel('L_{split}/m')
legend('l_{sig-pump}','l_{idler-pump}')

%5. Plot gain curves.
epsilon0 = 8.8542e-12; %Permittivity of free space
%Nonlinear coeff. for BBO
d22 = 2.2e-12;
d31 = 0.08e-12;
deff = d31*sin(theta) + d22*cos(theta);
%Angular frequencies of signal and idler
```

```
omega1 = 2.*pi.*c./lambda1;
omega2 = 2.*pi.*c./lambda2;
%---These are the parameters to change when optimizing the gain --
I3 = 50e13; % INPUT Pump intensity 7e13 [W/m^2]
L = 1e-3; %MANUALLY input crystal length [m] based on previous
    result
theta = 23.6/360*2*pi; %INPUT phase-matching angle
alpha = [2 2.025 2.05 2.075]/360*2*pi; %INPUT non-coll. angles
%-----------------------------------------------------------------
figure(5)
for i = 1:length(alpha)
    %Find Deltak, calculate g^2 (g2) and Gamma^2 (Gamma2), use this
        to find gain G
    k3 = 2.*pi.*birRef(theta,lambda3)./lambda3;
    k3k1diff = sqrt((k3-k1.*cos(alpha(i))).^2+(k1.*sin(alpha(i)))
        .^2);
    Deltak = k3k1diff - k2;
    Gamma2 = 2.*deff.^2.*omega1.*omega2.*I3./(c.^3.*epsilon0.*nOrd(
        lambda1).*nOrd(lambda2).*birRef(theta,lambda3));
    g2 = Gamma2 - Deltak.^2/4;
    G = 1+Gamma2./g2.*sinh(sqrt(g2).*L).^2;
    semilogy(lambda1*1e9,G)
    hold on
end
xlim([600 800])
title('Gain G at \theta = 23^\circ, I_3 = 50 GW/cm^2')
legend('\alpha = 2^\circ','\alpha = 2.025^\circ','\alpha = 2.05^\
    circ','\alpha = 2.075^\circ')
xlabel('\lambda/nm')
ylabel('G [I_{out}/I_{in}]')

% Plot sinc^2(Deltak(lambda)*L) at theta and alpha that minimizes
    sum(abs(Deltak))
%MANUALLY insert the optimum alpha and theta as found from the gain
    curves
alpha = 2.05/360*2*pi; %MANUALLY insert optimal alpha
theta = 23.6/360*2*pi; %MANUALLY insert optimal theta
k3 = 2.*pi.*birRef(theta,lambda3)./lambda3;
k3k1diff = sqrt((k3-k1.*cos(alpha)).^2+(k1.*sin(alpha)).^2);
Deltak = k3k1diff - k2;
figure(6)
plot(lambda1*1e9,sinc(Deltak*1e-3/(2*pi)).^2)
title('sinc^2(\Deltak(\lambda)L/(2\pi)) at \theta = 23.6^\circ, \
    alpha = 2.05^\circ and L = 1 mm')
xlabel('\lambda/nm')
ylabel('sinc^2(\Deltak(\lambda)L/(2\pi))')


%6. Calculate walk-off angle rho of k3 due to birefringence.
theta = linspace(22,24)/360*2*pi; %INPUT desired range of phase-
    match angles
rho = atan((nOrd(lambda3)/nExt(lambda3))^2.*tan(theta))-theta;
figure(7)
plot(theta/2/pi*360,rho/2/pi*360)
title('Walkoff angle \rho between signal and pump')
xlabel('\theta [degrees]')
ylabel('\rho [degrees]')
```

nOrd(lambda):

```
%no in BBO using Sellmeier equation. Lambda is inputted in m.

function no = nOrd(lambda)
lambda = lambda.*1e6; %convert to um
no = 2.7359+0.01878./(lambda.^2-0.01822)-0.01471.*lambda
    .^2+0.0006081.*lambda.^4-0.00006740.*lambda.^6;
no = sqrt(no);
```

nExt(lambda):

```
%ne in BBO using Sellmeier equation. Lambda is inputted in m.

function ne = nExt(lambda)
lambda = lambda.*1e6; %convert to um
ne = 2.3753+0.01224./(lambda.^2-0.01667)-0.01627.*lambda
    .^2+0.0005716.*lambda.^4-0.00006305.*lambda.^6;
ne = sqrt(ne);
```

vgOrd(lambda):

```
%Determine group velocity of ordinary wave in BBO. Take derivative
    of Sellmeier equation and than use the equation for the group
    velocity.
%Lambda is inputted in m

function vgo = vgOrd(lambda)
c = 299792458; %Speed of light in vacuum
%Constants for Sellmeier equation
A = 2.7359;
B = 0.01878;
C = 0.01822;
D = 0.01354;
lambda = lambda.*1e6; %convert lambda to um
DnDlambda = 0.5.*(-2.*B.*lambda.*(lambda.^2-C).^(-2)-2.*D.*lambda)
    .*(A+B.*(lambda.^2-C).^(-1)-D.*lambda.^2).^(-0.5);
vgo = c./(nOrd(lambda./1e6)-(lambda./1e6).*DnDlambda);
```

vgExt(lambda):

```
%Determine group velocity of extraordinary wave in BBO. Take
    derivative of Sellmeier equation and than use the equation for
    the group velocity.
%Lambda is inputted in m

function vge = vgExt(lambda)
c = 299792458;%Speed of light in vacuum
%Constants for Sellmeier equation
A = 2.3753;
B = 0.01224;
C = 0.01667;
D = 0.01516;
lambda = lambda.*1e6;
DnDlambda = 0.5.*(-2.*B.*lambda.*(lambda.^2-C).^(-2)-2.*D.*lambda)
    .*(A+B.*(lambda.^2-C).^(-1)-D.*lambda.^2).^(-0.5);
vge = c./(nExt(lambda./1e6)-(lambda./1e6).*DnDlambda);
```

Script for calculating DFG. Produces plots of the phase-matching curves and the coherence length. Also makes use of nOrd(lambda) and nExt(lambda).

```
%DFG in BBO
%All distances are in meters, all times in seconds
%The calculation of the coherence length requires the user to
    manually input the optimal phase-matching angle from the
```

```
    previous step (indicated by the word MANUALLY in the script).
    The script must therefore be run twice.

%clear all
c = 299792458; %Speed of light in vacuum

%1. DFG between lambda1 and lambda3 gives lambda2
lambda3 = linspace(620e-9,750e-9,500); % INPUT first wave
lambda1 = 1030e-9; %INPUT second wave
lambda2 = 1./(1./lambda3-1./lambda1); %calculate DFG

%2. Phase match. k1 and k2 are ordinary waves, while k3 is
    extraordinary
alpha = [0 0.5 1 1.5]/360*(2*pi); %INPUT non-coll. angle
k2 = 2.*pi.*nOrd(lambda2)./lambda2; %All k are magnitudes of
    vectors
k30 = 2.*pi./lambda3; %k3 in vacuum
k1 = 2*pi.*nOrd(lambda1)/lambda1;
figure(1)
hold on
box on
for i = 1:length(alpha)
    %Find the desired k3 for phase-match
    k3 = sqrt(k2.^2-(k1.*sin(alpha(i))).^2)+k1.*cos(alpha(i));
    n3 = k3./k30; %Use this to find desired refractive index
    %Use equation for refractive index in birefringent material to
       find the desired theta using n3
    theta = zeros(1,length(n3));
    for j = 1:length(n3)
        thetaFun = @(theta) cos(theta).^2./nOrd(lambda3(j)).^2 +
           sin(theta).^2./nExt(lambda3(j)).^2 - 1./n3(j).^2;
        theta(j) = fzero(thetaFun,80/360*2*pi); %Find root to eq
           for n3, gives theta
    end
    plot(lambda3*1e9,theta/(2*pi)*360)
end
legend('\alpha = 0^\circ','\alpha = 0.5^\circ','\alpha = 1^\circ','
    \alpha = 1.5^\circ')
xlabel('\lambda/nm')
ylabel('\theta [degrees]')
title('Phase matching angle \theta for different values of \alpha')

%3. Coherence length
%Birefringent refractive index
birRef = @(theta,lambda) sqrt(1./(cos(theta).^2./nOrd(lambda).^2 +
    sin(theta).^2./nExt(lambda).^2));
theta = 20.2/360*2*pi; %MANUALLY input optimal phase-matching angle
%Find Deltak
k3 = 2.*pi.*birRef(theta,lambda3)./lambda3;
k3k1diff = k3 - k1;
Deltak = k3k1diff - k2;
%Use Deltak to find coherence length
Lc = 2.*pi./abs(Deltak);
figure(2)
semilogy(lambda3*1e9,Lc)
title('Coherence length L_c for DFG')
xlabel('\lambda/nm')
ylabel('L_c/m')
```

Script for calculating SHG. Produces plots of refractive index, phase matching curve and efficiency. Also makes use of nOrd(lambda) and nExt(lambda).

```
%SHG for 1030 nm light in BBO. Fundamental has ordinary polarization, second harmonic has extraordinary polarization
c = 299792458; %speed of light in vacuum

%1. Plot refractive index no and ne
lambda = linspace(400e-9,1200e-9,500); %INPUT wavelength
no = nOrd(lambda); %ordinary refractive index
ne = nExt(lambda); %extraordinary refractive index
figure(1)
plot(lambda*1e9,no)
hold on
plot(lambda*1e9,ne)
legend('n_o','n_e')
title('Refractive index of BBO')
xlabel('\lambda/nm')
ylabel('Refractive index n')
grid on

%2. Phase-matching curves
lambda1 = linspace(1020e-9,1040e-9,500); %INPUT fundamental wave
lambda3 = lambda1./2; %second harmonic
n1 = nOrd(lambda1); %refractive index of fundamental wave
%Solve for the phase-matching angle theta that makes n3 = n1 for each lambda
theta = zeros(1,length(n1));
for j = 1:length(n1)
    %Find theta so that n(lambda3) = n(lambda1)
    thetaFun = @(theta) cos(theta).^2./nOrd(lambda3(j)).^2 + sin(theta).^2./nExt(lambda3(j)).^2 - 1./n1(j).^2;
    %Find root to eq for n3, this gives theta. Initial guess 23 degrees
    theta(j) = fzero(thetaFun,23/360*2*pi);
end
figure(2)
plot(lambda1*1e9,theta/(2*pi)*360)
xlabel('\lambda/nm')
ylabel('\theta [degrees]')
title('Phase matching angle \theta for SHG in BBO')

%3. Plot sinc(Deltak*L), gives efficiency
L = 4e-3; %INPUT crystal thickness
%define refractive index of extraordinary wave
birRef = @(theta,lambda) sqrt(1./(cos(theta).^2./nOrd(lambda).^2 + sin(theta).^2./nExt(lambda).^2));
n3 = birRef(23.39/360*2*pi,lambda3); %refractive index of second-harmonic
Deltak = 4*pi./lambda1.*(n3-nOrd(lambda1));
eff = sinc(Deltak*L/(2*pi)).^2;
figure(3)
plot(lambda1*1e9,eff);
xlabel('\lambda/nm')
ylabel('sinc^2(\Deltak(\lambda)L/(2\pi))')
```

The following script produces the plots in figures 3, 2, 5, 6, 7, 14 and 16. Note that the plots are only intended to illustrate the concepts, they are not based on any calculations related to the setup that has been described in this thesis.

```
%SPM
x = linspace(-3,3,500);
figure(1)
hold on
box on
yyaxis left
plot(x,(0.5*exp(-x.^2)).^2,'-'); %Pulse envelope intensity in time
ylabel('Intensity (arb.u.)')
axis([-2,2,-0.2,0.4])
yyaxis right
plot(x,0.25*x.*exp(-x.^2).*exp(-x.^2)); %Derivative of the
    intensity envelope
axis([-2,2,-0.2,0.4])
xlabel('Time (arb.u.)')
ylabel('Frequency shift (arb.u.)')

%self steepening
figure(2)
hold on
box on
plot(x,0.5*exp(-log((3-x)./1).^2),'b');
axis([-3,3,0,0.6])
xlabel('Time (arb.u.)')
ylabel('Amplitude (arb.u.)')

%CEP
figure(3)
hold on
box on
plot(x,0.5*exp(-x.^2).*sin(5*x+pi/8),'b'); %Pulse in time
plot(x,0.5*exp(-x.^2),'r--'); %Pulse envelope in time
axis([-3,3,-0.7,0.8])
xlabel('Time arb.u.')
ylabel('Amplitude arb.u.')

%phase vs. group velocity
x1 = linspace(-4,2);
figure(4)
subplot(1,3,1)
hold on
box on
plot(x1,0.5*exp(-(x1+1).^2).*cos(5*(x1+1)),'b'); %Pulse in time
plot(x1,0.5*exp(-(x1+1).^2),'r--'); %Pulse envelope in time
xlabel('z (arb.u.)')
ylabel('Amplitude (arb.u.)')

x1 = linspace(-3,3);
subplot(1,3,2)
hold on
box on
plot(x1,0.5*exp(-x1.^2).*cos(5*x1-pi/4),'b'); %Pulse in time
plot(x1,0.5*exp(-x1.^2),'r--'); %Pulse envelope in time
xlabel('z (arb.u.)')

x1 = linspace(-2,4);
subplot(1,3,3)
hold on
box on
```

```
58 plot(x1,0.5*exp(-(x1-1).^2).*cos(5*(x1-1)-pi/2),'b'); %Pulse in
       time
59 plot(x1,0.5*exp(-(x1-1).^2),'r--'); %Pulse envelope in time
60 xlabel('z (arb.u.)')
61
62 %chirp by dispersion
63 figure(5)
64 subplot(1,2,1)
65 hold on
66 box on
67 plot(x,0.5*exp(-x.^2).*cos(5*x),'b'); %Pulse in time
68 plot(x,0.5*exp(-x.^2),'r--'); %Pulse envelope in time
69 xlabel('Time (arb.u.)')
70 ylabel('Amplitude (arb.u.)')
71
72 subplot(1,2,2)
73 hold on
74 box on
75 plot(x,0.5*exp(-(0.8*x).^2).*cos(5*x+2*x.^2),'b'); %Pulse in time
76 plot(x,0.5*exp(-(0.8*x).^2),'r--'); %Pulse envelope in time
77 xlabel('Time (arb.u.)')
78
79 %CEP for short vs. long pulse
80 figure(7)
81 subplot(2,2,1)
82 plot(x,0.5*exp(-x.^2).*cos(4*x),'b');
83 box on
84 title('a) \phi = 0')
85 xlabel('Time (arb.u.)')
86 ylabel('Amplitude (arb.u.)')
87
88 subplot(2,2,2)
89 plot(x,0.5*exp(-x.^2).*cos(4*x-pi/2),'b');
90 box on
91 title('b) \phi = \pi/2')
92 xlabel('Time (arb.u.)')
93 ylabel('Amplitude (arb.u.)')
94
95 subplot(2,2,3)
96 plot(x,0.5*exp(-x.^2).*cos(20*x),'b');
97 box on
98 title('c) \phi = 0')
99 xlabel('Time (arb.u.)')
100 ylabel('Amplitude (arb.u.)')
101
102 subplot(2,2,4)
103 plot(x,0.5*exp(-x.^2).*cos(20*x-pi/2),'b');
104 box on
105 title('d) \phi = \pi/2')
106 xlabel('Time (arb.u.)')
107 ylabel('Amplitude (arb.u.)')
108
109 %Up vs. downchirp
110 figure(8)
111 subplot(1,2,1)
112 box on
113 plot(x,0.5*exp(-x.^2).*sin(8*x+2*x.^2),'b'); %Pulse in time
114 xlabel('Time (arb.u.)')
```

```
115 ylabel('Amplitude (arb.u.)')
116 title('a)')
117 subplot(1,2,2)
118 box on
119 plot(x,0.5*exp(-x.^2).*sin(8*x-2*x.^2),'b'); %Pulse in time
120 xlabel('Time (arb.u.)')
121 title('b)')
```